UNIVERSITY OF OKLAHOMA

GRADUATE COLLEGE

MID-WAVELENGTH AND LONG-WAVELENGTH INTERBAND CASCADE INFRARED PHOTODETECTORS

A DISSERTATION

SUBMITTED TO THE GRADUATE FACULTY

in partial fulfillment of the requirements for the

Degree of

DOCTOR OF PHILOSOPHY

By

LIN LEI
Norman, Oklahoma
2017

MID-WAVELENGTH AND LONG-WAVELENGTH INTERBAND CASCADE INFRARED PHOTODETECTORS

A DISSERTATION APPROVED FOR THE
DEPARTMENT OF ENGINEERING PHYISCS

BY

Dr. Rui Q. Yang, Chair

Dr. Michael B. Santos. Co-chair

Dr. Kieran J. Mullen

Dr. Matthew B. Johnson

Dr. Chung Kao

Dr. Hjalti Sigmarsson

Acknowledgments

I would like to start by acknowledging my advisor, Prof. Rui Q. Yang, for offering me the opportunity to conduct my research in his quantum device lab. He has been completely selfless in sharing his wisdom and has always encouraged me to think independently. I would like to thank him for his patient efforts in training me, not only in research skills, but more importantly in the mindset of thinking. I have benefited immensely from his passion for research and his sincere personality.

Next, I would like to thank my co-advisor, Prof. Michael B. Santos for his guidance and support during my graduate studies and research in the physics department. It was my great pleasure to work with him in the MBE group. I would also like to express my gratitude to Prof. Matthew B. Johnson for his generous advices on my research. In addition, I am also thankful to Prof. Kieran J. Mullen, Chung Kao and Hjalti Sigmarsson for serving on my committee.

It was my honor to work in such a great group with many talented students where everyone helped each other as a great team. I worked closely with Dr. Hossein Lotfi before he graduated and learned invaluable lessons from him. He taught me the characterization and analysis techniques of the interband cascade devices. He is a good friend and was always kind in sharing his knowledge and offering assistance. I am also grateful to Dr. Lu Li for his hard work on MBE growth and device fabrication. He is a nice and reliable person who helped me in both my research and personal life. I would like to thank Dr. Hao Ye for her excellent MBE growth. Many thanks to my friend Dr. Yuchao Jiang who generously provided suggestions to my research and favors to my daily life. I would also like to thank SM Shazzad Rassel for his technical support to my research. I am thankful to Dr. Robert T. Hinkey for the discussions with him that helped me understand interband cascade devices when I first joined this group. I have worked closely with Wenxiang Huang since he joined our group, he is fast learner and contributed greatly to my dissertation. I would like to thank Jeremy A. Massengale for his MBE support of the recent samples. I would also like to thank the previous and current members of the MBE group: Dr. Tetsuya D. Mishima, Joel C. Keay, Chomani Gaspe, Mukul Debnath, Sangeetha Vijeyaragunathan, Kaushini Wickramasinghe for their help on XRD analysis and Hall measurements.

My appreciation also goes to the Homer L. Dodge Department of Physics and Astronomy for accepting me into their graduate program and providing me with the academic knowledge and techniques needed to be successful in my graduate career. I am grateful to the Physic department and the Graduate College for the financial support during my time at OU. I also want to thank all my friends, especially thanks to Yunxiang Wang and Dexin Shi, for the generous help that they offered in various aspects of my life in Norman.

The research presented in this dissertation was supported by funding from NSF (Awards No. ECCS-1202318 and No. DMR-1229678), and AFOSR (Award No. FA9550-15-1- 0067).

Last but not least, I would like to express the deepest appreciation to my parents and my sister for their unconditional love, and to my wife Die Zhou for her constant encouragement and support.

Table of Contents

List of Tables

List of Figures

Abstract

Interband cascade (IC) devices are a family of infrared optoelectronic devices that includes interband cascade lasers (ICLs), interband cascade infrared photodetectors (ICIPs) and interband cascade infrared thermophotovoltaics (ICTPVs). They are unique due to their multiple-stage architecture based on type-II heterostructures. In IC devices, the carrier transport is rectified with two unipolar barriers (injectors), namely the electron barrier (hole injector) and hole barrier (electron injector). The series connection between cascade stages is realized by employing the type-II broken-gap alignment between InAs and GaSb layers. While a conventional single stage detector is limited by the short diffusion length and carrier lifetime at high temperatures and long wavelengths, an ICIP with a series of thin discrete absorbers can circumvent these limitations with high device performance. Although the responsivity of ICIPs is reduced by the thin absorbers, noise is also reduced significantly by the series connected cascade stages so that a large signal to noise ratio is retained. Most of the interest for IR detector applications is focused on the mid-wavelength (MW) infrared (IR) and long-wavelength (LW) IR bands. However, most of them require a cooling system to achieve high device performance. ICIPs are one of the most promising candidates for meeting the high-performance and uncooled requirements of these applications.

MW ICIPs based on InAs/GaSb type-II superlattice (T2SL) and bulk GaInAsSb absorbers are discussed in detail. High temperature operation and high device performance are demonstrated with Johnson-noise limited detectivities over 1.0×10^{9} cm·Hz$^{1/2}$/W at 300 K.

LW ICIPs with current-matching and non-current matching architectures were systematically studied. These ICIPs are capable of operating at high temperatures up to 340 K. They exhibited a high device performance with a detectivity (D^*) higher than 1.0×10^9 and 1.0×10^8 cm$\cdot$Hz$^{1/2}$/W at 200 and 300 K, respectively. While current-matching is necessary for maximizing photon absorption to achieve optimal responsivity, the lower responsivity in the non-current matched ICIPs is attributed to light attenuation in the optically deeper stages. Meanwhile, the responsivity in the non-current matched ICIPs is enhanced by the significantly higher electrical gain, along with the much higher resistances, so that their device performance is comparable or even slightly higher than the current matched ICIPs.

Multi-stage ICIPs show superior performance over conventional one-stage detectors at high temperatures in both the MWIR and LWIR regions. The presence of high electrical gain in the both MW and LW ICIPs may be related to two mechanisms: one is the photoconductive gain due to a shorter transit time than carrier lifetime, the other is the compensation of dark current to maintain current continuity.

The observed multiple negative differential conductance (NDC) features in the LW ICIPs at high temperatures are related to the sequential turn-off of intraband tunneling of minority carriers through the electron barriers. Five sets of ICIPs with various structural details and carrier concentrations in the absorber were systematically studied to illustrate the underlying physics and demonstrate the mechanism for NDC.

Chapter 1 Introduction

1.1 Background and motivation

Infrared (IR) detectors are sensors of IR radiation that convert optical signal into electrical current. They are widely used in many applications, such as gas sensing, thermal imaging, night vision, infrared tracking and free space communication. Conventional IR detectors are typically a one-stage structure, *i.e.* a single absorber (made of narrow bandgap semiconductors) which generally needs to be thick to ensure enough light absorption to generate a decent output signal. There are two fundamental limitations for these IR detectors: they cannot operate with reasonable high performance at elevated temperatures due to the exponentially increased thermal noise, and they have a relatively slow response time because the electrons have to travel a long distance in the thick absorber. Therefore, they are typically operated at low temperatures with a cryogenic cooling system to reduce the noise and maintain high device performance, resulting in increased system cost, size, weight and power consumption. On the other hand, many IR applications require a fast response speed, particularly for the real-time thermal imaging and free space communication.

With the increased demanding for uncooled and compact IR detectors with high response speed, especially for the development of autopilot in automotive industry nowadays, the interband cascade IR photodetectors (ICIPs) have been established with a novel structure design to satisfy these requirements. Essentially, the thick absorber in the one-stage detector is divided into multiple series-connected discrete absorbers in an ICIP structure. Thus, compared to the conventional IR detectors, the transport distance for the electrons is much shorter in the ICIPs, leading to a shorter transit time, and hence a faster response. In the meantime, the noises are significantly reduced, even at much higher temperatures, with the series-connected stages.

The low operating temperature of IR detectors has been one of the primary concerns in sensitive IR systems. While uncooled thermal detectors have been successfully demonstrated in rudimental thermal imagers, their device performance is limited by their slow response speeds and low sensitivities. Photodetectors make it possible to achieve both high sensitivity and fast response. However, most of the photodetectors are typically operated at cryogenic temperatures (78 to 200 K) to reduce the noise originating from several sources in narrow bandgap semiconductor materials [1]. Recently, high-operating-temperature (HOT) photodetectors have drawn much research interest to develop high-resolution IR imaging systems that eliminate the requirement of cryogenic cooling.

The $Hg_{1-x}Cd_xTe$ photodetectors have long been the leading technology with the best device performance [2]. They can operate at room temperature in both mid-wavelength (MW) IR (3-5 µm) and long wavelength (LW) IR (8-14 µm) ranges, but the device performance is not optimal with a low dynamic resistance, particularly in the LWIR region with a detectivity (sensitivity) about 8×10^{7} $\mathrm{cm\cdot Hz^{1/2}/W}$ at 8 µm. Additionally, the expensive substrates and low device yield of $Hg_{1-x}Cd_xTe$ photodetectors lead to a relatively high cost. Photodetectors based on InAs/GaSb type-II superlattice (T2SL) have been theoretically projected to outperform of $Hg_{1-x}Cd_xTe$ photodetectors [3-5] due to a low tunneling current (with a relatively larger effective mass) [6] and suppressed Auger recombination [7,8]. However, the performance of real device implementation with T2SL has not been fully demonstrated. This is mainly attribute to the relatively small absorption coefficient of T2SL material. Besides, the III-V narrow bandgap materials suffer from low material quality and short carrier lifetime where the Shockley-Read-Hall (SRH) recombination limits the device performance.

The barrier detectors based on T2SL have been introduced with unipolar barriers to impede the flow of majority carrier dark current. The nBn detectors have demonstrated a reduced dark current associated with SRH process (confined within the unipolar barriers with much wider bandgaps) and noise without impeding photocurrent flow [9,10], the suppression of surface leakage current was also observed in nBn detectors with unipolar barriers [11-13]. The barrier detectors have achieved a device performance approaching that of the state-of-the-art $Hg_{1-x}Cd_xTe$ photodetector in the LWIR region. However, they are still limited with low operating temperature, because the diffusion length of minority carriers is reduced at elevated temperatures. Since the absorption coefficient of T2SL material is small, in order to obtain a high quantum efficiency, detectors require a thick absorber to have enough photon absorption at low temperatures. With raising the temperature, the diffusion length is reduced and the carrier lifetime decreased, so part of the photo-generated carriers cannot be collected when the diffusion length is shorter than the absorber thickness at a certain high temperature. This reduces the quantum efficiency and lowers the device performance. Meanwhile, for high speed application, the absorber thickness must be reduced to shorten the carrier transport time to ensure a fast response.

To circumvent the diffusion length limitation for HOT photodetectors, the interband cascade IR photodetectors (ICIPs) [14,15]have been introduced by using a multiple cascade stage architecture with discrete absorbers, where each of them is shorter than the diffusion length. Each cascade stage in an ICIP is similar to the complementary barrier IR photodetector (CBIRD) [16] where the absorber is sandwiched between quantum engineered electron and hole barriers, while the series connection between cascade stages is realized with the type-II broken gap alignment between InAs and GaSb quantum structures (at the interface of the electron and hole barriers). As such, the photo-generated carriers travel only over one stage before they recombine in the next stage, and the individual absorber thickness can be significantly shorter than the diffusion length, while the total absorber thickness can be much longer than the diffusion length. In such case, the incident photons can be largely absorbed with a large total absorber thickness, meanwhile, the photo-generated carriers can be effectively collected at considerably higher temperatures with a much shorter transit time. Therefore, ICIPs with thin discrete absorber design are feasible for high-temperature and high-speed application without compromising the absorption efficiency.

Then quantum efficiency or responsivity of an ICIP is generally low due to the thin discrete absorbers. However, in the meantime, both shot noise and thermal noise are substantially reduced because of the series connected cascade stages, and they are roughly inversely proportional to the number of stages [14]. Hence, the signal to noise ratio (or detectivity) maintains at a larger value at elevated temperatures compared to conventional single stage detectors. In addition, the flexibility in design by varying the absorber thickness and number of stages leads to optimized device performance that can exceed the $Hg_{1-x}Cd_xTe$ photodetectors in meeting specific applications that requires high operating temperature and high response speed.

The detailed theory of ICIPs and their operating mechanism will be discussed in the next chapter, but first I will introduce the IR radiation and the related applications, and an overview of IR detectors is described as well.

1.2 Infrared radiation

Infrared (IR) radiation is an electromagnetic radiation with a wavelength that spans from 700 nm to 1 mm (frequency range of 300 GHz to 430 THz), which is longer than those of visible light (400-700 nm), and is therefore invisible. IR radiation is part of the blackbody (an object at certain temperature above 0 K) radiation spectrum and the spectral radiance can be described by Planck's Law:

$$B_\lambda\left(\lambda,T\right)=\frac{2hc^2}{\lambda^5}\frac{1}{e^{\frac{hc}{\lambda k_B T}}-1}\ , \tag{1.1}$$

where T, h, k_B, c, and λ are the temperature of the blackbody surface, Planck's constant, Boltzmann's constant, the speed of light in vacuum, and the wavelength, respectively. The Sun is an excellent example of a blackbody with a surface temperature around 5800 K. As can been seen from Fig. 1.1, the peak of sun's emission falls in the visible region. Obviously, the radiation spectrum varies with objects at different temperatures. When below 3000 K, the IR band covers most of the total radiation.

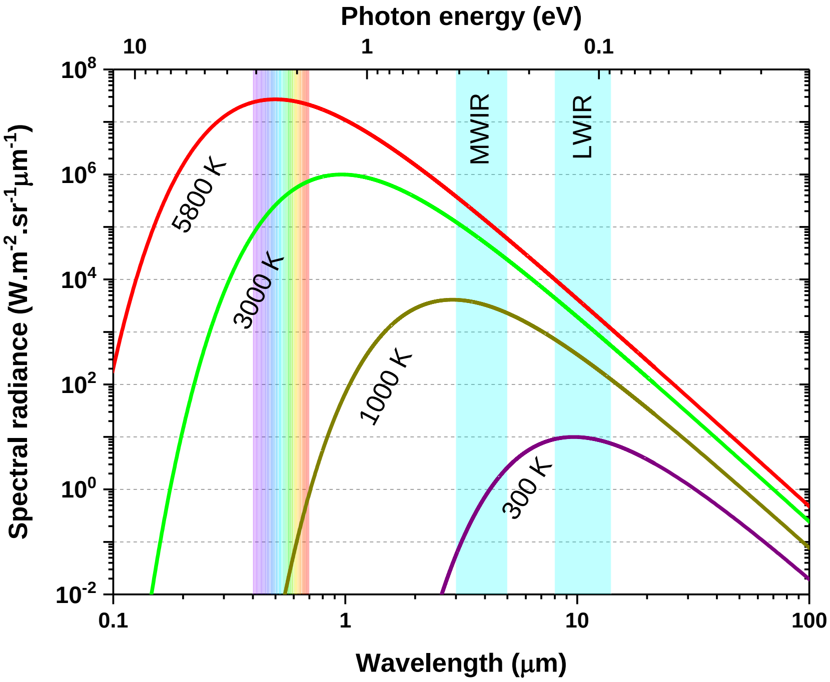

Figure 1.1: Spectral radiance for a blackbody at different temperatures.

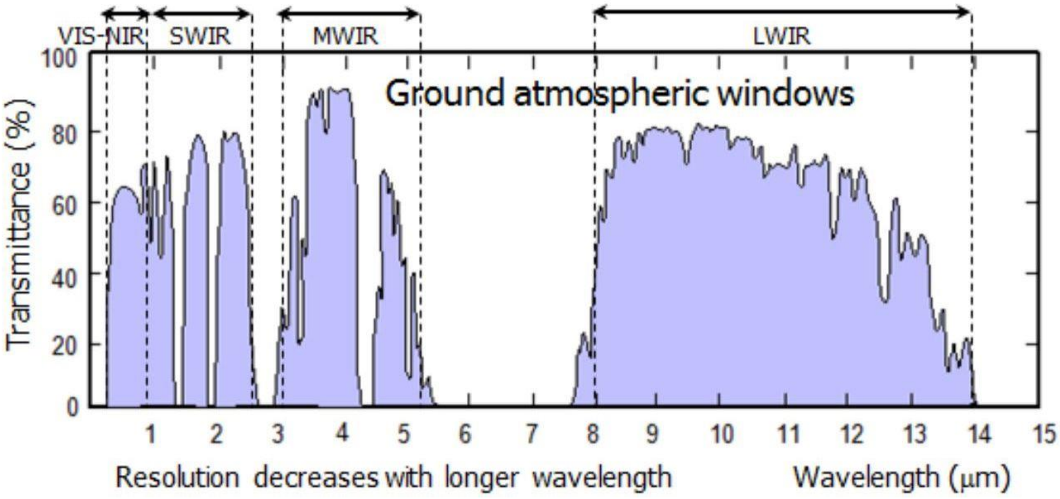

Figure 1.2: Atmospheric transmittance spectrum of IR radiation [17].

The IR band covers a wide range of wavelengths which can be divided into near-infrared (NIR, 0.7-1 µm), short-wavelength infrared (SWIR, 1-3 µm), mid-wavelength infrared (MWIR, 3-5 µm), long-wavelength infrared (LWIR, 8-14 µm), very long-wavelength (VLWIR, 14-30 µm) band and far-infrared (FIR, 30-1000 µm) based on the response of various detectors. Thermal imaging utilizes the photons with wavelength in the IR bands, the NIR-SWIR bands are similar to visible light which make them good for imaging scenes that reflect light, while the MWIR-LWIR wavebands are important for the imaging of objects that emit thermal radiation and are most used in night vision. However, if the radiation is not in vacuum, there are many types of molecules in the air that will absorb photons at particular wavelengths in the IR band. As shown in Fig. 1.2 for the terrestrial IR bands, the atmospheric transmittance presents multiple dips caused by strong molecular absorptions in air. Therefore, in addition to thermal imaging, IR bands are important for gas sensing of water moisture, methane, carbon dioxide, carbon monoxide, etc., as shown in Fig. 1.3. However, applications of IR on Earth will avoid usually those absorption regions and most of the them are focused on MWIR and LWIR bands.

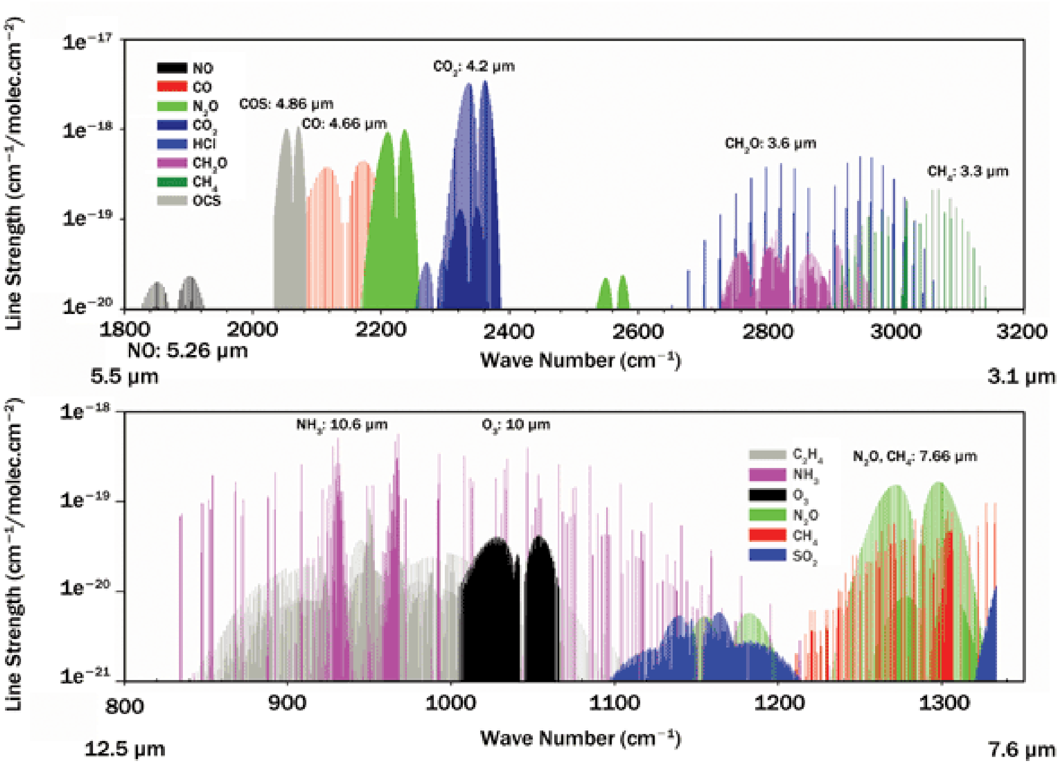

Figure 1.3: HITRAN simulation of absorption spectra for major atmospheric species from 3.1 to 12.5 µm [18].

1.3 Infrared detectors

1.3.1 Background

While the discovery of infrared radiation dates back over 200 years, it was not until the late 20th century that we were able to explore it for use with in modern physics and fast developed technologies, as partially shown in Fig. 1.4 for the development of IR detectors. IR radiation is less absorbed and scattered in the atmosphere compare to visible light and provides important information about objects, such as their temperature, geometry, composition, location in space, and environment. One of the most advanced applications of IR radiation is infrared detectors, which are sensors of infrared photons that convert an optical signal to an electrical signal. IR detectors have potential applications in astronomy, meteorology, climatology, medicine, and the military. They can be used for gas sensing, thermal imaging, night vision, hyperspectral imaging, infrared tracing, etc.

There are two main categories of infrared detectors: thermal detectors and photon detectors (photodetectors). In thermal detectors, the absorption of incident photons increases the temperature of the detector element, resulting in a change in an electrical property of the detector such as its resistivity or capacitance. In photodetectors, the IR photons absorbed in a semiconductor material generate electron-hole pairs and the output current or voltage can be measured. Generally, the response of thermal detectors is independent of the radiation wavelength and the sensitivity relies on the material and structure design. Typical thermal detectors include thermocouples, thermopiles, bolometers and pyroelectric detectors. They are low cost and require no cooling, but their slow response times and low sensitivities limit their applications.

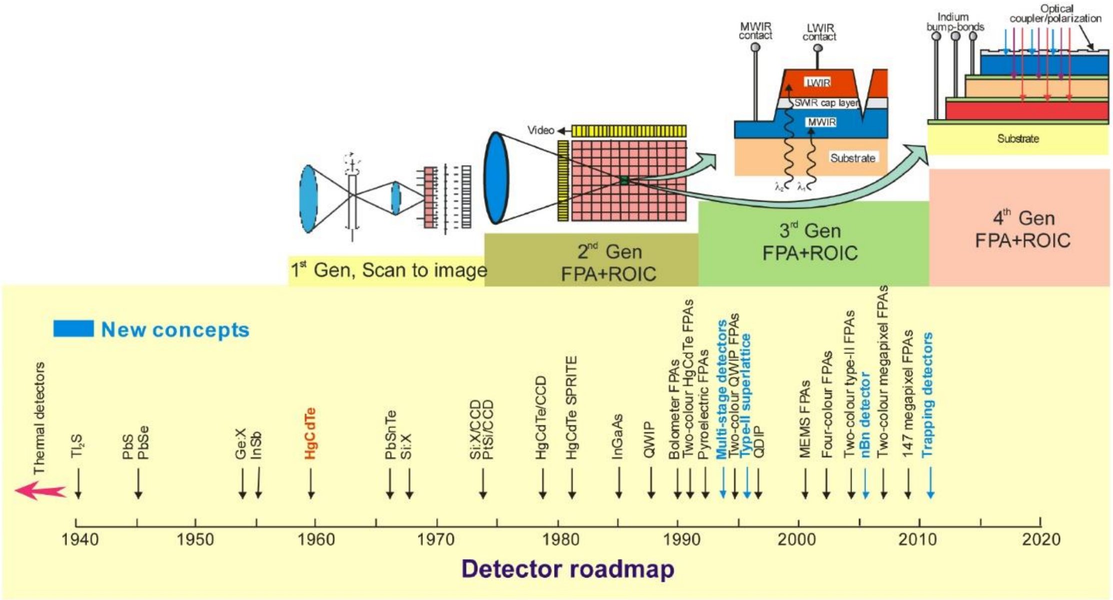

Figure 1.4: History of the development of infrared detectors and systems [19].

On the other hand, photodetectors provide faster response speeds and higher sensitivities. However, most of them require a cryogenic cooling system to obtain high performance which considerably increases the package size and expense. Nevertheless, many IR applications do need high response and high sensitivity, such as gas sensing and night vison such that photodetectors have attracted more interests. Therefore, the improvement of HOT photodetectors works at room temperature or thermoelectrically cooled temperatures have been the general trend for practical applications.

1.3.2 Photodetectors

There are various types of photodetectors, and several figures of merit are used to characterize their performance. The output of a photodetector includes its response signal to the incident radiation and random noise fluctuations, with the ultimate performance of a photodetector being its signal to noise ratio (SNR). A primary figure of merit is the responsivity which is defined as the ratio of photo-generated current or voltage to the incident optical power on the photodetector:

$$R_i = \frac{I_{ph}}{P_{inc}} \text{ or } R_V = \frac{V_{ph}}{P_{inc}} \ , \tag{1.2}$$

where R_i, R_v, I_ph, V_ph, and P_inc are the device current response, voltage response, photocurrent, photovoltage, and incident power, respectively.

Similar to responsivity, another figure of merit widely used in the detector community is quantum efficiency (η) which is defined as the number of photo-generated carriers per incident photon:

$$\eta = \frac{I_{ph}/e}{P_{inc}/hv} = R_i \frac{hc}{e\lambda} = R_i \frac{1.24}{\lambda} \ , \tag{1.3}$$

where e, h, c, v and λ are the electronic charge, Planck's constant, speed of light, frequency and wavelength of the incident photon in µm. Basically, the quantum efficiency judges the device's ability to convert incident radiation into electrical output and is related to the absorption coefficient of the material. Regardless of material defects, the radiation power after the absorption of photons in the detector is given by:

$$P_{absorption} = (1-R)P_{inc}e^{-\alpha d} \ , \tag{1.4}$$

where R is the reflectance at the device surface, α and d are the absorption coefficient and thickness of active material of the detector. Assuming every absorbed photon generates one electron-hole pair and all of the photo-generated carriers can be fully collected at the device contacts, the quantum efficiency can be alternatively expressed as:

$$\eta = \frac{(1-R)P_{inc} - P_{absorption}}{P_{inc}} = (1-R)(1-e^{-\alpha d}) \ , \tag{1.5}$$

The random fluctuations in a detector's output limit its sensitivity to a certain minimum detectable power. There are several noise sources presented in photodetectors, such as Johnson noise, shot noise, 1/*f* noise, and generation-recombination noise, as will be briefly described below [20]:

Johnson noise (also called thermal noise) is due to the random thermal motions (Brownian motion) of electrons inside the device material. It occurs across the bandwidth of the detector, so it is a white noise and therefore independent of frequency. Johnson noise is inherent to all resistive devices and is defined by:

$$i_{n,Johnson}^{2} = \frac{4k_B T}{R}\Delta f \ , \tag{1.6}$$

where k_B, T, R and Δf are Boltzmann constant, absolute temperature, device resistance, and measurement bandwidth, respectively.

Shot noise is another white noise that exists in photodetectors. It is related incident photons arriving at random time intervals, which follow a Poisson distribution. As a result, the photo-generated carriers contain similar fluctuations. Hence shot noise is induced by the varied photocurrent at different time interval and is described as:

$$i_{n,shot}^{2} = 2eI\Delta f \ , \tag{1.7}$$

where e is the electronic charge, I is the device current that contains noises from the signal, background and dark current.

1/*f* noise is frequency dependent and is more dominant at low frequencies (<100 Hz). It is complicated and is usually measured with a spectrum analyzer. The origin of 1/*f* noise is not fully understood yet.

Generation-recombination noise is another type of electrical signal noise caused by the statistical fluctuation of the generation and recombination of electrons in photodetectors, and one expression of generation-recombination noise follows the equation [21]:

$$i_{n,gr}^2 = 2(G+R)e^2 g^2 d\Delta f \ , \tag{1.8}$$

where G and R are the generation and recombination rates, g and d are the noise gain and the thickness of the detector.

There are also some other sources of noise. For example, $1/f^2$ noise is a derivative of $1/f$ noise and it is observed mainly in the metal interconnections of an integrated circuit. The total noise current in a detector can be written as:

$$i_n = \left(i_{n,Johnson}^2 + i_{n,shot}^2 + i_{n,1/f}^2 + i_{n,gr}^2\right)^{1/2}, \tag{1.9}$$

The noise equivalent power (NEP) is defined as the signal power needed to generate an output signal that is equal to the noise and is expressed as $NEP = i_n / R_i$. The inverse of NEP is referred to as the detectivity, which represents the sensitivity of a photodetector. In order to specify the performance of a detector and make reasonable comparisons among different detectors, the specific detectivity (D^*) is often used by normalizing the bandwidth to 1 Hz and the device area to 1 cm^2.

$$D^* = \frac{\sqrt{A\Delta f}}{NEP} = \frac{R_i\sqrt{A\Delta f}}{i_n} \ , \tag{1.10}$$

here A denotes the device area. When Johnson and shot noises are dominant, the detectivity can be written as:

$$D^* = \frac{R_i}{\sqrt{\dfrac{4k_BT}{RA} + 2qJ}} \ , \tag{1.11}$$

where R_i, RA, q, and J are the device responsivity, resistance and area product, electronic charge, and current density, respectively. Since background radiation is unavoidable, when the background photon flux is much greater than the signal flux, the photodetector is in a background-limited infrared performance (BLIP) condition. The background limited detectivity for a photovoltaic detector is given by:

$$D^*_{BLIP} = \frac{R_i}{\sqrt{2\eta q^2 \phi_B}} = \frac{\lambda}{hc}\sqrt{\frac{\eta}{2\phi_B}} \,, \tag{1.12}$$

when it is shot noise limited, where η and ϕ_B are the quantum efficiency and background incident photon flux, respectively. The D^*_BLIP for photoconductive detectors is $\sqrt{2}$ times lower than for photovoltaic detectors which are generation-recombination noise limited where the two processes are uncorrelated.

1.3.3 Characterization of photodetectors

In order to evaluate the performance of a photodetector, we need to know its electrical and optical properties. The electrical performance can be obtained by exploring the current-voltage characteristics (*IV* curves) at different temperatures from which the current and resistance of the device can be extracted. Dark current is obtained by using a cold shield around the device. Dark current density (J_d) and product of resistance (R_0A) and area are the measurable parameters to evaluate the Johnson noise. Since the current measured under illumination contains photoexcited carriers from background radiation and source signal, when under a certain bias, the shot noise would be the dominant noise for some detectors. In addition to noise estimation, *IV* curves can reveal other properties such as carrier transport mechanisms and surface leakage current.

To identify the dominant carrier transport mechanisms, J_d or the R_0A were measured over a wide range of temperature (T) for representative devices and fit according to the modified Arrhenius equation:

$$R_0 A = CT^{-q} e^{\frac{E_a}{k_B T}} \text{, or } J_d = CT^{q} e^{-\frac{E_a}{k_B T}} \text{,} \tag{1.13}$$

where E_a is an activation energy, k_B the Boltzmann constant and C is a prefactor. The additional parameter, q, is expected to be 1 if the dark current scales with intrinsic carrier density n_i (generation-recombination limited), and 2 if it scales with n_i^2 (diffusion limited) [22-24]. As a simple approximation, q=0 is used for general estimation.

If the current density-voltage (JV) characteristics are sensitive to device size, reflected by the inverse product of zero-bias resistance (R_0) and device area (A) as a function of their perimeter–to-area ratio (P/A), the contributions of bulk and surface currents to R_0A can be separated by fitting the device's R_0A to the equation [25]:

$$\frac{1}{R_0 A} = \frac{1}{(R_0 A)_{Bulk}} + \frac{1}{\rho_{sw}}\left(\frac{P}{A}\right), \tag{1.14}$$

where ρ_{sw} is the device sidewall resistivity. From fitting the data, one can estimate the bulk R_0A and the surface contribution to the overall current at different temperatures.

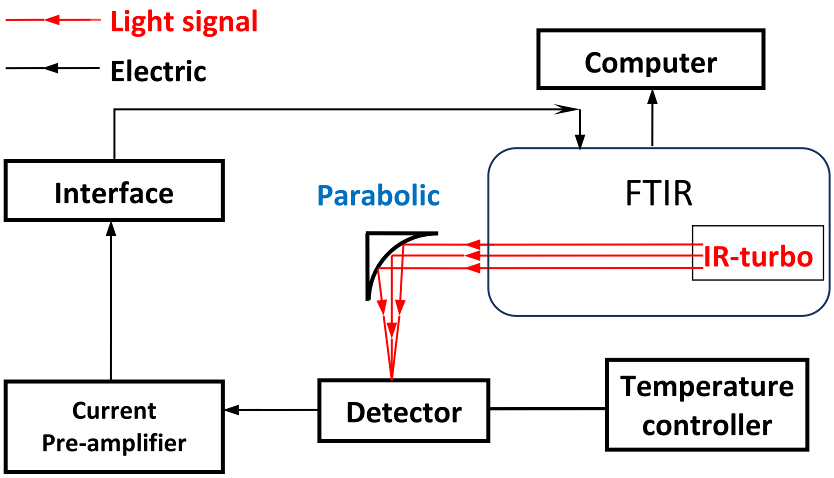

Figure 1.5: Experimental setup to obtain the relative response spectra of infrared photodetectors.

In order to determine the responsivity for an infrared detector, one may first measure the relative response spectrum which can be obtained with an Fourier-transform infrared spectroscopy (FTIR). The experimental setup is shown in Fig. 1.5.

From the response curve at different temperatures, one can obtain the cutoff wavelength or bandgap of the device at each temperature. The temperature dependence of the bandgap is estimated using the Varshni formula [26]:

$$E_g(T) = E_g(T=0) - \frac{\alpha T^2}{\beta + T}, \tag{1.15}$$

where E_g (T=0) is the extracted zero-temperature bandgap, α and β are the Varshni parameters.

The raw response spectrum is relative, so one may want to use a blackbody source to calibrate it into absolute responsivity. By using the setup shown in Fig. 1.6, the photocurrent of the detector can be measured.

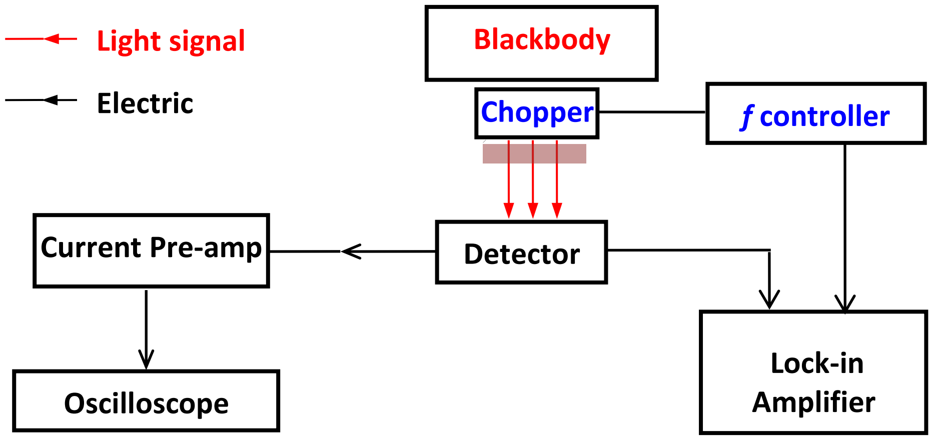

Figure 1.6: Experimental setup to obtain photocurrent of infrared photodetector under chopped blackbody radiation.

Knowing the blackbody temperature, one can calibrate the responsivity with the measured parameters:

$$I_{ph} = N \int R_{rel}(\lambda) P_{inc}(T, \lambda) d\lambda \, , \tag{1.16}$$

where N is the normalization factor, $R_{\mathrm{rel}}(\lambda)$ is the relative response, and $P_{\mathrm{inc}}(T, \lambda)$ is the spectrum of radiant power on the device surface per unit wavelength as given in Eq. 1.1. Thus, the responsivity can be obtained as:

$$R_i(\lambda) = N \times R_{rel}(\lambda) \, , \tag{1.17}$$

According to Eqs. 1.10 and 1.11, one can estimate the detectivity of the detector based on the measured parameters.

1.3.4 Different types of photodetectors

Depending on the operating principle, photodetectors can be photoconductive (PC) detectors, photovoltaic (PV) detectors, and avalanche photodiodes (APDs). PV detectors (or photoconductors) are typically made of semiconductor materials whose resistance is reduced under illumination. This is attributed to the free carriers generated by the absorption of incident photons that increase the conductivity. PV detectors are generally made of *pn* junctions or heterostructures in which the photo-generated carriers can be extracted to the external circuit through either diffusion or drift. In both PV and PC detectors, one incident photon generally creates zero or one electron-hole pair for a quantum efficiency less than unity. On the other hand, in avalanche photodiodes, multiple excitations can occur through impact ionization for a quantum efficiency that can exceed 100%.

The existing photodetector technologies include *pn* junction photodiodes, quantum well infrared photodetectors (QWIPs), quantum dot infrared photodetectors (QDIPs), quantum cascade detectors (QCDs), barrier detectors, and interband cascade infrared photodetectors (ICIPs).

1.3.4.1 pn junction photodiodes

The *pn* junction is the most widely used structure for photodetectors because of its relatively easy growth with mature materials like Si, InSb, HgCdTe, and InGaAs [27]. A *pn* junction is formed by doping adjacent regions of a semiconductor with excess donor and acceptor atoms, respectively. The material can be either a semiconductor or a type of superlattice. Generally, A *pn* junction photodiode is operated under a reverse bias such that the photo-generated carriers can be collected by electrical drifting before they recombine. While the incident photons can be absorbed in all the regions, only the photo-generated carriers in the depletion region and the ones within a diffusion length of the depletion region can be effectively collected. The photo-generated electron-hole pairs beyond this region, in the absence of electric field, do not separate and will therefore more easily recombine, and make no contribution to the photocurrent and reducing the quantum efficiency.

The *pn* junction photodiodes have two drawbacks: The narrow depletion region limits the quantum efficiency; The high depletion layer capacitance causes problems at high modulation frequencies. To overcome these issues, the modified structure known as a *pin* photodiode was introduced by inserting an intrinsic layer between the *p*- and *n*-type doped regions, as shown in Fig. 1.7. The intrinsic layer can be made thick enough to ensure sufficient absorption and collection. On the other hand, such a thick layer also exhibits a uniform electrical field and results in a reduced depletion layer capacitance.

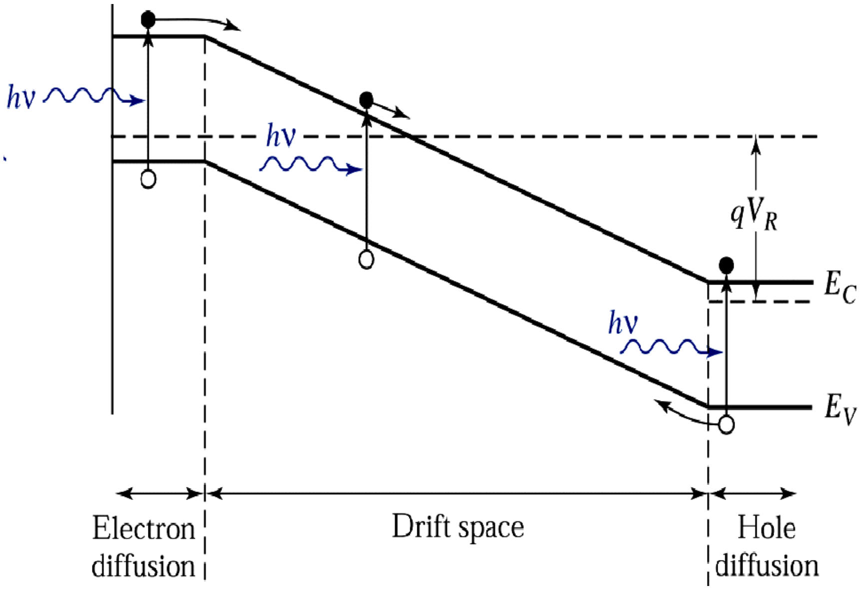

Figure 1.7: Energy band diagram of a *pin* photodiode under reverse bias [28].

1.3.4.2 Quantum well infrared photodetectors

The quantum well infrared photodetector (QWIP) was first introduced in 1987 by using intersubband transitions in resonant tunneling GaAs/AlGaAs superlattices [29], and QWIPs can be photovoltaic or photoconductive [30,31]. While the photoconductive QWIPs are much more popular and widely used, the photovoltaic QWIPs have been less developed and were overwhelmed by the development of quantum cascade detectors.

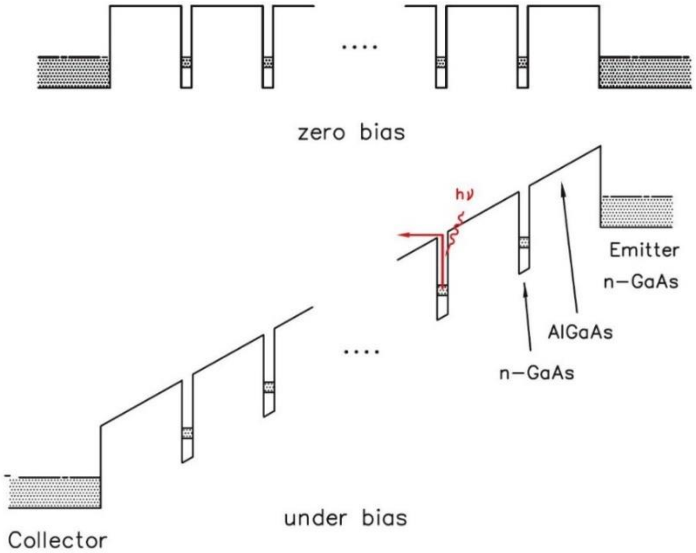

Figure 1.8: Schematic diagram of a bound to continuum photoconductive QWIP under zero and finite bias [31].

QWIPs are made of multiple identical quantum wells (QWs) separated by significantly thicker barriers to avoid coupling between QWs, and the intersubband transition in each QW is either bound-to-bound or bound-to-continuum. The operation principle can be seen from Fig. 1.8 for a widely used bound-to-continuum photoconductive QWIP under a certain bias. The incident photons are absorbed in each QW simultaneously where multiple photons are required to generate one electron that can be extracted to the emitter and collector contacts. Consequently, the quantum efficiency for a QWIP is much lower than conventional detectors. However, the photoconductive gain presented in QWIPs can substantially enhance the output current, where the photoconductive gain is simply defined as the ratio of carrier lifetime (τ) to total transit time [31],

$$g_{\text{photo}} = \frac{\tau + \tau_{\text{trans}}}{\tau_{\text{trans}}} \frac{1}{N} \approx \frac{\tau}{\tau_{\text{trans,tot}}}, \tag{1.18}$$

for the case $\tau \gg \tau_{\text{trans}}$, where N is the number of QWs in the QWIP, τ_{trans} is the transit time for an electron across one quantum well region or the period of the structure. Thanks to the tunable QW, QWIPs have been investigated for a wide range of wavelengths (3-80 µm) for MWIR to VLWIR applications. However, QWIPs typically have a narrow spectral response range (see Fig. 1.9) and work at liquid nitrogen temperature (77 K) to achieve high performance. Another limitation of *n*-type QWIPs is that, due to the selection rules of intersubband transitions, they are not sensitive to normal incidence and usually require specific device mounting or gratings.

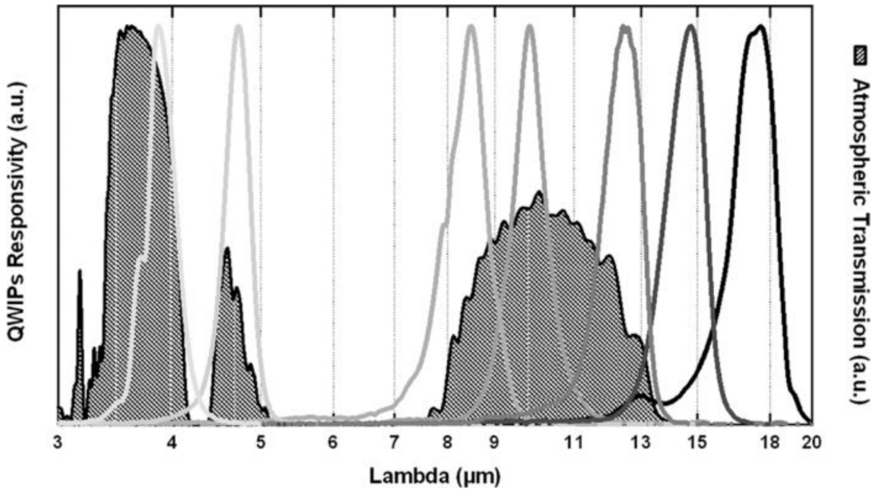

Figure 1.9: Experimental QWIPs responsivities (lines) at different wavelengths demonstrated at Ecole Polytechnique [32,33].

1.3.4.3 Quantum dot infrared photodetectors

Quantum dot infrared photodetectors (QDIPs) were promoted by the development of quantum dot lasers [34,35] and the success of QWIPs stimulated the development of QDIPs, and the first QDIP was demonstrated in 1988 [36]. Following this, there was a rapid development over the last 30 years and QDIPs have emerged as a competitive technology among various types of detectors. Though there are several heterostructure designs for QDIPs [37,38], the main material system is based on InAs QDs grown on a GaAs substrate where the schematic view of the quantum dot array and band structure can be seen from Fig. 1.10. As a result of the three-dimensional confinement in the quantum dots, QDIPs have several advantages such as low dark current, high photoconductive gain and responsivity, and high operating temperatures [39]. They are similar to QWIPs but with two-dimensional quantum wells replaced by zero-dimensional quantum dots. The detection mechanism in QDIPs is also based on intersubband transitions between the quantized energy levels of the dots and continuum states, but they are sensitive to normaly incident radiation [38,40]. Similarly, QDIPs are able to cover a wide spectral range for MWIR and LWIR band sensing and imaging by adjusting the quantum dot size/shape or strain and material composition. However, QDIPs typically have a low quantum efficiency due to the limited quantum dot absorption layer thickness.

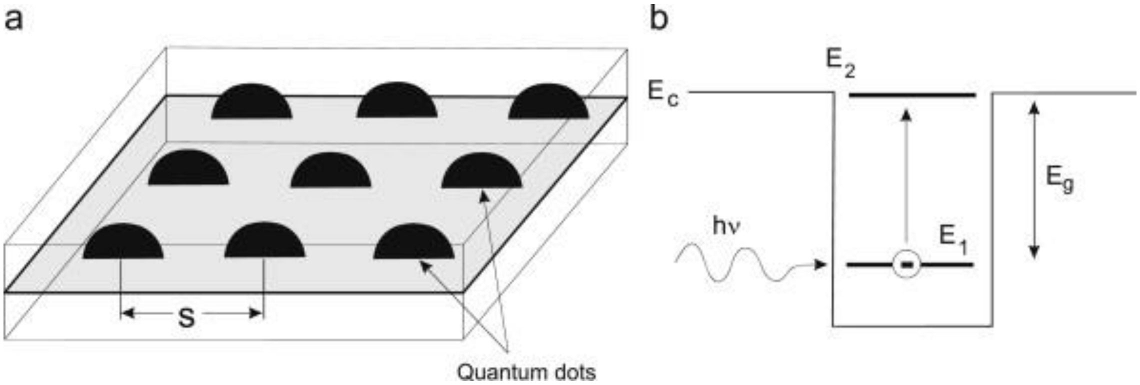

Figure 1.10: Schematic view of (a) the quantum-dot array and (b) conduction band structure of the dot [38,41].

1.3.4.4 Quantum cascade detectors

Quantum cascade detectors (QCDs) are similar to photovoltaic QWIPs [31,42]. The first QCD was demonstrated with a quantum cascade laser (QCL) structure used as a photovoltaic detector [43]. As in the case of QCLs, QCDs can cover a wide range of detection wavelengths from NIR to FIR [44,45] and operate at room temperature with a diagonal transition scheme [46]. As shown in Fig. 1.11, the operating mechanism is through a bound to bound intersubband transition within each identical QW and the photoexcited electrons follow the relaxation process through intraband tunneling within the extractor cascade and then tunnel into the ground state in the adjacent QW. The asymmetric structure of a QCD forces the photocurrent to follow in the desired direction. Compared to QWIPs, the dark current in the QCDs is negligible, leading to a much lower Johnson noise. However, the thin absorbers (active QWs) limit the amount of absorption, resulting in a low responsivity. On the other hand, due to the thin absorbers and short transit time, high speed operation of QCDs over tens of GHz has been demonstrated [47-49].

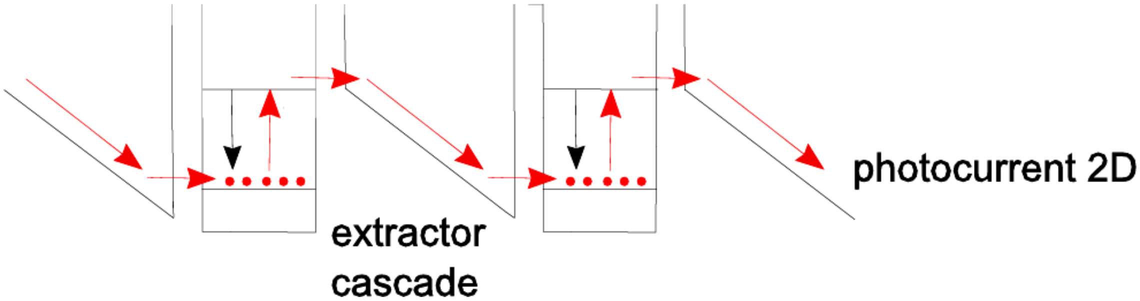

Figure 1.11: Schematic conduction band diagram of a QCD [50]. The extractor cascade is made of digitally graded quantum wells for intraband relaxation of photoexcited electrons.

1.3.4.5 Barrier detectors

Unipolar barriers are widely used in narrow bandgap semiconductors to form barrier photodetectors, including InAs [9,51,52], InAsSb [53-55], HgCdTe [56-58] and InAs/GaSb T2SL [16,59,60] infrared detectors. The unipolar barriers are introduced to block one type of carrier (electrons or holes) and allow the pass of the other, as can be seen from Fig. 1.12. In general, unipolar barriers are used to implement the barrier detector architecture (nBn [9,11,55], XBn [51,53,54], and CBIRD [16,61]) for increasing the collection efficiency of photo-generated carriers and suppressing the generation-recombination dark current associated with the Shockley-Read-Hall process without inhibiting photocurrent flow. Meanwhile, the barriers can also serve to suppress the surface leakage current [11].

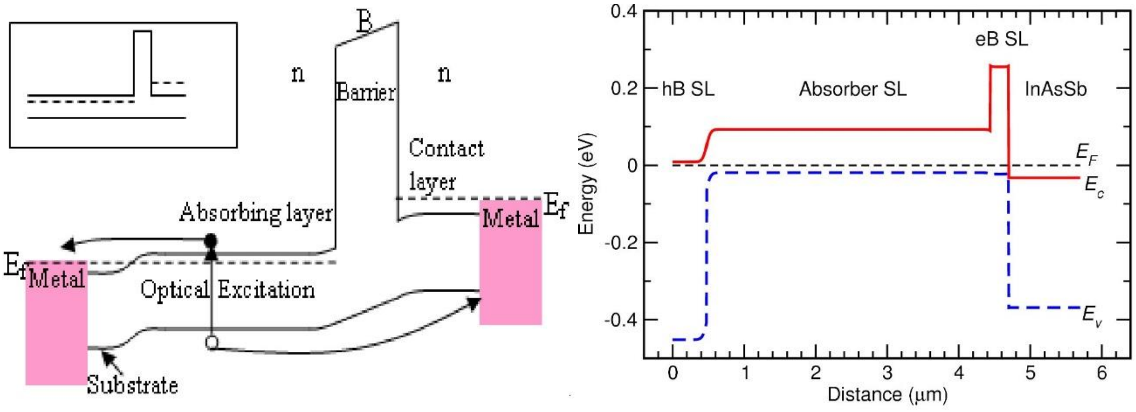

(a) (b)

Figure 1.12: Schematic band diagram of (a) an nBn detector [9] and (b) a complementary barrier infrared detector (CBIRD) [16].

1.4 Objective and scope

The $Hg_{1-x}Cd_xTe$ photodetectors have been a dominant player in the detector market with their advanced device performance. As stated above, several detector technologies have been developed to obtain high device performance and attempt to take the place of $Hg_{1-x}Cd_xTe$ photodetectors, among which ICIPs hold great potential for applications require high temperature operation and high response speed with their unique multi-stage architecture.

In this dissertation, the aim is to develop a series of ICIPs in the MWIR region for high speed operation and in the LWIR for high temperature operation. The MW ICIPs have already been demonstrated to be operated above room temperature (up to 450 K) [62,63], but no work has been done to examine their potential for high speed operation. Therefore, MW ICIPs based on T2L and GaInAsSb absorbers are carried out to pursue high speed operation at room temperature. The preliminary LW ICIPs have touched room temperature operation but with a cutoff wavelength near 8 µm at 300 K [64,65], which is far shorter than the desired cutoff wavelength for applications in the LWIR band. Hence, several sets of LW ICIPs with different structure designs are investigated to attain room temperature operation with a longer cutoff wavelength.

1.5 Dissertation outline

The main focus of this dissertation is on the design, characterization and analysis of interband cascade infrared photodetectors (ICIPs) in the MWIR and LWIR bands. Chapter 2 introduces the background of IR devices with interband cascade structures. The fundamental concept and theory of ICIPs are illustrated, the performance and benefits of ICIPs will be discussed in the following chapters.

Chapter 3 presents on a comparison study of the electrical and optical properties of a set of device structures with different numbers of cascade stages, T2SL absorber thickness, and doping variations, as well as a non-current-matched ICIP structure with equal absorbers.

Chapter 4 shows the demonstration of quaternary GaInAsSb-based MW ICIPs with cutoff wavelengths longer than 4 µm at 300 K. Both ICIPs with a three-stage discrete absorber architecture and conventional one-stage detector structures have been grown by molecular beam epitaxy and investigated in experiments for their electrical and optical properties.

Chapter 5 discusses on a comparison study of LW ICIPs with the goal of an improved understanding that will lead to further increases in the operation temperature. Four sets of detectors are studied including: single absorber barrier detectors, and multi-stage ICIPs with four, six and eight discrete absorbers.

Chapter 6 presents a comparative study of two sets of LW ICIPs based on a InAs/GaSb T2SLs. The devices in one set have a current-matched configuration while those in the other set are non-current-matched.

Chapter 7 investigates the multiple negative differential conductance (NDC) features observed in LW ICIPs at and above 300 K. Using ICIPs with various structures and carrier concentrations, several approaches were employed to demonstrate that the observed multiple NDC features and their unusual temperature dependence are related to the sequential turn off of resonant tunneling of minority carriers through the electron barriers at high temperatures.

Chapter 8 concludes this dissertation and provides suggestions for future research.

Chapter 2 Infrared devices with interband cascade structures

Interband cascade devices include interband cascade lasers (ICLs), ICIPs and interband cascade infrared thermophotovoltaics (ICTPVs). They are made of the III-V semiconductor compounds: InAs, GaSb, and AlSb with lattice constant around 6.1 Å, as described in Fig. 2.1(a). Since they have a zinc blende crystal structure and are nearly lattice matched, it is feasible to grow each of them on either an InAs [66] or a GaSb [67] substrate by using the molecular beam epitaxy (MBE) technique. By virtue of their unique bandgap alignment, they can form band-edge relationships including type-I, type-II staggered and type-II broken-gap. Compared to the type-I QW where the electron and hole wavefunctions are located in the same layer, they are spatially separated and located in different layers in a type-II broken-gap QW, as shown in Fig. 2.1(b). Therefore, the effective bandgap for the InAs/GaSb type-II broken-gap QW can be tuned in a wide range of energies from SWIR to VLWIR bands.

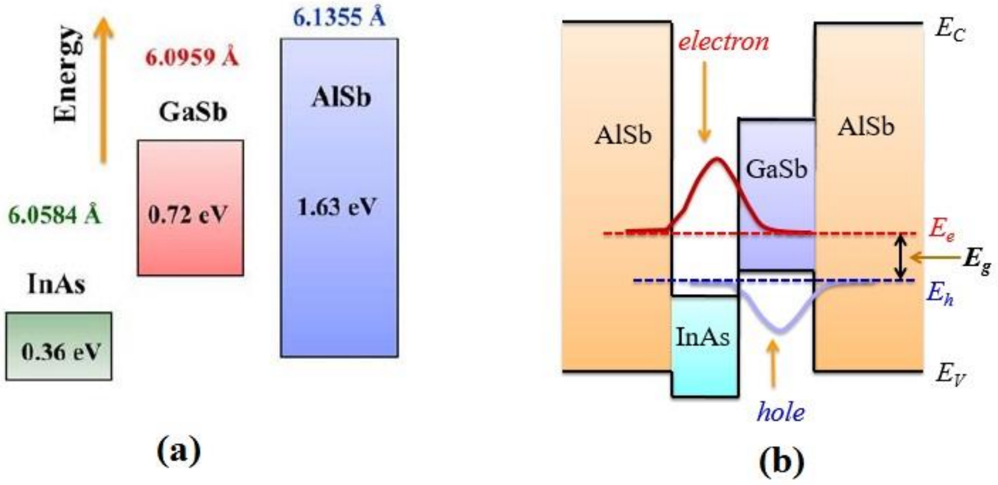

Figure 2.1: (a) Lattice constants and band gap alignment of the III-V 6.1 Å semiconductors. (b) Illustration of a type-II broken-gap QW [68].

While the type-II broken-gap QW is employed as the active region in ICLs, the InAs/GaSb T2SL materials are used as the absorber for the ICIPs and CITPVs. Since the introduction of T2SL in 1977 [69], it has been broadly used to realize different types of electronic and optoelectronic devices such as transistors, lasers, and detectors. The bandgap of T2SL can be tuned in wide range of wavelengths from 2.3 to 30 µm by adjusting the layer' thickness. The slight lattice mismatch (0.6%) between InAs and GaSb can cause sufficient strain build-up in thick InAs/GaSb superlattices that may affect the material quality, therefore, InSb-like interfaces [70] are often used to balance the strain. As mentioned earlier, IR detectors based on T2SL exhibit a reduced tunneling dark current associated with their larger electron effective masses [6] and a suppression of Auger recombination [7,8].

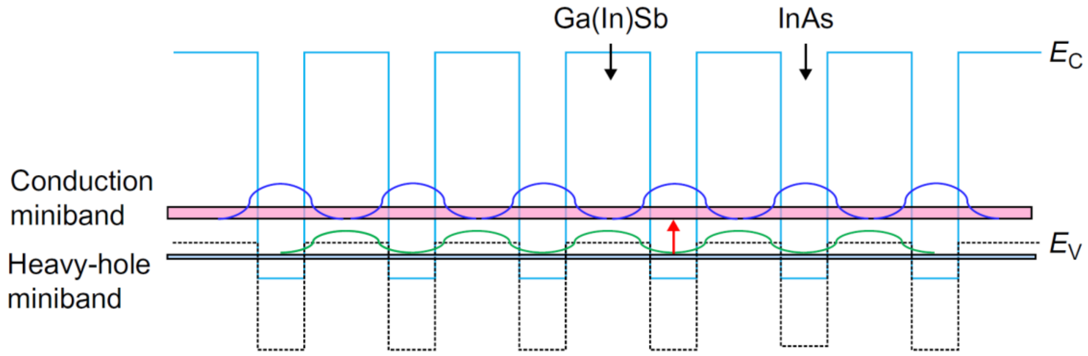

Figure 2.2: Schematic illustration of an InAs/Ga(In)Sb type-II broken-gap superlattice showing the spatial separation of the conduction band and the heavy-hole band wave functions. The infrared transition is indicated by an arrow [10].

2.1 Interband cascade lasers

Intersubband transitions in a biased superlattice was first proposed by R.F. Kazarinov and R.A. Suris in 1971 [71] for light amplification, Bell group in 1994 demonstrated the first intersubband lasers, i.e. quantum cascade lasers (QCLs) [72]. In the same year, the idea of IC structures for infrared optoelectronics was first proposed [73]. Unlike conventional interband semiconductor lasers that emit photons through recombination of electron-hole pairs across the material band gap, QCLs are unipolar and laser emission is achieved through the use of intersubband transitions in a repeated stack of semiconductor multiple quantum well heterostructures. A few years later, the first ICL was demonstrated in 1997 [74]. The ICLs are similar to the QCLs in terms of the cascade design and band structure engineering. However, rather than using intersubband transitions in QCLs, ICLs utilize interband transitions in a cascade structure, as illustrated in Fig. 2.3.

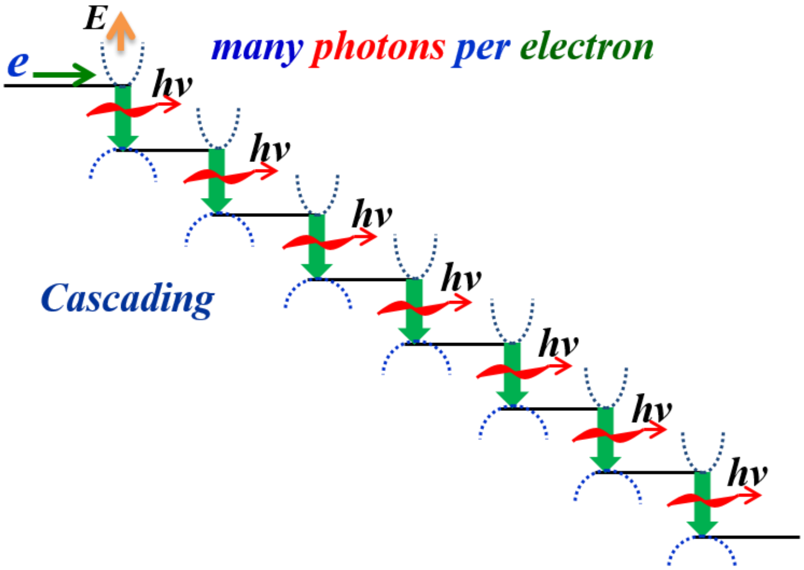

Figure 2.3: Illustration of the interband cascade process [75].

ICLs are made of multiple series-connected cascade stages with each stage containing three regions: the active region, electron injector and hole injector. The band-edge diagram of an ICL is shown in Fig. 2.4. The type-II QW serves as the active region for ICLs, where in this structure the active region is made of an InAs/GaInSb/InAs QW, known as the W structure [76]. Due to the significantly enhanced overlap of electron and hole wavefunctions in the W structure QWs, the corresponding optical matrix element is larger than that of a single InAs/GaSb QW that was used in the early stage of development. Therefore, the gain in each cascade stage is increased with W structure active region. The electron and hole injectors are made of InAs/AlSb and GaSb/AlSb QWs, respectively. To ensure good optical confinement, the cascade regions are sandwiched between the top and bottom cladding layers [77]. Upon current (electrons) injection throng the conduction band of the electron injector to the conduction band of the active region, electrons accumulate in the conduction band of the confined active region until the population inversion is established, then the injected electrons make transitions to the valence band of the active region with net photon gain for lasing. The electrons are swept to the valence band of the hole injector and then are transported to the next stage through interband tunneling facilitated by the type-II broken-gap alignment at the interface of hole and electron injectors. This process will repeat N times if there are N cascade stages in one ICL and the recycling of one injected electron will give rise to N lasing photons, thus high quantum efficiency beyond unity is achieved.

Compared to QCLs, ICLs have much lower injection current due to the much longer carrier lifetime of interband transitions, as such the Ohmic loss is reduced. In addition, ICLs are far more adaptable to apply in vertical-cavity surface-emitting lasers (VCSELs) [67] compared to QCLs due to the different section rules between interband and intersubband transitions.

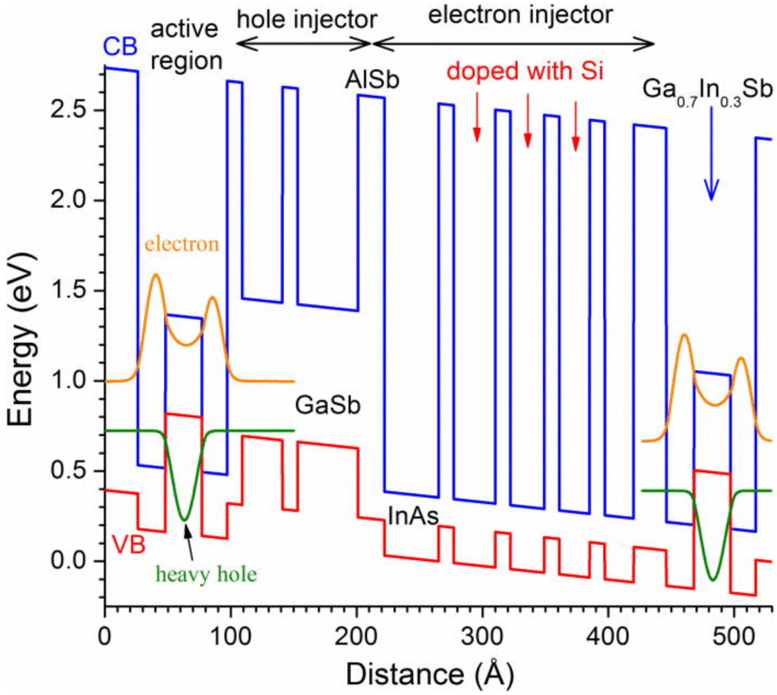

Figure 2.4: Band-edge diagram of one cascade stage in an ICL design [78].

More than 20 years' development of ICLs have demonstrated its promising potential for practical application and market share. At present, ICLs based on type-II QWs have already achieved continuous wave (cw) operation at room temperature with an emission wavelength of 2.8-5.6 μm [79,80]. Also, an ICL based on a type-I InGaAsSb/AlAsSb QW was reported to be able to operate in cw mode at 300 K with a lasing wavelength near 3.2 μm [81].

2.2 Interband cascade infrared photodetectors

2.2.1 Background

Interband cascade infrared photodetectors are similar to ICLs but with the active QW regions replaced with T2SLs for strong absorption. Actually the first ICIP was realized by using an ICL working as a detector in 2005 [82]. Then it was in 2010 the initial comprehensive theory of ICIPs was developed [14] and followed by a more detailed theoretical study in 2013 [83]. Originating from ICLs [73,82,84], ICIPs with T2SL absorbers are a relatively new type of detector. By taking advantage of the broken-gap band alignment in type-II heterostructures, ICIPs can effectively absorb most of the incident photons with their discrete multiple cascade stage architecture and efficiently collect the photo-generated carriers without being limited by the carrier diffusion lengths. Also, noise is significantly suppressed with multiple stages and thin individual absorbers. As such, ICIPs are feasible for high temperature and high-speed operation without compromising detectivity [14,15,83,85]. Preliminary experimental efforts [14,15,62-65,86-91] on ICIPs have shown encouraging results such as operation above room temperature (up to 450 K) [62,63] and high-frequency operation (up to 1.3 GHz) [91]. These ICIPs are comprised of InAs/GaSb T2SL absorbers that can be tailored to cover a wide range of the IR spectrum from the SW to very VLW regions [14,15,64,88,90,92-94], and possess the advantages of high uniformity, reduced tunneling currents, and suppressed Auger recombination, as compared to traditional HgCdTe detectors.

The T2SL absorber in each ICIP stage is sandwiched between an electron barrier and a hole barrier, similar to the CBIRD structure [16], as shown in Fig. 2.5. Other than

T2SL, the absorber can be also made of bulk semiconductor materials like the quaternary GaInAsSb alloy [95]. The electron barrier is usually composed of multiple GaSb/AlSb QWs and the hole barrier consists of multiple InAs/AlSb QWs with varied well widths for the different QWs. The two unipolar barriers in each stage rectify the current flow without impeding photo-generated carrier transport in the device, without the presence of a conventional *pn* junction, so that the generation-recombination current (and the corresponding noise) can be reduced.

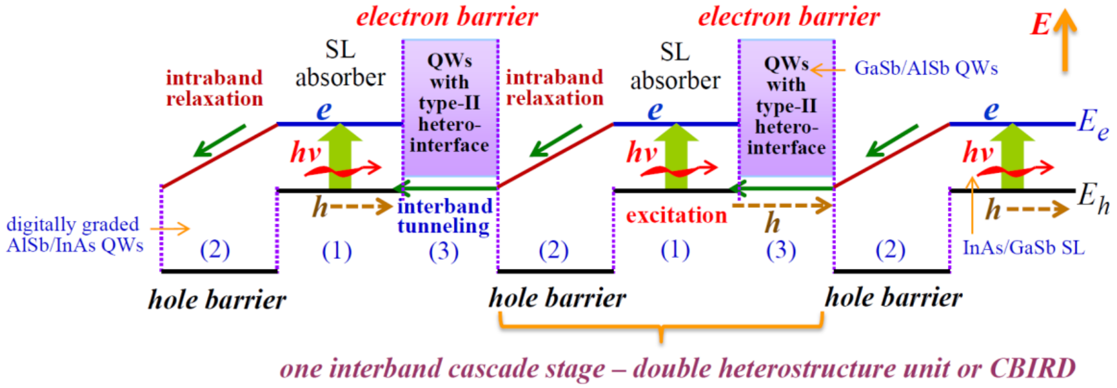

Figure 2.5: Schematic structure for an ICIP. Each cascade stage is made of three regions: (1) T2SL absorber, (2) hole barrier, and (3) electron barrier.

2.2.2 Illumination configurations

There are two illumination configurations for the ICIPs based on the directions of incident light and photo-generated electrons flow in the conduction band of the absorbers, and light is incident on the top surface of the device [65]. When they have the same direction, ICIPs are classified into regular (reg.) illumination configurations; when they have opposite directions, ICIPs are classified into reverse (rev.) illumination, as shown in Fig. 2.6(a) and (b). In the regular configuration, most of the photo-generated electrons in the absorber are close to the electron barrier that they need

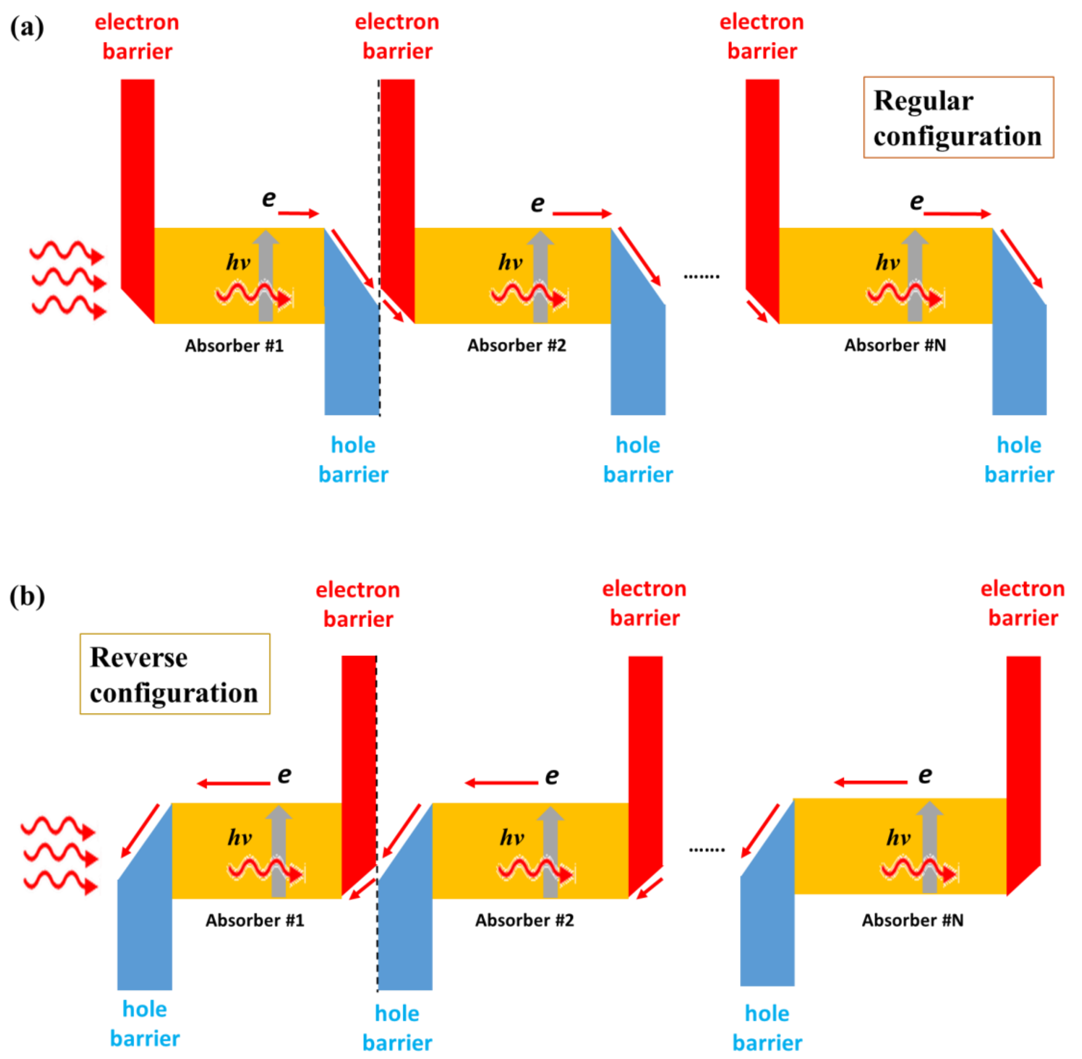

Figure 2.6: Schematic energy band structure of a multi-stage ICIP with (a) regular and (b) reverse illumination configurations. The two illumination configurations can be realized by reversing the growth order of layers in one structure without changing the light illumination direction.

to travel (through diffusion under zero bias) relatively long distance for the collection at the hole barrier. However, if the diffusion length is less than the thickness of the absorbers especially when operating at high temperatures and/or in the LWIR region, most of the photo-generated electrons recombine before reaching the collecting point. To overcome this issue, the reverse configuration structure was introduced by reversing the growth order of the regular configuration structure. In the revers configuration, most of the photo-generated electrons are closed to the hole barrier and hence can be effectively collected without travelling a long distance. When the diffusion length is much longer than the thickness of the absorbers, both configurations could approach 100% collection efficiency of the photo-generated carriers. However, if the diffusion length becomes shorter than the thickness of the absorbers, the reverse configuration is expected to have superior collection efficiency because photo-generated electrons are more efficiently collected for *p*-type absorbers, as indicated by the theoretical projections [83] shown in Fig. 2.7. Therefore, the reverse configuration is generally preferred as the ICIP structure.

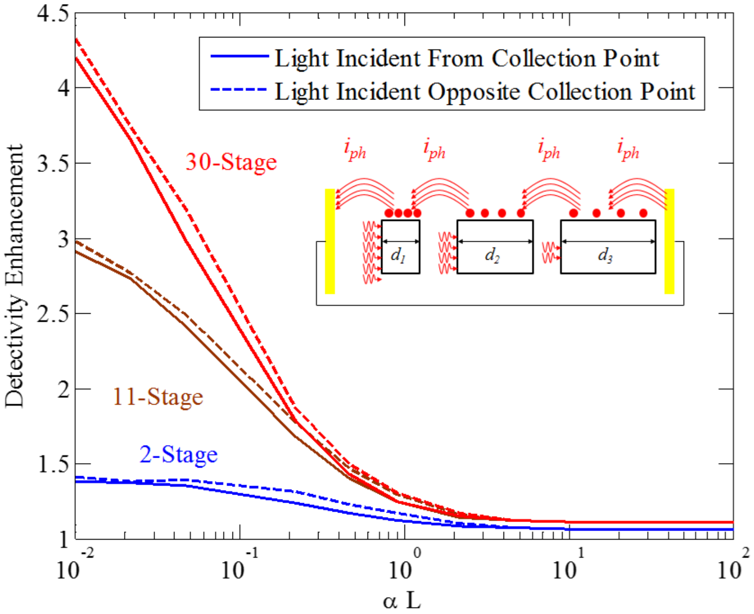

Figure 2.7: Theoretical zero-bias detectivity enhancement for 2-stage, 11-stage, and 30-stage photocurrent-matched multiple-stage ICIPs operating the thermal noise limit [83].

2.2.3 Comparison between single-absorber detectors and ICIPs

One of the fundamental benefits of ICIPs is noise reduction in both Johnson noise and shot noise. The Johnson noise reduction is inherent to ICIPs in terms of the large resistance caused by the series-connected short cascade stages. As mentioned in the previous section, shot noise is related to the random incident photons in terms of arriving time that follows a Poisson distribution. In a more general sense, any random fluctuations in the arrival time of electrons to the collecting contacts can be treated as shot noise. This can be caused by the fluctuations within interband transitions triggered by radiations from signal source and background, as well as the random thermal generation in the absorber. Consider a single stage detector, these fluctuations will be preserved as long as the electrons reach the collection points. However, in an ICIP, since these fluctuations among different stages are simultaneous and independent, in order to maintain the current continuity through the device to external circuit, the fluctuations in each absorber hence are forced to narrow down to an average range. Therefore, the shot noise will be reduced by a factor of N_C if there are N_C cascade stages in the ICIP. The suppression for the shot noise is because the added number of required transition for an electron, similar to how additional trials in an experiment reduces the uncertainty in the measurement [96]. It is also similar to the noise reduction in QWIPs with intersubband transitions [97,98]. Thus, the expression of specific detectivity for an ICIP should be modified according to Eq. 1.11:

$$D^* = \frac{R_\lambda}{\sqrt{\dfrac{4K_BT}{R_DA} + \dfrac{2qJ}{N_C}}}, \tag{2.1}$$

where R_λ, k_B, T, R_DA, q, and J are the device's responsivity, Boltzmann constant, device temperature, product of device dynamic resistance and area, electron charge, and total current density including a contribution from photocurrent, respectively.

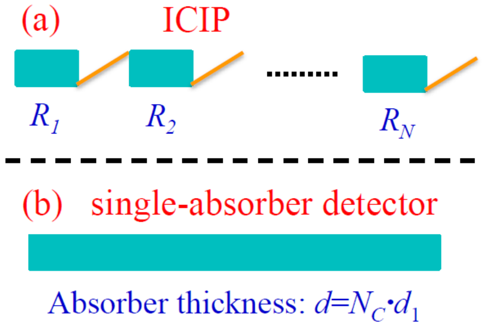

Figure 2.8: Schematics of detectors based on (a) ICIP and (b) single-absorber structures. Their total absorber thicknesses are designed to be the same [99].

The maximum responsivity (and external quantum efficiency) that can be achieved in an ICIP is reduced by the thin individual absorbers and multi-stage architecture. However, this is compensated by the suppression of noise, which has been discussed in previous theories from the perspective of shot noise gain[14,31] and at a fundamental level [83]. Hence, the signal to noise ratio (*i.e.* detectivity D^*) in ICIPs is not reduced; instead it can be enhanced compared to the conventional single-absorber detector. This is further illustrated by considering the D^* for two simplified detectors based on ICIP and the single-absorber structures as shown in Fig. 2.8. In Fig. 2.8(a) there are N_C identical thin absorbers connected in series with the total absorber thickness equal to that of the single-absorber detector in Fig. 2.8(b), resulting in a total resistance of $R=N_C\cdot R_1= N_C^2\cdot R_{single}$, where R_1 is the resistance of an individual absorber of ICIP, and R_{single} is the resistance of the single-absorber detector. Meanwhile, the current of the ICIP then will be N_C times smaller, $J_1=J_{single}/ N_C$. Suppose the light attenuation is negligible in the absorbers and there is a perfect collection of photo-generated carriers. Because the absorber thickness d in Fig. 2.8(b) is N_C times d_1 (the individual absorber thickness of the ICIP), the responsivity of the single-absorber detector is $R_{\lambda,\text{ single}}=N_C\cdot R_{\lambda 1}$, where $R_{\lambda 1}$ is the responsivity of the ICIP. Consequently, the detectivities for the single-absorber detector and ICIP are

$$D^*_{\text{ICIP}}=\frac{R_{\lambda 1}}{\sqrt{\frac{4k_BT}{N_CR_1A}+\frac{2qJ_1}{N_C}}}\propto\sqrt{N_C}$$

$$=\frac{R_{\lambda,\text{ single}}/N_C}{\sqrt{\frac{4k_BT}{N_C^2(R_{D,\text{ single}}A)}+\frac{2q(J_{\text{single}}/N_C)}{N_C}}}=\frac{R_{\lambda,\text{ single}}}{\sqrt{\frac{4k_BT}{R_{D,\text{ single}}A}+2qJ_{\text{single}}}}=D^*_{\text{single}}, \qquad (2.2)$$

Hence, in ideal cases where the diffusion length is infinite and under the first-order approximation shown in Eq. 2.2, the detectivity of an ICIP is proportional to the square root of N_C and equals to a conventional single-absorber detector with an equal total absorber thickness.

In a multi-stage ICIP structure, some photocurrent (*i.e.* signal) is traded for reduced noise. Obviously, this multi-stage discrete absorber architecture would have drawbacks when the circuit and system noise is higher than the device noise, which is most likely the case at very low temperatures. However, for operation at high temperatures where the device noise is generally much higher than the circuit and system noise, the multi-stage discrete absorber architecture would have advantages over the conventional single-absorber detector. This is because the carrier diffusion length at a high temperature is actually shorter than the single absorber thickness (*i.e.* $N_C\cdot d_1$) so that some photo-generated carriers will be recombined before being collected in the circuit, resulting in a reduced $R_{\lambda,\text{ single}}$ ($<N_C\cdot R_{\lambda 1}$) and thus a reduced D^* for the

conventional single-absorber detector, which is especially true in the LWIR region with a small absorption coefficient. In contrast, each individual absorber thickness in an ICIP is thinner than the diffusion length, while the sum of the absorber thicknesses can be significantly longer than the diffusion length and the single-absorber thickness in the conventional detector. This results in further noise reduction and an enhanced signal-to-noise ratio (*i.e*. detectivity) over that in the conventional single-absorber detector at high temperatures. Therefore, the device performance for ICIPs is better indicated by the detectivity rather than only by the responsivity or external quantum efficiency, in contrast to conventional detectors with a single absorber. Hence, ICIPs with a discrete absorber architecture should, in principle, perform better than conventional LWIR photodetectors at high temperatures.

2.3 Interband cascade thermophotovoltaic devices

Thermophotovoltaic (TPV) systems [100,101] convert the thermal radiation energy into electricity through the photovoltaic process. TPV systems are clean, quiet and compact power conversion systems and typically consist of a selective emitter, a filter, and a photovoltaic cell. A selective emitter is typically made of rare earth oxides [102,103] that absorb the radiation from the heat source, and reradiates photons with spectral sharping to increase the conversion efficiency by suppressing sub-bandgap photon emission and enhancing photon emission with energies larger than the bandgap of the TPV cell. Such broadband absorbers and narrowband emitter had been realized recently by using nanostructured materials and metamaterials [104,105]. In contrast to a typical solar cell, TPV cells are generally placed near a heat source where the radiation intensity is significant higher than one sun. However, the side effect of overheating the TPV cell degrade the conversion efficiency, therefore a cold-side filter is usually put in front of the TPV cell.

While the solar cells are much more popular than TPV systems for power conversion from sun light, there is about two thirds of waste energy as heat loss from world’s heavy industries, particular in steel and glass industries. The recovery of these losses will make a significant impact on energy saving as well as environment protection. Since most of unrecovered waste heat has temperatures below 650 ℃ [106] which radiates in the MWIR range as can be seen from Fig. 1.1, TPV cells with narrow bandgaps (<0.5 eV) have the potential to recover part of these mass energy losses. According to the theoretical projections [107,108], based on the detailed balanced model [109], TPV cells with bandgaps between 0.2-0.4 eV are optimal for a high conversion efficiency of thermal radiations from heat sources with temperatures in the range of 1000-2000 K. However, the development of TPV system is not as fast as expected, and most of the previous study was focused on a single junction structure based on GaInAsSb/GaSb [110-112], InGaAs/InP [113,114] material systems with bandgaps of 0.5 eV or above. Since there’s still large amount of waste energies below 0.5 eV are not utilized for power conversion, narrow bandgap materials are required to absorb these low temperature heat source radiations.

However, TPV systems with narrow bandgap materials suffered several limitations including the relatively low absorption coefficient, short diffusion length, and low open-circuit voltage, resulting in poor conversion efficiencies [100,115]. To circumvent these issues, the concept of ICTPVs was proposed in 2010 [116] as a new

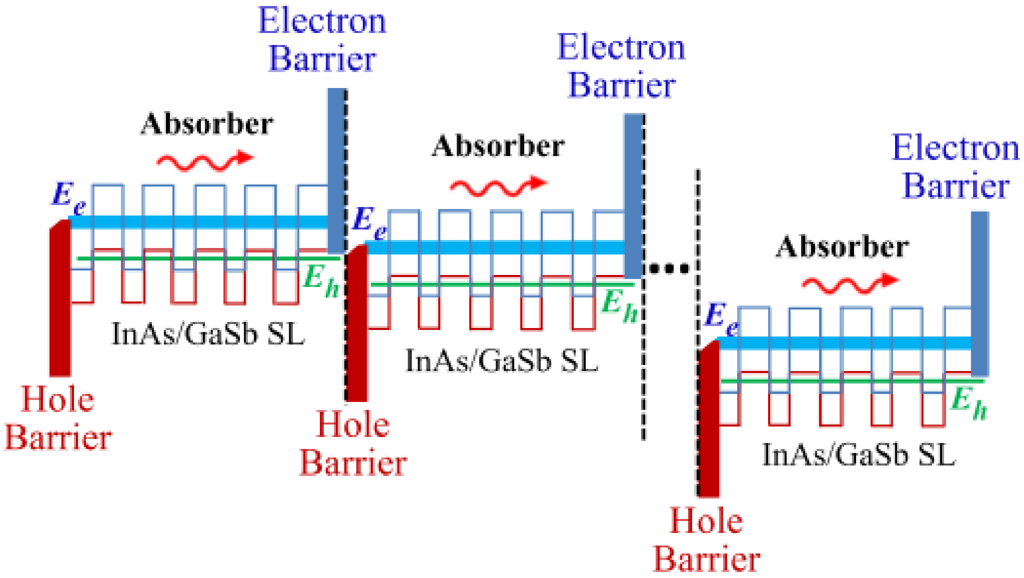

Figure 2.9: Schematic illustration of an ICTPV device with multiple stages. Each stage is composed of a T2SL absorber sandwiched between electron and hole barriers. E_e and E_h denote the energy for electron (light blue) and hole (green) minibands, respectively. The energy difference (E_e-E_h) is the bandgap (E_g) of the T2SL [117].

type of narrow bandgap TPV cells by utilizing multi-stage discreet thin absorber architecture based on interband cascade structure. Basically, the device structure is almost same as ICIPs, ICTPVs operate at a forward bias while ICIPs work under zero or reverse bias, as given in Fig. 2.99 [117]. The absorbers are made of InAs/Ga(In)Sb T2SLs such that the bandgap can be tailored to a desired energy over a wide range of IR bands. The carrier transport between cascade stages is through a type-II broken-gap band alignment between InAs and GaSb layers (Fig. 2.1), resulting a negligible series resistance. In an ICTPV structure, every individual absorber is design thinner than the diffusion length to ensure a high collection efficiency, while the total absorber thickness can be much thicker than the diffusion length to keep enough absorption depth of the incident photons. Another advantage of ICTPVs are the high open-circuit voltage due to the series connected cascaded stages, the preliminary work of our group had demonstrated the high open-circuit voltage exceeding the single-bandgap determined value (E_g/e, where e is electron charge) in ICTPVs [116-122] at room temperature and above. On the other hand, the maximum achievable photocurrent is relative low as the fact of the thin individual absorbers, which is beneficial for reducing Ohmic losses associated with circuit resistance.

Compared to conventional *pn* junction TPV cells, ICTPVs hold much higher open-circuit voltage and lower current densities, while the Ohmic loss due to large current on the series resistance is a big problem for *pn* junction TPV cells with high intensity flux sources. Meanwhile, the dark current is suppressed in the ICTPV by eliminating the depletion region where SRH recombination is a severe issue for narrow bandgap materials. Consider the heat sources are typically broadband, ICTPVs can take advantages from multi-junction solar cells by varying the bandgaps of the absorbers in different cascade stages to enhance the absorption of incident photons and hence increase the conversion efficiency.

Chapter 3 Mid-wavelength interband cascade infrared photodetectors with superlattice absorbers and gain

3.1 Background and motivation

In the previous chapters, the theory and the fundamental benefits of ICIPs have been discussed. As stated, ICIPs with multi-stage design are particular advantageous for high temperature operation with high response speed and high sensitivity. While a reduction of quantum efficiency is typically observed in single stage detectors at such high temperature because of the reduced diffusion length [123,124], MW ICIPs have been reported to work above room temperature [62,63]. Therefore, the single stage detectors are typically operated at low temperature with a thick absorber to ensure a high quantum efficiency with sufficient photon absorption. However, the requirement of cryogenic cooling increases the power consumption, device package size and cost. In the meantime, the response time is limited by the thick absorber. On the other hand, ICIPs with thin discrete absorber design are practicable for high temperature operation with a short transit time. Hence, ICIPs are of great potential for uncooled IR detectors targeted in high speed application.

In this chapter, a series of MW ICIPs are single stage detectors based on T2SL absorbers are investigated. It is expected that the multi-stage ICIPs would outperform over the singe stage detectors at high temperatures in terms of lower noise and higher sensitivity. Also, these ICIPs can be explored for high frequency operation at room temperature.

3.2 Device structure, growth and fabrication

Thirteen detector structures with different numbers of stages and absorber thicknesses were designed to have their cutoff wavelength in the MWIR region. These ICIP structures were grown on nominally undoped *p*-type GaSb substrates. Table 3.1 provides the detailed design parameters for these detector structures and the surface defect density of each grown wafer.

Table 3.1: Summary of design and material parameters for each wafer.

Wafer	Config.	# of stages N_C	Absorber thickness (nm)	Total absorber thickness (nm)	P-type doping in the absorber (cm^{-3})	P-type doping in the buffer layer (cm^{-3})	P-type doping in the substrate (cm^{-3})	Surface defect density (cm^{-2})
R146	Reg.	8	253.5/279.5/312/344.5 /383.5/435.5/500.5 /591.5	3100.5	3.8×10^{16}	3.2×10^{17}	1.6×10^{17}	5×10^{4}
Y001D	Reg.	3	312/344.5/383.5	1040	5.1×10^{16}	2.8×10^{17}	1.2×10^{16}	3×10^{4}
Y002D	Reg.	6	312/344.5/383.5/435.5 /507/604.5	2587	5.1×10^{16}	2.8×10^{17}	1.2×10^{16}	7×10^{4}
Y003D	Reg.	3	312/344.5/383.5	1040	5.1×10^{16}	2.8×10^{17}	1.2×10^{16}	3×10^{4}
Y004D	Rev.	3	312/344.5/383.5	1040	5.1×10^{16}	2.8×10^{17}	2.6×10^{16}	3×10^{4}
Y005D	Rev.	3	312/344.5/383.5	1040	5.1×10^{16}	5.1×10^{16}	2.6×10^{16}	2×10^{4}
Y007D	Rev.	1	1040		5.1×10^{16}	2.8×10^{17}	2.6×10^{16}	3×10^{4}
Y008D	Rev.	6	312/344.5/383.5/435.5 /507/604.5	2587	3.8×10^{16}	2.9×10^{17}	2.6×10^{16}	2×10^{4}
Y009D	Rev.	8	312×8	2496	3.8×10^{16}	2.9×10^{17}	2.6×10^{16}	5×10^{4}
Y010D	Rev.	3	507/617.5/793	1917.5	5.1×10^{16}	2.8×10^{17}	2.6×10^{16}	3×10^{4}
Y011D	Rev.	1	2340		5.1×10^{16}	2.8×10^{17}	2.6×10^{16}	5×10^{4}
Y012D	Rev.	1	3120		5.1×10^{16}	2.8×10^{17}	2.6×10^{16}	5×10^{4}
Y014D	Rev.	1	1040		5.1×10^{16}	2.8×10^{17}	1.6×10^{17}	6×10^{3}

Wafer R146 was grown with the regular illumination configuration in an Intevac Gen-II MBE system and the Y-series wafers were grown with the reverse illumination configuration in a Veeco GENxplor MBE system. In the regular illumination configuration, the electron barrier is near the top surface; while in the reverse configuration the hole barrier is near the top. Table 3.1 summarizes all ICIP wafers with various numbers of cascade stages (N_C) and illumination configurations (Config.). The carrier concentration in the substrate is 1.2×10^{16} cm^{-3} for wafers Y001D to Y003D, 2.6×10^{16} cm^{-3} for wafers Y004D to Y012D, and 1.6×10^{17} cm^{-3} for wafers R146 and Y014D. These ICIP structures generally have good structural quality as determined by x-ray diffraction. Wafer R146 had some tensile strain and the Y-series wafers generally had reduced strain after adjustment of design parameters and beam fluxes. The surface defect densities varied with growth run and MBE conditions as shown in Table 3.1.

The absorbers in these ICIPs were composed of 27Å-InAs/15Å-GaSb/8Å-Al(In)Sb/15Å-GaSb M-shape superlattices (SLs) [125] for a period of 65 Å. Thin Al(In)Sb layers were inserted into the InAs/GaSb SL to lower the sensitivity of the miniband energy to possible layer thickness fluctuations during MBE growth and to reduce the miniband width so that the absorption coefficient of the SL has a relatively sharp increase near the cutoff wavelength - a behavior approaching the two-dimensional (2D) electron density of states. All GaSb layers in the absorbers were *p*-type doped at 3.8-5.1×10^{16} cm^{-3} so that electrons were minority carriers, while the GaSb buffer layers were generally *p*-type doped at 2.8-2.9×10^{17} cm^{-3} except for Y005D which was doped at 5.1×10^{16} cm^{-3}. The bandgap of these absorbers was designed for a cutoff wavelength near 4.3 µm at 300 K, which is consistent with the observed values of 4.2-4.5 µm from devices made from these wafers. This agreement indicates good control of layer thickness and composition for all MBE growths. Except for wafer Y009D, where each absorber has the same thickness with an equal number of SL periods, the absorber thickness (*i.e.*, the number of SL periods) is increased in the optically deeper stages to achieve current matching.

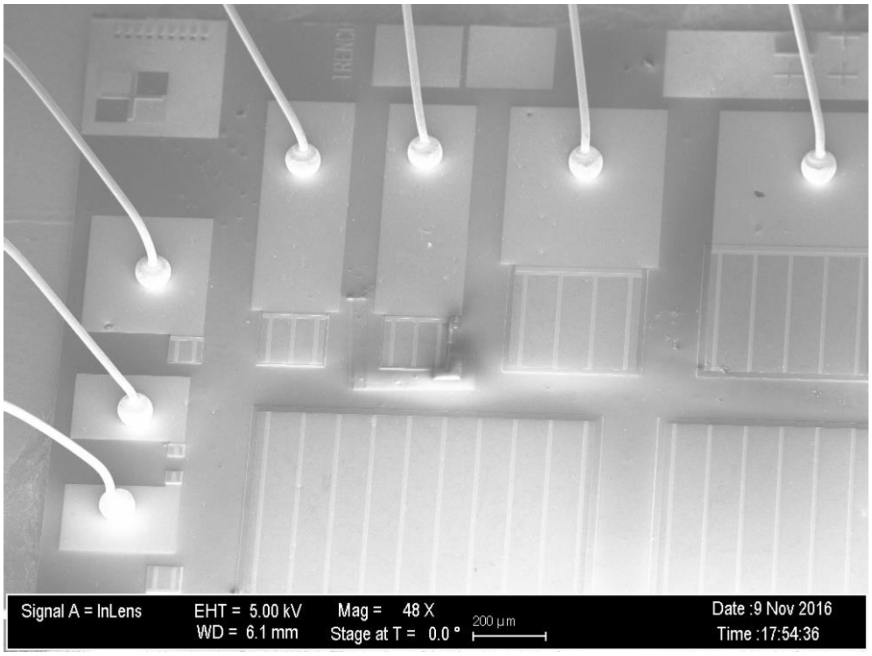

Figure 3.1: Micrograph of processed and wire-bonded detector samples taken using scanning electron microscopy.

After MBE growth, the wafers were processed into square mesa detectors with dimensions from 50 to 1000 μm using conventional contact UV photolithography and wet etching, as shown in Fig. 3.1. An RF-sputter deposited two-layer passivation scheme (Si_3N_4 then SiO_2, see Fig. 3.2) was used to reduce the overall stress and minimize pin holes. As can be seen from Fig. 3.3, The Si_3N_4+SiO_2 passivation has significantly higher median R_0A (order of magnitude) than that from only SiO_2 passivation at low temperatures, for temperatures higher than 200 K the median R_0A from two methods were similar. Sputter deposited Ti/Au layers provided the top and bottom contacts. Finally, the devices were mounted on heat sinks and wire bonded. For device characterization, light was incident on the top surface for all devices.

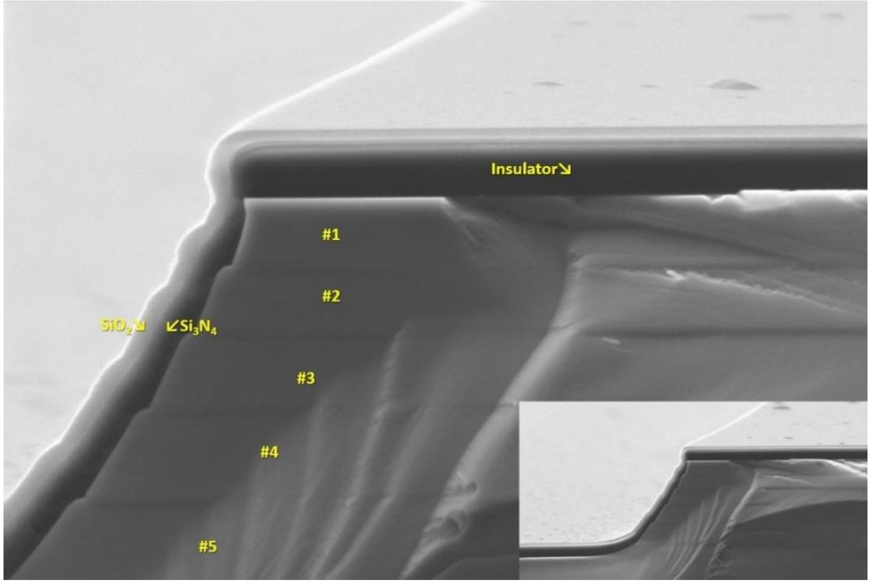

Figure 3.2: Cross section view of a five-stage ICIP under SEM.

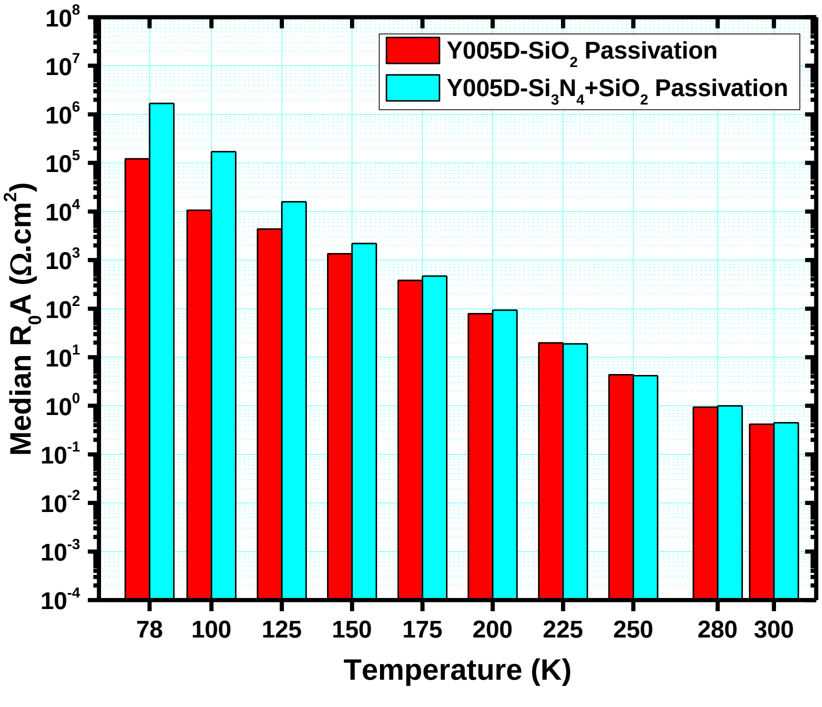

Figure 3.3: Median R_0A vs. temperature for two passivation with wafer Y005D.

3.3 Device Characterizations and Discussion

3.3.1 Eight-stage ICIP with regular illumination configuration

The eight-stage ICIPs (wafer R146) configured for regular illumination, were characterized first. The device dark current (I_d) was measured at temperatures from 78 to 333 K. The dark current density (J_d) *vs*. bias voltage (V) for a representative device at various temperatures is shown in Fig. 3.4. The carrier transport in devices made from this wafer was dominated by the diffusion current when the temperature approached room temperature. However, their current density-voltage characteristics were sensitive to device size as reflected by the inverse product of zero-bias resistance (R_0) and device area (A) as a function of their perimeter–to-area ratio (P/A), as shown in Fig. 3.5. The contribution of bulk and surface currents on R_0A can be separated by fitting the device's R_0A to the Eq. 1.14 [25]. The surface contribution to overall current at 300 K was 8.3% for 1 mm × 1 mm devices, and increased to 50% for 0.2 mm × 0.2 mm devices (the percentage was an average for different devices with the same size). This implies significant leakage current from the side walls, which is probably due to imperfect passivation.

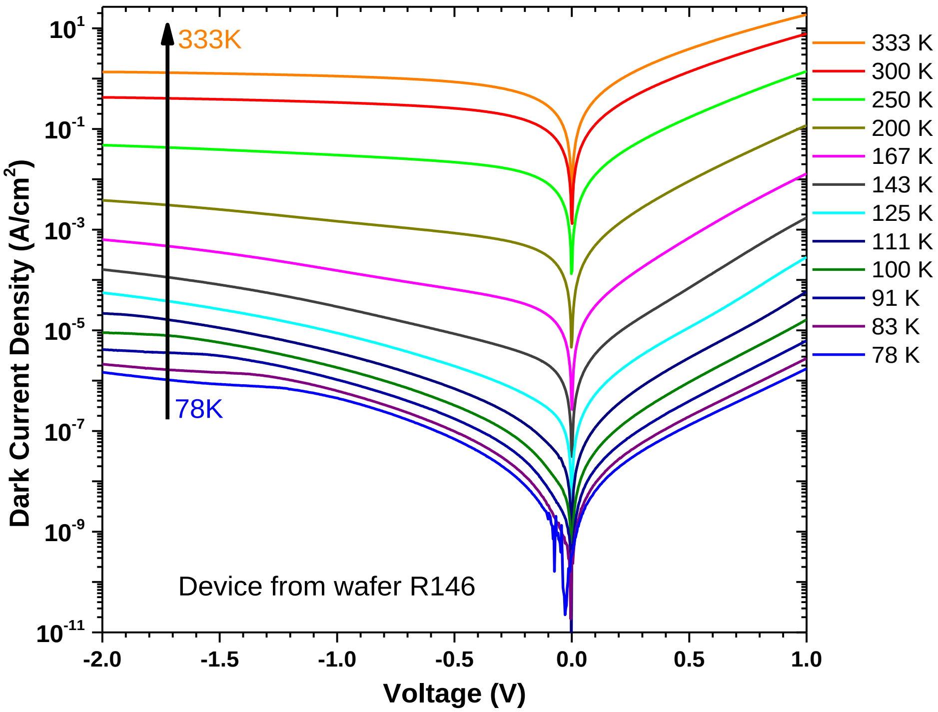

Figure 3.4: Dark current density *vs*. bias voltage from 78 to 333 K for a representative device of wafer R146.

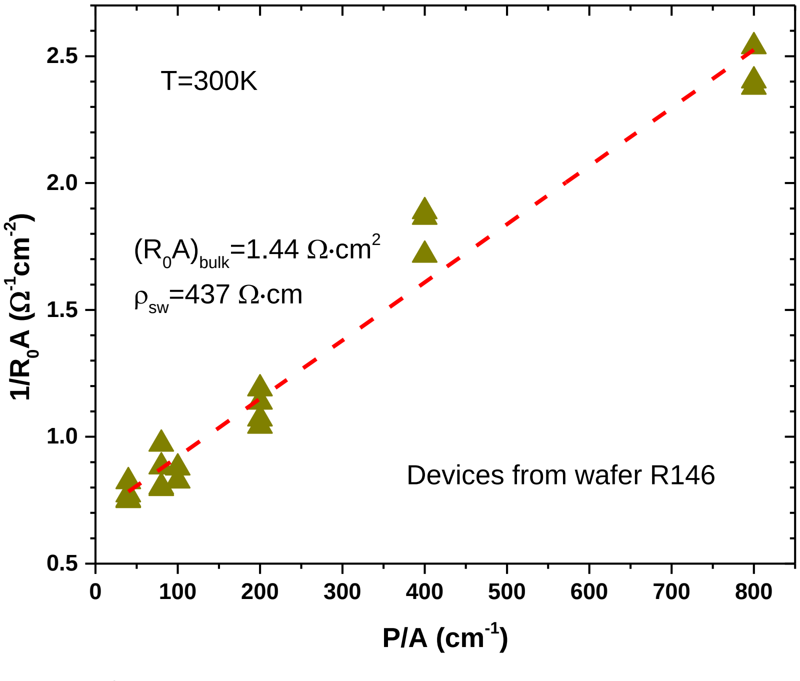

Figure 3.5: $(R_0A)^{-1}$ *vs*. *P/A* at 300 K for the devices fabricated from wafer R146.

The photo-response at various temperatures was measured using an FTIR spectrometer and calibrated with a blackbody source (aperture diameter of 1.52 cm) at 800 K with a 2π field of view (FOV). The device exhibited a smooth responsivity at zero-bias for all temperatures as shown in Fig. 3.6(a), and was insensitive to bias voltage as shown in Fig. 3.7. The 100% cutoff wavelength for this device was 3.7 µm at 78 K, and extended to 4.3 µm at 300 K. Dips near 3.1 µm in the response spectra were observed at low temperatures (78-167 K) and attributed to ice formation (from residual air in the cryostat) on the device surface at these low temperatures [126,127]. This dip has previously been observed in the spectra of T2SL detectors at low temperatures [63,128-131]. The relatively low responsivity was due to the thin absorbers in each stage. Compared to a conventional one-stage detector, the maximum responsivity and external quantum efficiency that can be achieved in an ICIP is reduced by the thin individual absorbers and multi-stage architecture. On the other hand, the thermal and shot noises are suppressed in ICIPs because the noise is proportional to the absorber thickness and inversely proportional to the square root of the number of cascade stages, N_C. Therefore, the device performance of the ICIPs is better indicated by detectivity, D^* (Eq. 2.1). In Eq. 2.1, the suppression of Johnson noise in a multi-stage ICIP implicitly follows from the large R_DA associated with the series connection of cascade stages with thin absorbers, as compared to a single, thick absorber in a conventional detector. The Johnson-noise-limited detectivity, D^* (for the representative device with size 0.2 ×0.2 mm^2), under zero-bias at different temperatures is shown in Fig. 3.6(b). At high temperatures, the total current density J is dominated by the dark current density, J_d. The value of ~10^9 cmHz$^{1/2}$/W at 300 K is lower than expected because R_0A was small due to significant surface leakage current. If the surface leakage current could be completely eliminated, the Johnson-noise-limited detectivity at 300 K would be ~20% higher (1.2×10^9 cmHz$^{1/2}$/W), as determined by inserting $(R_0A)_{\mathrm{Bulk}}$ into Eq. 1.14. At 300 K, the detectivity increases above 10^9 cmHz$^{1/2}$/W with reverse bias, because R_DA increases with reverse bias, while the shot noise increases more slowly, as illustrated in Fig. 3.7.

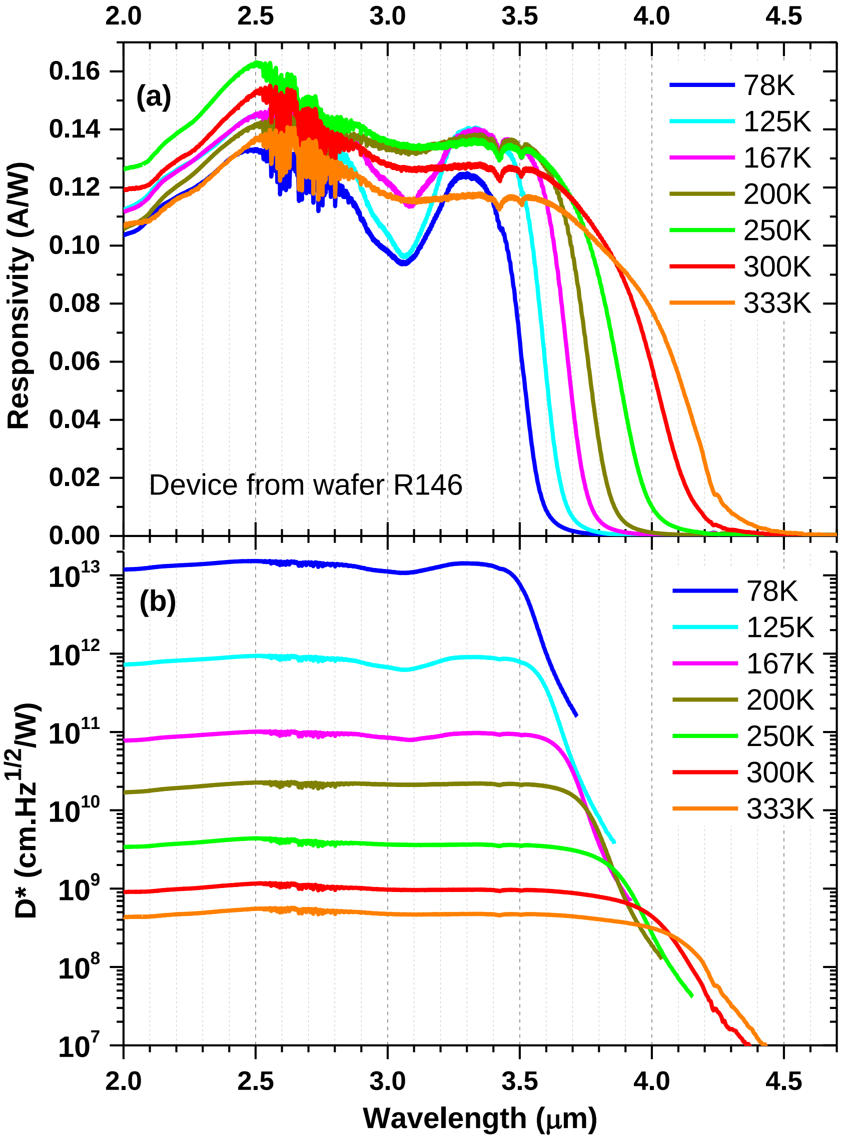

Figure 3.6: (a) Zero-bias responsivity and (b) Johnson-noise-limited D^* for a detector from wafer R146 at various temperatures.

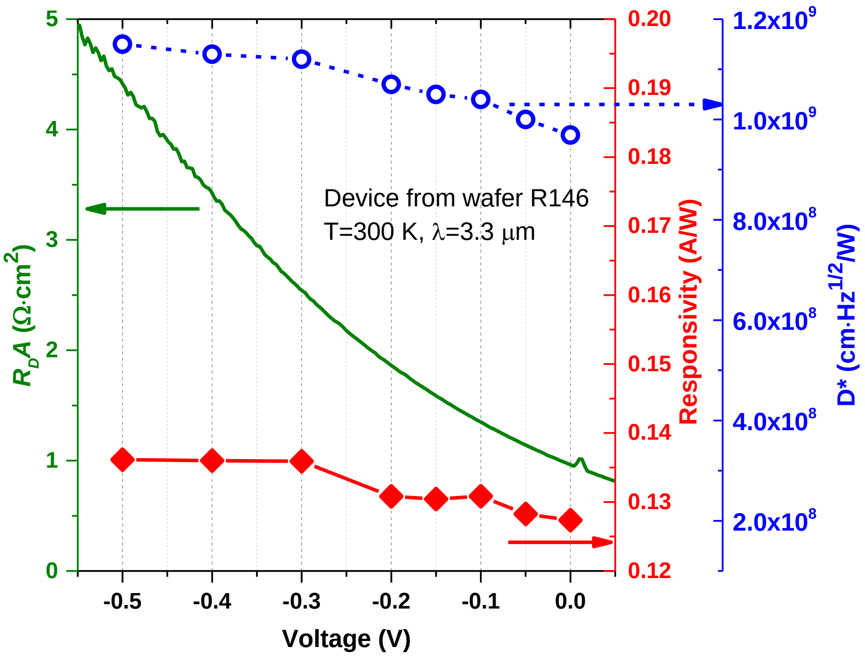

Figure 3.7: R_DA, responsivity, and D^* *vs.* bias voltage for a detector from wafer R146 at 300 K. The D^* was limited by Johnson noise under zero-bias, while both Johnson noise and shot noise were included under reverse bias.

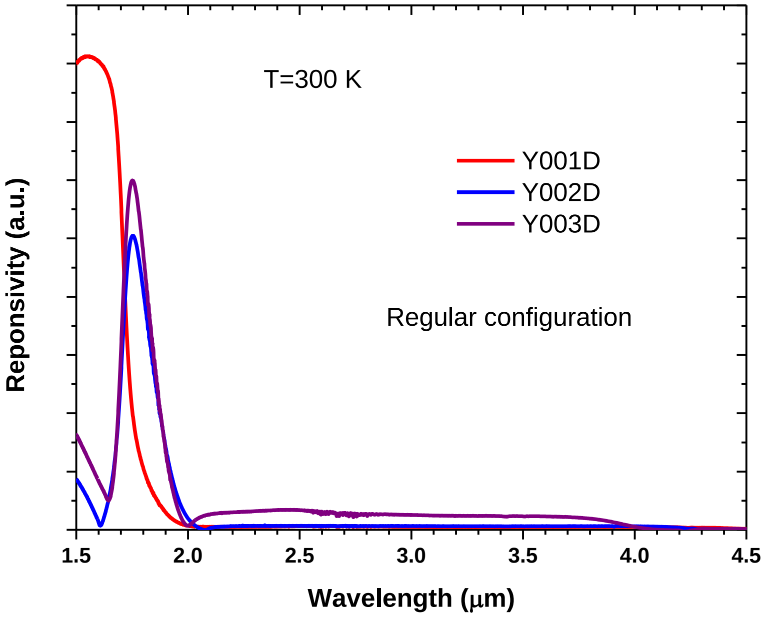

Figure 3.8: Response for devices from wafers Y001D, Y002D and Y003D under zero bias at 300 K.

The other three wafers Y001D, Y002D and Y003D are also in the regular illumination configuration with three-, six- and three-stage ICIP structures. However, their response curve exhibited an extremely strong GaSb response peak, as shown in Fig. 3.8. The reason for this behavior will be explained in the following section, and no further investigations are made for these wafers.

3.3.2 ICIPs with reverse illumination configuration

As indicated in Table 3.1, the ICIP structures for the Y-series wafers (except for Y001D, Y002D and Y003D) are in the reverse illumination configuration with varying absorber thickness and number of cascade stages. Devices with a bottom substrate contact were made from wafers Y004D, Y005D, Y007D, Y008D, Y009D Y010D, Y011D and Y012D. Some of them exhibited a significant response peak near the GaSb bandgap, as shown in Fig. 3.9, because the GaSb substrates had a nominal doping concentration of p_s =2.6×10^{16} cm^{-3}, while the buffer layers were generally doped at p_b=2.8×10^{17} cm^{-3}. Consequently, there is an electric field (similar to that in a *pn* junction) between the substrate and buffer layer that results in a small barrier ($\sim k_B T\cdot\ln(p_b/p_s)$=62 meV at 300 K) that affects carrier transport across this junction, as can be seen from the inset to Fig. 3.9. This junction facilitated the collection of photo-generated carriers with photons at energies near the GaSb bandgap, which was especially significant for devices made from wafers with the regular illumination configuration (Y001D, Y002D and Y003D). For devices with the reverse-illumination configuration, the photon-response peak near the GaSb bandgap, which was possibly caused by illumination through the etched trench, was substantially smaller. Nevertheless, its presence may affect the smooth transport and collection of photo-generated carriers initiated in the cascade region, resulting in a possible reduction of device responsivity. This can be seen by comparing devices with and without the photon-response peak near the GaSb bandgap, as shown in Figs. 3.9 and 3.10.

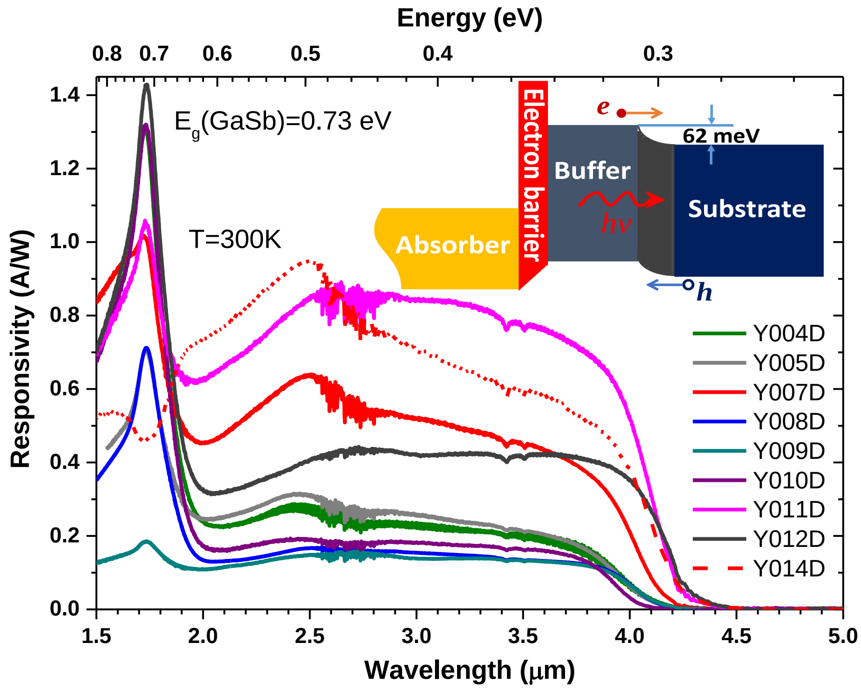

Figure 3.9: Responsivity of the device with a GaSb response peak near 0.72 eV from each wafer at 300 K. The inset shows the schematic band diagram between the buffer layer and the substrate for all wafers except R146 and Y014D.

To further examine this effect, an electrical contact to the buffer layer was used for devices grown on the low-doped substrates and wafer Y014D was grown with the same structure as Y007D, on a substrate with the higher nominal doping concentration (1.6×10^{17} cm^{-3}). When a contact to the buffer layer was used for devices, the response peak near the GaSb bandgap was either substantially reduced or completely removed, and there was no GaSb-response peak for any devices made from Y014D (see Fig. 3.9). To minimize the effect of this junction on the device characterization, only the devices with small or no GaSb-response peaks were selected from each of these wafers for the more extensive investigation reported below. Also, the series resistance for devices on substrates with different doping concentrations is expected to be different, which complicates the extraction of their intrinsic electrical properties. For example, the R_0A of devices from Y007D and Y014D at 300 K were 0.089 and 0.042 Ω·cm^2, respectively, while their responsivities were nearly equal, as shown in Figs. 3.10 and 3.11.

The zero-bias responsivity of the Y-series detectors at different temperatures is shown in Fig. 3.10, and their 100% cutoff wavelength is 4.2-4.6 μm at 300 K. Unlike the devices in Fig. 3.9 (except Y014D), none of the representative devices in Fig. 3.10 and Fig. 3.11 showed a GaSb response peak under zero-bias. The one-stage detectors showed higher responsivities than those of the multi-stage ICIPs, which is due to their thicker absorbers. The responsivities at 3.3 μm of the devices from Y007D, Y011D and Y012D at 300 K were 0.67 (0.74), 0.83 (1.33) and 0.74 (1.55) A/W under zero bias (100 mV bias), respectively. As can be seen from Fig. 3.11(a), the zero-bias responsivities of devices from Y012D and Y011D increased with temperature up to 200 K, due to bandgap narrowing; and then began to saturate and drop significantly for temperatures above 250 K, suggesting a reduction of the diffusion length below 2 μm above 250 K. At 300 K, the zero-bias responsivity of a device from wafer Y011D was somewhat higher than that from Y012D, indicating some variations of material quality as reflected by the longer cutoff wavelength in devices from Y012D. The zero-bias responsivity of a device from Y007D increased up to 250 K, and then began to saturate and decrease slightly above 280 K, suggesting that the diffusion length was about 1 μm at 250 K and became shorter at higher temperatures. This means that multi-stage ICIPs with relatively thin discrete absorbers should be appropriate to accommodate the shortening of the diffusion length at high temperatures.

Indeed, except for the three-stage ICIP from Y010D with a 793-nm-thick absorber in the last stage, the zero-bias responsivity of devices from all other multi-stage wafers did not decrease until about 300 K, as shown in Fig. 3.11(a). The zero-bias responsivity of the three-stage ICIP from Y010D was the highest (0.34 A/W at 3.3 µm at 250 K) among multi-stage ICIPs, but decreased with temperature above 250 K, suggesting that the diffusion length could be shorter than 0.8 µm at temperatures above 250 K and indicating possible material quality variation in comparison with Y007D. This decrease may also be the result of deviations from the current matching between stages in Y010D devices at high temperatures, which could be more substantial due to their relatively thick absorbers (507/617.5/793 nm) in every stage. For the devices with absorbers that are thicker than the diffusion length at high temperatures, their responsivities became bias dependent. For example, devices from Y007D and Y010D became relatively sensitive to bias voltage at 280 K, while devices from Y011D and Y012D started to show strong bias dependence from 250 K. The bias dependence of the responsivity for these devices at 300 K is shown in Fig. 3.11(b) and Fig. 3.7, from which one can see that the responsivity for the current-matched ICIPs from Y004D, Y008D and R146) with relatively thin absorbers was nearly insensitive (≤5%) to the bias voltage. This suggests that the diffusion length at 300 K is probably comparable to the thickness of the thickest absorber (~0.6 µm) in these devices. However, the responsivity of the one-stage device from Y014D was nearly insensitive to bias voltage. Considering possible variations and non-uniformity of material quality and device fabrication, the diffusion length for these detectors is estimated to be 0.6 to 1.0 μm at high temperatures (250-300 K).

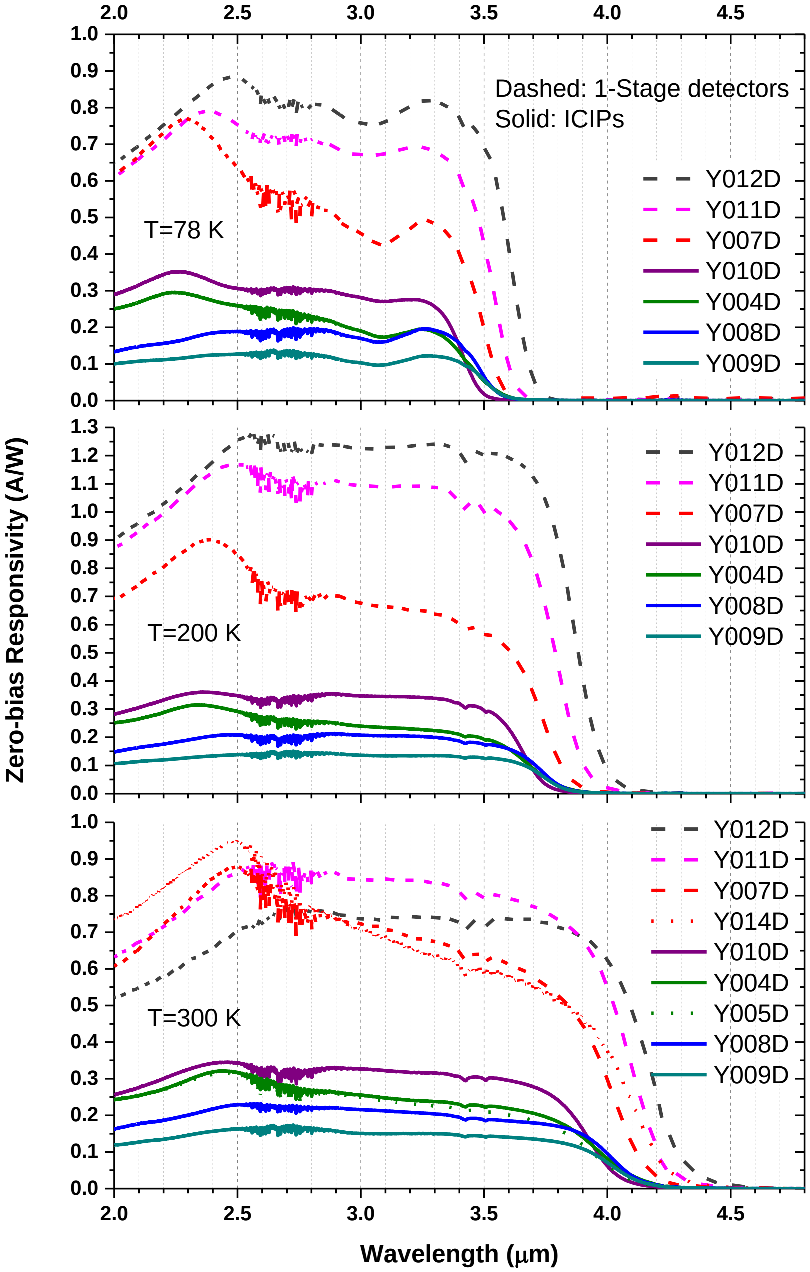

Figure 3.10: Zero-bias responsivity for detectors from the Y-series wafers at different temperatures.

For the multi-stage ICIPs, the device from R146 with a regular illumination configuration had a lower responsivity than the ICIPs with a reverse illuminating configuration. This occurred because the thinnest absorber (253.5 nm for the 1st stage) in R146 was thinner than in devices from the other wafers (≥312 nm for the 1st stage). Additionally, no electrical gain was present in devices with the regular illuminating configuration, while a gain exceeding unity was observed in devices with the reverse illuminating configuration, which will be discussed in section 2.3.

For devices made from wafers Y004D, Y005D, and Y008D, the absorber thickness (312 nm) in their first stage is the same, and their responsivities and temperature dependences were very similar. Wafers Y004D and Y005D were designed with the identical structure (although with different doping concentrations in their buffer layers) and their devices showed little difference in their responsivity. Similarly, their detectivities (see Table 3.2 and Fig. 3.12) are essentially the same, demonstrating excellent MBE growth repeatability for the same campaign period. Additional stages in Y008D compared with Y004D and Y005D (6 *vs*. 3) resulted in devices with slightly lower responsivity at high temperature, which was probably the result of a slight current mismatch between the optically deeper stages with relatively thick absorbers. Nevertheless, the additional stages in Y008D resulted in devices with a higher R_0A and D^* than observed in devices from Y004D and Y005D (see Table 3.2 and Fig. 3.12). The characteristics of devices at 300 K made from all the wafers are summarized in Table 3.2.

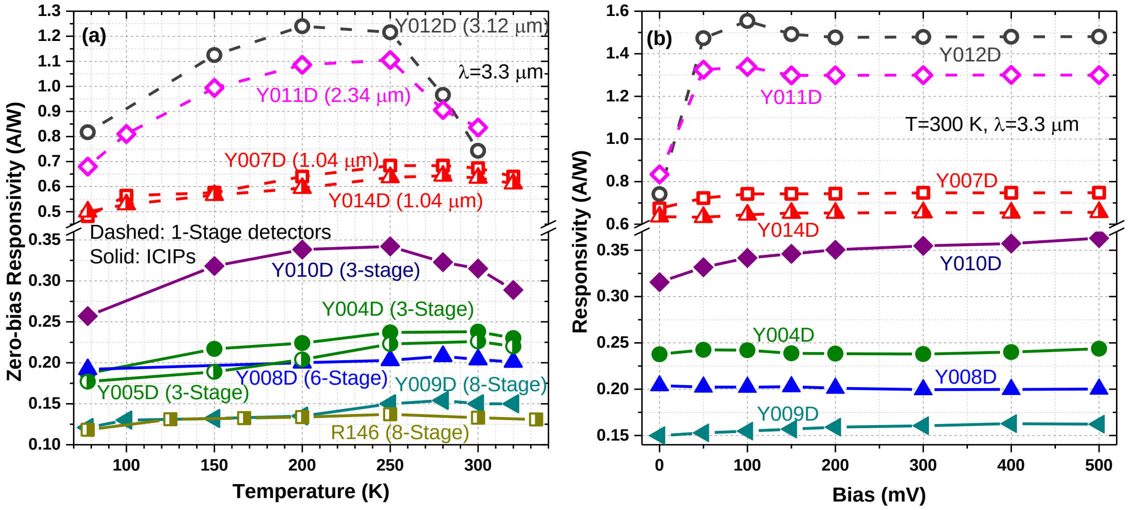

Figure 3.11: (a) Zero-bias responsivity at 3.3 μm *vs*. temperature and (b) Bias dependent responsivity at 300 K for all the detectors from all wafers. In the top portion of (a), the number in the parentheses indicates the absorber thickness for one-stage devices. Different vertical scales are used in the top and bottom portions to better show variations.

Table 3.2: Performance at a wavelength of 3.3 μm for ICIPs (background temperature=25 °C, FOV=2π) at 300 K.

Detector	R146	Y004D	Y005D	Y008D	Y009D	Y010D	Y007D	Y014D	Y011D	Y012D
# of stages	8	3	3	6	8	3	1	1	1	1
100% λ_c (μm)	4.3	4.3	4.3	4.3	4.3	4.2	4.3	4.4	4.4	4.5
Device dimension (mm)	0.20	0.40	0.40	0.50	0.20	0.40	0.20	0.10	0.20	0.20
Zero-bias D^* (cm·Hz$^{1/2}$/W)	9.7×10^8	1.3×10^9	1.1×10^9	1.5×10^9	1.1×10^9	1.6×10^9	1.6×10^9	1.0×10^9	1.3×10^9	1.0×10^9
R_λ (A/W)	0.13	0.24	0.21	0.20	0.15	0.31	0.67	0.64	0.84	0.71
R_0A (Ω·cm^2)	0.96	0.46	0.51	0.93	0.86	0.42	0.089	0.042	0.041	0.036
D^* under bias (cm·Hz$^{1/2}$/W)	1.2×10^9 (-500 mV)	1.5×10^9 (150 mV)	1.4×10^9 (150 mV)	1.8×10^9 (200 mV)	1.3×10^9 (400 mV)	1.8×10^9 (150 mV)	1.9×10^9 (150 mV)	1.2×10^9 (100 mV)	2.1×10^9 (100 mV)	2.0×10^9 (100 mV)
J_d (A/cm^2) under bias	0.26	0.17	0.15	0.17	0.26	0.23	0.45	0.87	1.13	1.52
R_λ (A/W) under bias	0.14	0.24	0.23	0.20	0.16	0.35	0.74	0.64	1.30	1.48
R_DA (Ω·cm^2)	4.41	2.03	2.67	2.98	2.97	1.17	2.16	0.48	0.35	0.18

Figure 3.12 shows the zero-bias detectivities of devices from each wafer. Although the one-stage detectors had significantly higher responsivities due to their thick absorbers, their zero-bias detectivities (1.0-1.6×10^9 cm·Hz$^{1/2}$/W) were comparable to, or somewhat lower than, those of the ICIPs. This is because the devices with thick absorbers had a substantially lower R_0A and higher Johnson noise. At a finite reverse bias, the responsivity increased substantially for the one-stage devices from Y011D and Y012D with thick absorbers (>2 µm), resulting in somewhat higher detectivity (2.0-2.1×10^9 cm·Hz$^{1/2}$/W). However, D^* is smaller in the device from Y012 with the thicker absorber (3.12 µm) than in the device from Y011D with a thinner absorber (2.34 µm). This is because the increase of responsivity is less than the increase of noise after the absorber reaches a certain thickness [132], especially when the diffusion length has a finite value [83], resulting in a reduced D^* with further increase of absorber thickness. This limitation can be, in principle, circumvented or significantly alleviated in ICIPs based on a discrete absorber architecture with total absorber thickness well beyond the diffusion length, resulting in an optimized D^* exceeding the maximum value that a single-stage detector can achieve [83]. Practically, this requires a sophisticated MBE system that can grow high-quality thick ICIP structures with stable fluxes over many hours (>10) and appropriate device fabrication with excellent passivation to minimize the surface leakage current that reduces R_0A because ICIPs trade signal for reduced noise. The ICIPs that were investigated in this work are far from optimal in terms of material quality, device fabrication, total absorber thickness and current matching. Nevertheless, they are already appropriate for uncooled, high-speed operation as demonstrated using an IC laser as an IR source [91].

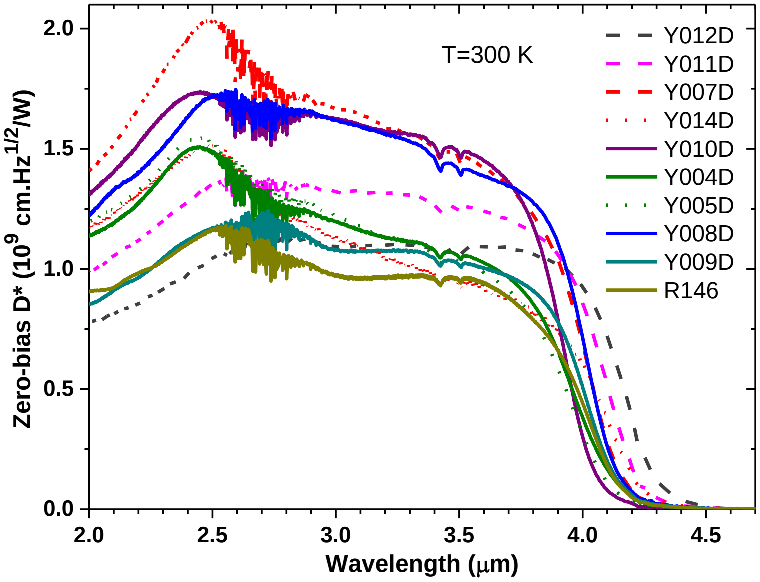

Figure 3.12: Johnson-noise-limited *D** for detectors from all wafers at 300 K.

From the experimental results discussed above on ICIPs with individual absorber thicknesses that are varied for current matching between cascade stages, it is evident that the responsivity depends on how well the current is matched. To further investigate this dependence, ICIPs were made from wafer Y009D which was designed with identical absorbers in each of its 8 stages. For a good comparison, the absorber thickness (312 nm) in Y009D was made equal to that of the first stage of ICIPs from wafers Y004D, Y005D and Y008D and the doping concentration in the absorber was kept the same (3.8×10^{16} cm^{-3}). The responsivity of the device from Y009D (*e.g.*, 0.15 A/W at 300 K) was substantially lower than the value achieved in devices from the other three wafers (*e.g.*, ≥0.20 A/W at 300 K) at all temperatures, as shown in Fig. 3.11(a). This is attributed to significant mismatch of photocurrent between cascade stages with nominally equal absorbers in Y009D because the light intensity was substantially attenuated in optically deeper stages after partial absorption in preceding stages. This result contradicts the findings reported in Ref. [87]. In those experiments, the responsivity of five-stage MW ICIPs with identical absorbers was approximately linearly proportional to the individual absorber thickness, without being affected by the light intensity attenuation along the propagation direction even though the total absorber thickness exceeded 2 μm. This behavior cannot be explained and understood by existing theories [14,83], but might be related to the electrical gain that will be discussed in section 2.3. Another puzzle in Ref. [87] is that the measured R_0A increased as the absorber became thicker with diffusion limited transport at high temperatures (*e.g.*, 300 K), which is opposite to what theories projected [83,99,133], but might be related to imperfect device fabrication as discussed below.

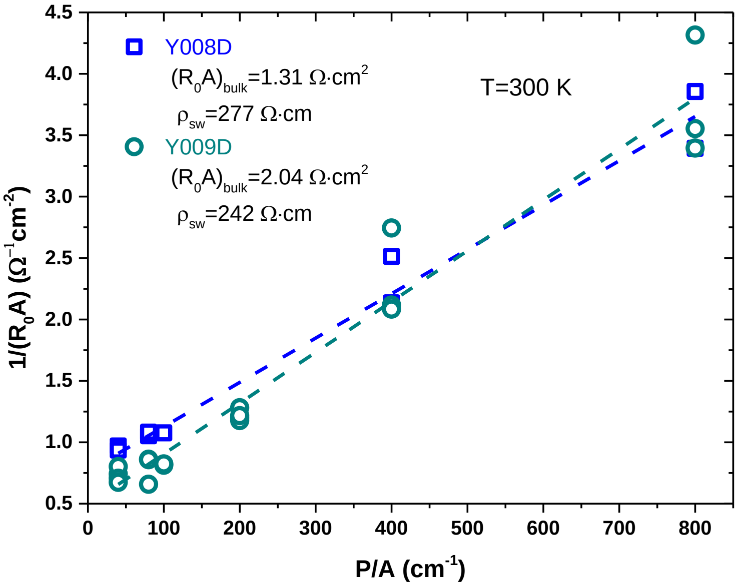

Figure 3.13: Size dependence of R_0A for the six- and eight-stage devices from wafers Y008D and Y009D at 300 K.

The device fabricated from Y009D with identical absorbers also showed a smaller R_0A (0.86 Ω·cm^2 at 300K) than the device from Y008D (0.93 Ω·cm^2 at 300K), which contradicts the predictions of a diffusion transport model [83]. In order to examine whether this was related to the surface leakage current, $(R_0A)_{\text{Bulk}}$ was extracted by fitting the device R_0A to Eq. 1.17. Figure 3.13 shows the size dependence of R_0A for the devices from Y008D and Y009D at 300 K. The extracted $(R_0A)_{\mathrm{Bulk}}$ for Y009D was substantially larger than for Y008D, which is consistent with the theoretically expected dependence on absorber thicknesses and number of stages [83], while the side-wall resistivities were comparable since the devices were fabricated at the same time.

3.4 Absorption coefficient and electrical gain

The absorption coefficient was around 3100 cm^{-1} at 3.3 µm based on transmission measurements from the three one-stage wafers, as shown in Fig. 3.14. This value is in good agreement with the values reported for T2SLs [134-136] and close to the value that was used to design the current matched ICIPs (3000 cm^{-1}). Since the photocurrent generated in each stage is equal in the current matched ICIPs, the quantum efficiency of each stage should be equal as well and can be expressed as

$$\eta/(1-R)=(1-e^{-\alpha d_1})=e^{-\alpha d_1}(1-e^{-\alpha d_2})=\cdots=e^{-\alpha(d_1+d_2+\cdots d_{N-1})}(1-e^{-\alpha d_N}), \qquad (3.1)$$

where: η is the quantum efficiency, α is the absorption coefficient, R is the reflectance at the device's top surface, and d_N is the absorber thickness for stage N. For the ICIPs with equal absorber thickness (d) in each stage, the photocurrents generated in the different stages are not equal. The photocurrent generated in the last stage is the smallest among the cascade stages due to the light intensity attenuation in the absorbers, and consequently the quantum efficient is limited by the photocurrent in the last stage according to

$$\eta=(1-R)e^{-\alpha(N-1)d}(1-e^{-\alpha d}), \qquad (3.2)$$

If the electrical gain, *G*, in the detectors is not unity, the responsivity can be described as [61]:

$$R_\lambda = G\eta \frac{\lambda}{hc} = G(1-R)(1-e^{-\alpha d_1})\frac{\lambda}{hc}, \tag{3.3}$$

where λ, *h*, and *c* are the wavelength, Planck constant and speed of light, respectively.

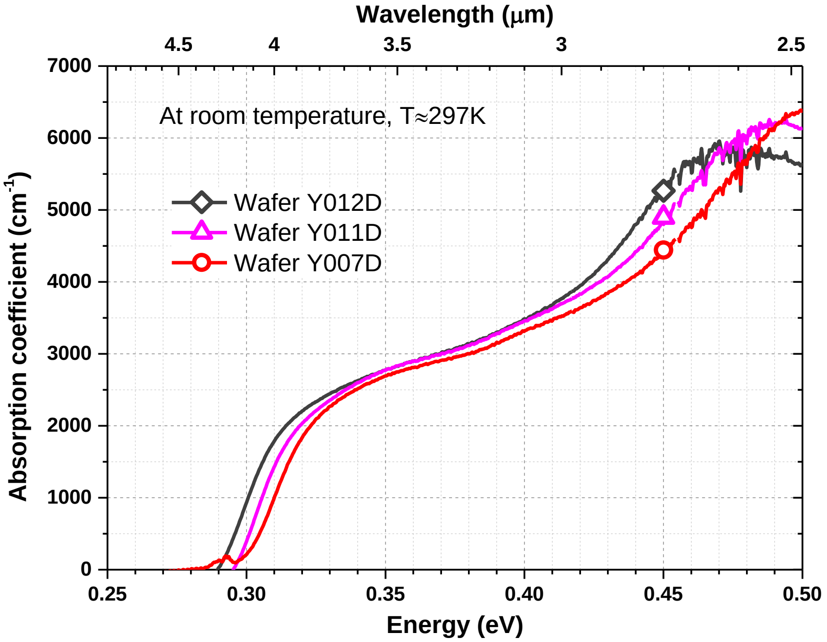

Figure 3.14: Absorption coefficient extracted from transmission measurements based on the one-stage wafers Y007D, Y011D and Y012D.

According to Eqs. 2.1-2.3, the electrical gain can be extracted from experimentally measured absorption coefficients and responsivities for all devices. In the calculation of the quantum efficiency, only the first stage was considered with Eq. 3.1 for the current matched ICIPs and only the last stage was considered with Eq. 3.2 for ICIPs with identical absorbers. The extracted electrical gain at 3.3 μm is shown in Fig. 3.15 for representative devices at 300 K from all wafers (except Y005D which is similar to Y004D). With the reverse illumination configuration, the electrical gain at 300 K was between 1.2 and 1.6 under saturated bias for current-matched ICIPs and one-stage detectors, and nearly reached 2 for the eight-stage noncurrent-matched ICIP. Gain exceeding unity was also observed in T2SL detectors (>5) [61] and in our previous type-I GaInAsSb detectors [95]. However, the electrical gain in devices from R146 with a regular illumination configuration was close to unity.

There are two possible mechanisms for producing an electrical gain above unity. One mechanism, implied in Ref. [83], arises from the distribution of bias voltage or electrical potential across individual cascade stages during device operation. For a multi-stage ICIP under illumination at zero-bias, the electrical potential across each individual stage will self-adjust to achieve equal current through each stage. If the number of photo-generated carriers is not equal in every stage, the electrical potential across each stage would also not be equal. The requirement of current continuity forces the stage with the largest amount of photo-generated carriers (typically the first stage in a non-current-matched ICIP with identical absorbers) to be slightly forward biased such that a forward injection current will partially offset the photocurrent. Hence, the responsivity in a non-current-matched ICIP is smaller than that in a current-matched ICIP, as observed in this work. Consequently, other stages with smaller amounts of photo-generated carriers will necessarily be under reverse bias to make the total voltage across all stages zero. The reverse bias will add a thermal generation current in those stages along the same direction as the photocurrent, resulting in an effective increase of the photo-current. When the thermal generation current is higher than or comparable to the photo-current (which is possible at high temperatures), the stages under a reverse-bias voltage could have a significant electrical gain as observed in the non-current-matched ICIPs from wafer Y009D, and also recently observed in long wavelength non-current-matched ICIPs [94]. Of course, this mechanism cannot explain the gain observed in one-stage devices, which leads us to now discuss the second possible mechanism.

According to the theory of photoconductors [31], the photoconductive gain is determined by the ratio of the carrier lifetime (τ) to the transit time (τ_t), which can be larger than 1. The ICIPs with short absorbers can be viewed as photoconductors, especially under a bias, in which the carrier transit time might be substantially shorter than the carrier lifetime, resulting in an electrical gain exceeding unity. This argument seems to be supported by the largest gain observed from non-current matched ICIPs from Y009D where all absorbers are kept thin (312 nm). However, this argument is not completely supported by somewhat randomly distributed values of *G* for ICIPs and one-stage devices with various absorber thicknesses (see Fig. 3.15). Such a high electrical gain was not observed from our previous ICIPs [14,15] (and R146) with the regular illumination configuration on GaSb substrates with a relatively high p-type doping concentration. To exclude the possible effect of the substrate that caused the extra GaSb response peak discussed earlier, a one-stage detector, Y014D, with the same structure as Y007D was grown on a GaSb substrate with a *p*-type doping concentration similar to that in R146. An electrical gain of 1.3 was observed in the detector from Y014D, although its value was smaller than that for Y007D (1.5) (see Fig. 3.15). At this moment, we do not fully understand what is responsible for these electrical gains. Further effort is required to investigate this phenomenon.

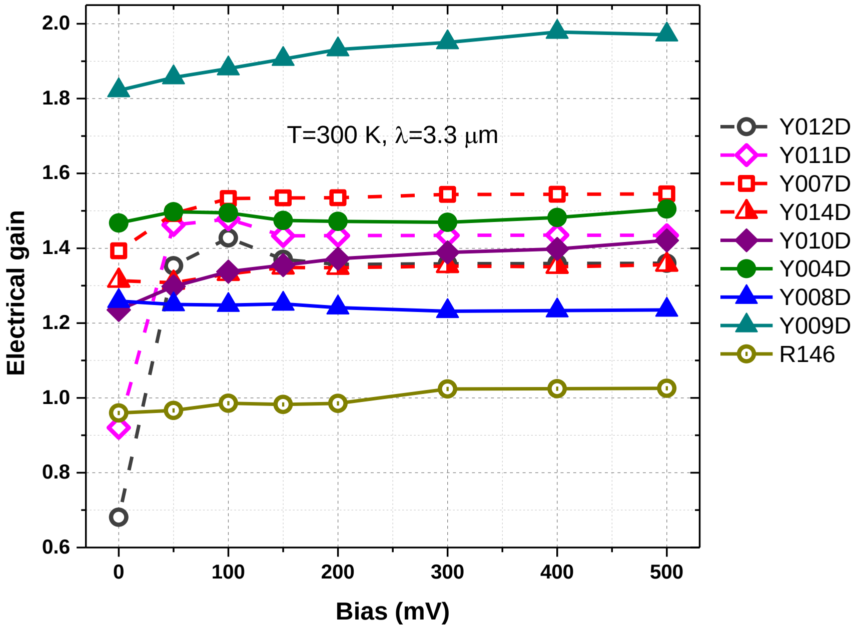

Figure 3.15: Extracted electrical gain at 3.3 μm for the devices from all wafers at 300 K.

3.5 Summary and concluding Remarks

In summary, MWIR one-stage detectors and ICIPs were studied with different absorber thicknesses, numbers of stages, and illumination configurations, as well as variations in substrate and buffer layer doping concentration. The multi-stage ICIPs were capable of operating at higher temperatures at zero-bias with superior carrier transport over the conventional one-stage detectors. Values of Johnson-noise-limited detectivity D^* exceeding 10^9 cm·Hz$^{1/2}$/W were obtained at 300 K. Based on the temperature dependence and the bias sensitivity of their responsivities with various absorber thicknesses, the diffusion length is estimated to be between 0.6 to 1.0 μm for T2SL materials at high temperatures (>250 K). By comparing responsivities between current matched ICIPs with various absorber thicknesses and noncurrent-matched ICIPs with equal absorbers, it was shown that the current-matching between cascade stages is important and necessary to achieve the maximum responsivity. In addition, electrical gain exceeding unity was demonstrated in these detectors in the reverse illumination configuration. This study illustrates the flexibility and potential advantages for ICIPs to achieve significantly improved device performance with advanced growth technology and better device fabrication. Currently, the understanding and device performance of ICIPs are still in a relatively early phase. With the wider availability of room temperature quantum cascade lasers [72,137,138] and advanced IC lasers [78,84,139,140], it is expected that the demands for room-temperature high performance MWIR detectors will grow, which will push for further understanding and development of ICIPs. Recently, the high-frequency operation of a mid-infrared interband cascade system that consists of a type-I interband cascade laser and an uncooled ICIP is demonstrated at room temperature [91] with a 3-dB bandwidth for an uncooled ICIP of 1.3 GHz. This initial study indicates the great potential of ICIPs for high-speed applications and the feasibility of compact systems for relevant applications.

Chapter 4 Mid-wave interband cascade infrared photodetectors based on GaInAsSb absorbers

4.1 Background and motivation

Interband cascade structures have been explored for constructing multi-stage IR photodetectors with the advantage of circumventing the finite diffusion length limitation in narrow bandgap photodetectors [14], leading to improved high-temperature and high-speed operation [14,15,62,65,88]. By using InAs/GaSb T2SL as the absorbers, ICIPs have been demonstrated over a wide wavelength range from SW to VLW (2.9 to 16 μm) [14,15,62-65,88]. InAs/GaSb T2SL absorbers have certain advantages, such as low tunneling current (with a relatively large effective mass insensitive to the SL bandgap) and the suppression of Auger recombination [8]. However, the drawback of T2SL detectors is their relatively small absorption coefficient. This issue can be alleviated by using bulk semiconductor materials such as GaInAsSb as the absorbers. In contrast to T2SL where electrons and holes are mainly located in different layers, GaInAsSb absorber allows even distribution of electrons and holes in the same layer and interfaces are eliminated. Consequently, high optical absorption coefficient and responsivity can be achieved with relatively thin GaInAsSb absorbers, which is desirable to obtain fast response without compromising signal strength. Additionally, the use of GaInAsSb absorbers, instead of T2SL absorbers with many interfaces, drastically reduces shutter movements during their MBE growth, which should make the mechanical parts of MBE last significantly longer without maintenance. The bandgap of $Ga_{1-x}In_xAs_ySb_{1-y}$ can be tailored by changing the composition to cover from

0.25 to 0.73 eV, while keeping it lattice matched to GaSb [141]. Although the growth of quaternary GaInAsSb alloys is challenging, especially in immiscibility regions [142,143], they have been used in infrared optoelectronic devices such as lasers [144,145], thermophotovoltaics [110,111], and infrared photodetectors [146-148]. Nevertheless, to the best of my knowledge, GaInAsSb detectors have not been reported in MWIR wavelength region beyond 3 µm even though the growth of thick GaInAsSb layer had been demonstrated on GaSb substrates with substantial strain and improved material quality [145,149,150]. Also, until this work, there has not been any study reported with bulk GaInAsSb material in ICIPs.

In this chapter, the initial investigation of ICIPs with quaternary GaInAsSb absorbers is discussed with a cutoff wavelength beyond 4 µm at 300 K. High absorption coefficients (compared to T2SL at similar wavelength) and gain have been observed from these initial GaInAsSb ICIPs, suggesting a possible improved frequency response for high speed application with the larger photocurrent (signal) caused by the enhanced absorption.

4.2 Device structures and material growth

Two detector structures were designed with quaternary $Ga_{0.44}In_{0.56}As_{0.5}Sb_{0.5}$ absorbers, which are lattice matched to the GaSb substrate and with a bandgap of about 0.29 eV at 300 K [141], corresponding to a cutoff wavelength of 4.3 µm. One structure is three-stage ICIP (ICIP-3) that has three cascade stages with thicknesses of individual absorbers designed as 260, 365 and 575 nm, respectively, as shown in Fig. 4.1. Thicker absorbers in the optically deeper stages are to ensure the photocurrent matching. The other one is one-stage detector (ICIP-1), in which the absorber thickness is 1,200 nm, equal to the total absorber thickness of ICIP-3. The *p*-type absorbers (p=2.8×10^{16} cm^{-3}) were sandwiched between the electron and hole barrier in each stage, as shown in Fig. 4.1. The hole barrier is composed of digitally graded three InAs/Al(In)Sb QWs with well layer thickness of 83, 72, and 65 Å, respectively. The electron barrier is composed of digitally graded seven GaSb/AlSb QWs with well layer thickness of 10, 12, 15, 19, 25, 36 and 53 Å, respectively, which is significantly thicker than the electron barrier with fewer GaSb/AlSb QWs in our previous ICIPs [14,15] and should be sufficient to force electrons move towards the preferred direction.

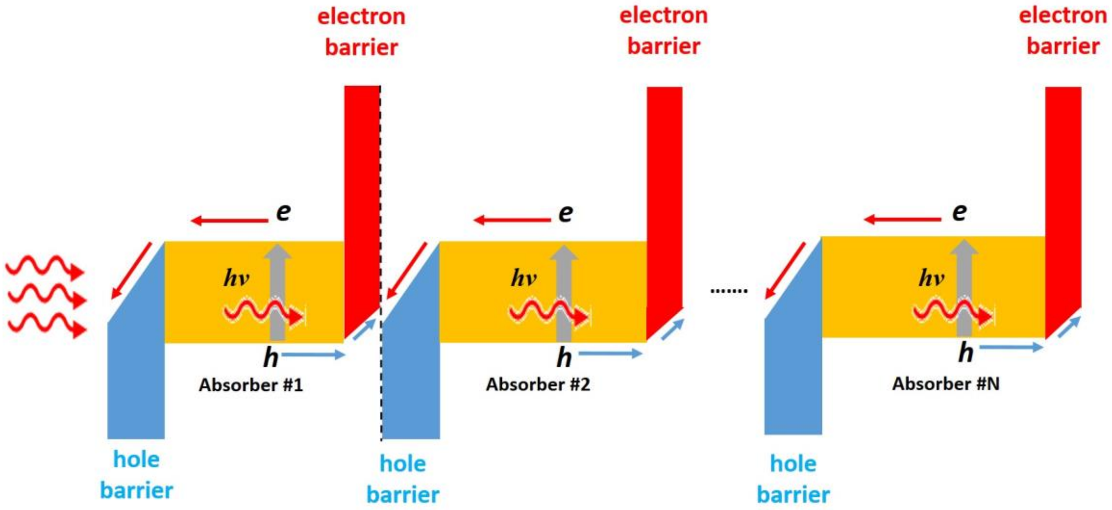

Figure 4.1: Schematic energy band profile of a three-stage ICIP with reverse illumination configuration. Variation of the absorber thickness is designed to achieve photocurrent matching between stages.

The ICIP structures were grown on nominally undoped *p*-type GaSb substrates at IQE Inc. in an Oxford-VG V-100 solid source MBE tool using a production epitaxial growth process developed specifically for Sb-based materials. Group V (As, Sb) fluxes were controlled by valved cracker cells, while the group III molecular beams (In, Ga, Al) were produced via SUMO or conical effusion cells. Substrate growth temperatures for the bulk absorber and barrier QW sections ranged from 400 to 500 °C, depending on the layer alloys and position within the structure. Additional details of the MBE configuration and *in situ* control tools have been previously described [151,152]. The undoped GaSb substrates were (100) with a miscut orientation of <0.5° and an epi-ready surface. Both ICIP structures are in the reverse illumination configuration [65], in which the hole barrier is close to the top surface and the light is incident on this top surface (Fig. 4.1).

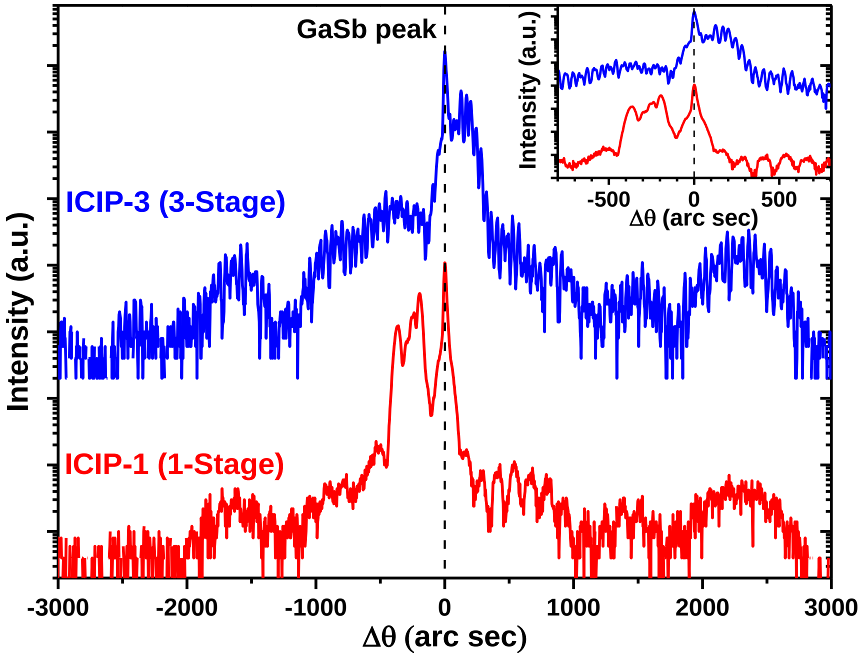

Figure 4.2: High resolution x-ray diffraction measurements for one-stage (blue) and for three-stage (red) wafers.

The crystalline quality of the ICIP wafers was investigated using high resolution x-ray diffraction (HRXRD), as shown in Fig. 4.2. The full width at half maximum (FWHM) of the measured main peak are 38 and 21 arc seconds for one- and three-stage wafers, respectively, indicating very good structural quality for both wafers, with the three-stage wafer being somewhat better. The one-stage wafer had a small compressive strain (810 ppm), while the three-stage wafer had a small tensile strain (-520 ppm). From the inset HRXRD, multiple adjacent peaks beside substrate peak may indicate somewhat different compositions of the GaInAsSb alloys caused by small deviations from the targeted alloy composition during the MBE growth. Both wafers had surface defect densities lower than 1×10^3 cm^{-2} under optical microscope with defect size in the range of 1.3 to 50 μm^2. After the growth, the device fabrication process followed the process flow described in section 3.2.

4.3 Results and discussion

4.3.1 Electrical characteristics

The electrical characteristics of detectors from both wafers were examined over a wide range of temperatures (78 to 340 K). The dark current densities J_d of three-stage ICIPs are lower than the one-stage devices for each temperature from 78 K to 340 K, as shown in the Fig. 4.3(a). This agrees with theoretical projections for thin individual absorbers and multiple stages [83]. Dark current densities in these GaInAsSb ICIPs are generally higher than those observed in our T2SL ICIPs with similar cutoff wavelength. For example, the dark current densities are 2.3×10^{-4} and 2.0×10^{-5} A/cm^2 for one- and three-stage ICIPs at 50 mV reverse bias at 78 K, respectively. One possible reason for this behavior is the small effective mass that might cause excessive leakage current (similar problems are observed in MCT detectors) [153]. Another factor for high dark current density is a possible additional leakage channel with a relatively low shunt resistance. This is evident at a low bias region (<100 mV) and reverse bias at low temperatures (<200 K) [154], where the effective resistances of the detectors are large so that the impact of the shunt resistance in parallel is more significant. Under a high forward bias or at high temperatures (>200 K), other current components such as the diffusion current and recombination current exponentially increase and become more dominant than the shunt current via the leakage channel. The extracted product of dynamic resistance (R_D) and device area (A) is plotted in Fig. 4.3(b), which shows R_DA peaked at a reverse bias for high temperatures. This suggests that the carrier transport at high temperatures is more diffusion-dominant at low reverse bias. The shunt resistance plays a more dominant role at low temperatures and limits the value of R_0A (R_DA at zero bias voltage). For example, the value of R_0A for all devices was less than 4,000 $\Omega \cdot \text{cm}^2$ at 78 K. Hence, the Johnson noise limited detectivities are relatively small at low temperatures. At higher temperatures (above 200 K), dark currents converge at a high forward bias, with a constant series resistance (~5 Ω) indicating a good ohmic contact, as shown in Fig. 4.3(b). This series resistance is significantly smaller than that for this device at 300 K (>100 Ω). This series resistance may have some effect on accurate determination of certain properties (*i.e.* responsivity and Johnson-noise limited detectivity) for large size devices (R_0<10 Ω) at the higher temperature (>300 K). Hence, the value of this series resistance was subtracted in the value of R_0A for devices in Fig. 4.4.

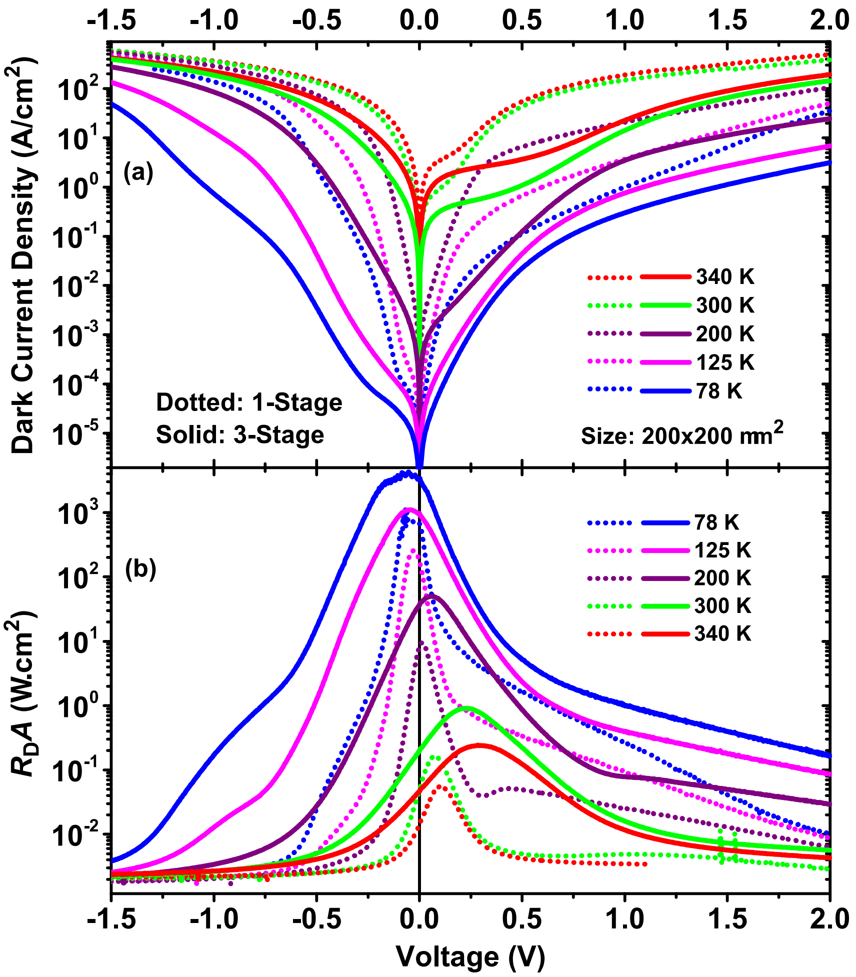

Figure 4.3: (a) Dark current densities (b) dynamic resistance-area products as a function of bias voltage from low to high temperatures for one- and three-stage detectors. The positive voltage denotes the reverse bias, as the detectors have the reverse configuration.

Generally, because of shorter individual absorbers and multiple stages, the value of R_0A is significantly higher in three-stage ICIPs than in one-stage detectors at every temperature. Also, their R_0A values are less sensitive to the device size for three-stage devices, as shown in Fig. 4.4, where R_0A is plotted as the perimeter to area ratio (P/A) at high temperatures (see Fig. 4.4(b)). From 200 K up to 340 K, R_0A was nearly independent on the device size for three-stage ICIPs; and its size dependence was also weak for one-stage devices. These observations suggest that the leakage current might be from bulk defects. This is reflected by small activation energies that were extracted from devices, as show in Fig. 4.4(a). The activation energy was obtained by an Arrhenius plot of device R_0A over the temperature range with the Eq. 1.13. As show in Fig. 4.4(a), a small activation energy of 30 meV is extracted from devices at low temperatures, which is indicative of surface leakage or defect-assisted tunneling currents. In the high temperature range (200-340 K), the extracted activation energies are 280 meV for three-stage and 260 meV for one-stage detectors. These values fall between the device bandgap (E_g=370 meV at 78 K) and the half-bandgap value. This suggests the existence of the Shockley-Read-Hall (SRH) recombination centers which, even though localized in the bulk materials, become dominant paths for tunneling and recombination current under certain conditions [155,156], and contribute significantly to leakage current over the entire temperature range.

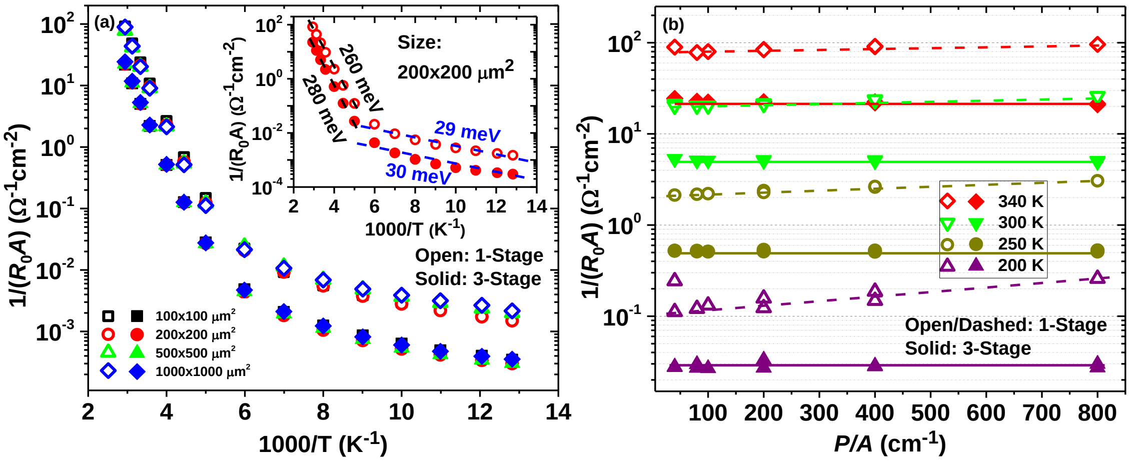

Figure 4.4: (a) Arrhenius plot for one- and three-stage devices with different sizes. Inset: activation energy extracted from selected devices. (b) $(R_0A)^{-1}$ *vs*. *P*/*A* for one- and three-stage devices at different temperatures. The values at 300 and 340 K had been subtracted by corresponding series resistance.

4.3.2 Optical characteristics

The photo-response spectra of devices at various temperatures were measured using a FTIR spectrometer and calibrated with an 800 K blackbody source (aperture diameter 1.52 cm). The cutoff wavelength is 3.7 (3.6) µm at 78 K and extends to 4.6 (4.5) µm at 300 K for the one-stage (three-stage) detectors. Figure 4.5(a) displays the responsivity for both one- and three-stage detectors (at 50 mV) in a temperature range from 78 to 340 K. The responsivity in both detectors is bias dependent at all temperatures, which might be caused by an undesirable barrier [60,65,88,157] in the carrier transport path. For a clear illustration, the responsivity at a wavelength (λ) of 3.3 µm is shown in Fig. 4.5(b) for devices at 0 and 50 mV, and the bias dependence is shown in Fig. 4.5(c) for both one-stage and three-stage devices at various temperatures. At low temperatures (78 to 125 K), devices from both wafers reached the maximum response at a reverse bias voltage of 50 mV. However, the responsivity for three-stage ICIPs is less sensitive to bias voltage, and is nearly unchanged with the bias voltage at high temperatures (>250 K), where the thermal energy could be sufficient to assist carriers to overcome the unintended barrier. In contrast, one-stage devices have strong responsivity dependence on bias over the entire range of temperatures and requires higher reverse bias to reach the maximum as the temperature increases (Fig. 4.5(c)). For instance, at 300 K, the responsivity at 3.3 µm for the one-stage device increases from 0.68 A/W at zero-bias to the maximum of 0.92 A/W near 150 mV (an increase of 35%). These large variations and the requirement of the higher bias voltage to reach peak responsivity for the one-stage device at high temperatures can be explained by the reduction of carrier diffusion length shorter than the absorber thickness (1.2 µm).

Because of thinner individual absorbers (<0.6 μm) in the three-stage devices, efficient collection of photo-generated carriers is maintained over the whole operating temperature range. This is supported by the continuous increase of responsivity with the temperature for the three-stage devices, as shown in Fig. 4.5(b) and (c). To be mentioned here, with the narrowing of the bandgap, the responsivity of the one-stage device at a reverse bias also increased when temperature was raised from 78 to 300 K, but at a slower percentage change, and then reduces from 300 to 340 K. These results demonstrate that multiple stage ICIPs with thin absorbers have superior carrier transport over a one-stage device.

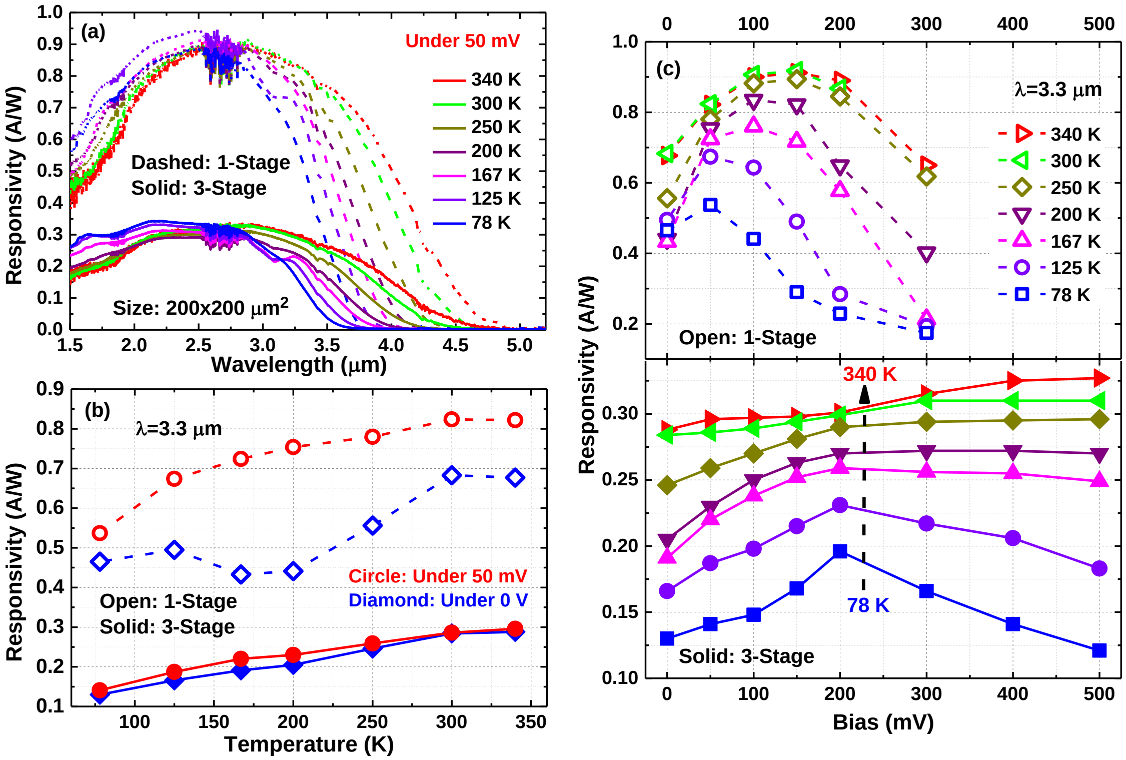

Figure 4.5: (a) Responsivity under 50 mV (b) Temperature dependence of responsivity at 3.3 μm for 1- and 3-stage ICIPs under 0 and 50 mV bias. (c) bias dependence at various temperatures.

Additionally, an unusual temperature dependent responsivity was observed for the one-stage detectors under zero bias, as shown in Fig. 4.5(b). It decreases when temperature increases from 125 to 200 K, and then increased again with temperature up to 300 K. This behavior is not yet understood. Furthermore, after reaching its peak value, the responsivity sharply decreases with further increase of the reverse bias voltage in one-stage detectors, as shown in Fig. 4.5(c). This behavior is also observed for three-stage devices at low temperatures, but at substantially small scales, however, similar behavior was never observed in our previous T2SL photodetectors with either single or multiple stages. Similar responsivity dependence on bias voltage are observed by other groups in T2SL [60] and MCT [157] photodetectors, for which trap-assisted tunneling is thought to be possibly responsible. Currently in this work, it is not clear whether the underlying mechanism is specifically related to the GaInAsSb absorber or to defect-assisted tunneling. These possible mechanisms will be investigated in the future.

Assuming that all photon-generated electrons are collected, the absorption coefficient, α, can be estimated from the device responsivity:

$$R_{\lambda}(\lambda)\frac{1.24}{\lambda}=\eta(\lambda)=(1-R)(1-e^{-\alpha(\lambda)d})\,, \tag{4.1}$$

where R_λ is the responsivity, η is the external quantum efficiency, R is the reflectance at the device surface, and d is the absorber thickness. Considering that the photocurrent was determined by the first absorber (the thinnest one), the absorption coefficient is extracted and plotted in Fig. 4.6 along with the experimental result obtained from a transmission measurement on a piece of the one-stage wafer. For most of the measured region, the absorption coefficient extracted from the responsivity is significantly higher than the typical value (2000-3000 cm^{-1}) in T2SLs, and also substantially higher than the experimental value determined from the transmission measurement as shown also in

Fig. 4.6. For example, the absorption coefficient is 6,200 and 7,500 cm^{-1} at 3.3 μm based on responsivity for one- and three-stage devices at 300 K, which is higher than the experimental value of 4,900 cm^{-1} obtained from the transmission measurement. Also included in Fig. 4.6 is the theoretically calculated absorption coefficient based on a model [158] and the optical effective mass [159] including nonparabolic effects calculated with an eight-band model [160], where a band gap of 0.3 eV was used for GaInAsSb absorber. The theoretically calculated result for α agrees well with the experimental value obtained from transmission measurement for photon energy near the bandgap up to 0.4 eV. The higher absorption coefficient extracted from the device responsivities, compared with the result obtained from the transmission measurement, suggests a gain exceeding unity. According to photoconductive theory [31], the photoconductive gain is determined by the ratio of the carrier lifetime (τ) to the transit time (τ_t), which can be larger than 1 when the carrier lifetime is longer than the transit time. The ICIPs with short absorbers can be viewed as photoconductors, especially under a bias, in which carrier transit time might be substantially shorter than the carrier lifetime, resulting in a gain exceeding unity. This high gain was similar to the gain observed in ICIPs with T2SL absorbers [92,94]. Moreover, high gains (>5) have been reported for T2SL detectors [161,162].

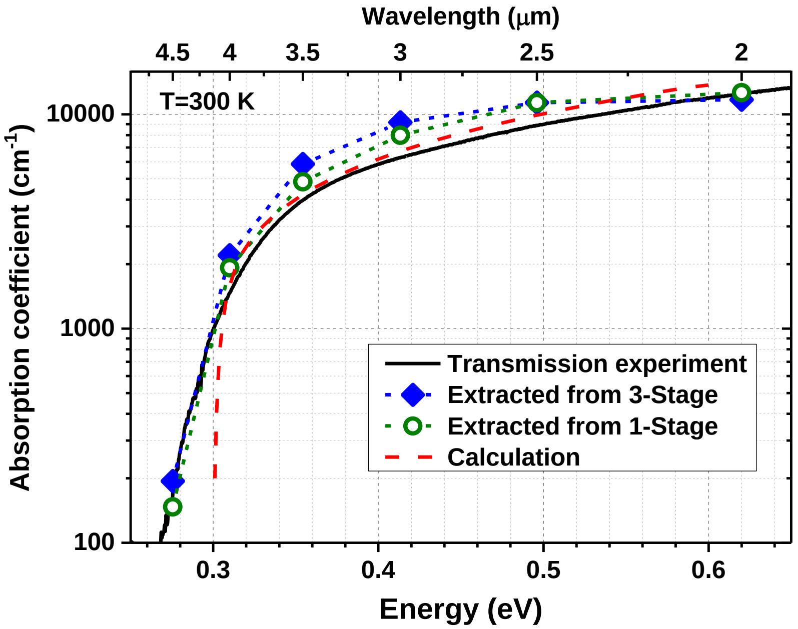

Figure 4.6: Theoretically calculated absorption coefficient compared with experimental result and extracted values from external quantum efficiency.

To further evaluate the device performance, the normalized detectivity, D^*, is determined according to the following Eq. 4.1 for devices based on their responsivities and electrical properties by considering Johnson noise and shot noise, as plotted in Fig. 4.7. The detectivities for the one- and three-stage detectors at low temperatures were not very high (1.8×10^{11} and 1.1×10^{11} cm·Hz$^{1/2}$/W at 3.3 μm and 78 K), they were limited by small R_0A values at low temperature, as discussed earlier. At 300 K, both one- and three-stage detectors had Johnson-noise limited detectivities of 10^9 cm·Hz$^{1/2}$/W at 3.3 μm under zero-bias voltage, which is comparable to the values obtained for T2SL ICIPs with a similar cutoff wavelength and for InAsSb nBn detectors with a 2-μm-thick absorber and cutoff wavelength near 4.5 μm at 300 K [55]. Under low reverse bias at 300 K, the device resistance increases by bias, as shown in Fig. 4.3(b), resulting in an increase of D^*, as shown in Fig. 4.7(b). In fact, D^* is somewhat higher in the one-stage device than that in the three-stage ICIP, because of the substantial increased responsivity in the one-stage device with the reverse bias. Here the benefit of ICIPs in terms of D^*, is not clearly observed, mostly because the R_0A values of the three-stage detectors was significantly lower than the theoretical projections for the ideal ICIPs [83] (*i.e.* transport is diffusion-limited and the diffusion length is longer than the absorber thickness), where R_0A in the three-stage ICIP would be about 10 times larger than that in the one-stage device. Issues such as leakage current associated with imperfect device passivation and bulk defects are the main reasons for the underperformance of the three-stage ICIPs presented in this work. When the total absorber thickness is equal for a multiple stage ICIP and a conventional one-stage detector, if the carrier transport is not dominated by diffusion, the expected high resistance with the discrete absorber architecture will not be achieved, resulting in a detectivity lower than theoretically projected. However, the total absorber thickness does not have to be equal, especially when the diffusion length is significantly shorter than the absorption length (=1/α). In such a case, an ICIP can have more cascade stages with the total absorber thickness significantly longer than the diffusion length and the single absorber thickness of the conventional detector. Consequently, the device resistance of an ICIP can be significantly higher so that its D^* can exceed that for a single-stage detector.

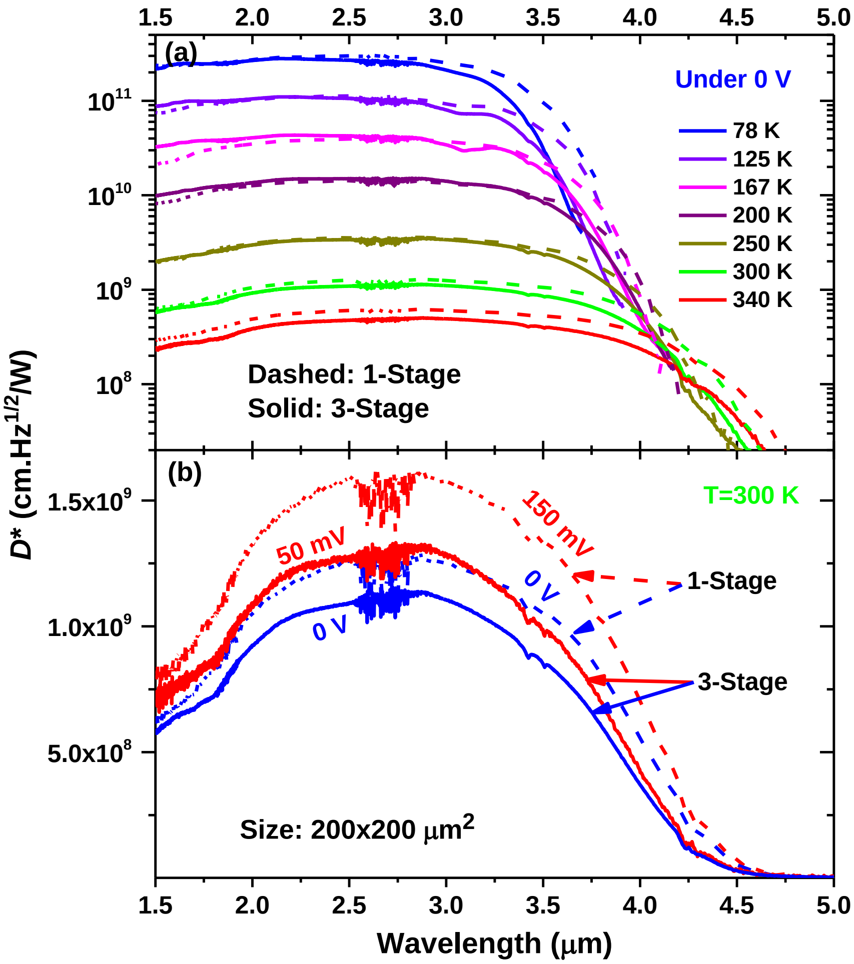

Figure 4.7: (a) Johnson noise limited *D** at different temperatures for devices at zero-bias. (b) *D** under zero-bias and a reverse bias voltage for devices at 300 K.

4.4 Summary and concluding remarks

MWIR detectors have been demonstrated at temperatures up to 340 K based on absorbers composed of the quaternary GaInAsSb alloy in both a discrete absorber architecture and a conventional single absorber structure. Absorption coefficients (*e.g.* ~5000 cm^{-1} at 3.3 μm) significantly higher than the typical value (2000-3000 cm^{-1}) in T2SLs are observed. Additionally, gain factors exceeding unity are observed in both structures. Johnson noise limited detectivity for both one- and three-stage detectors reaches 10^9 cm·Hz$^{1/2}$/W at 300 K, comparable to T2SL photodetectors with similar cutoff wavelengths. Nevertheless, the exploration of GaInAsSb-based MWIR photodetectors, particularly with the discrete absorber architecture, is in the preliminary phase and there are aspects that need to be understood and studied further. ICIPs with GaInAsSb absorbers will have potential advantages for high-speed applications with both high absorption coefficient and detectivity.

Chapter 5 Long wavelength interband cascade infrared photodetectors operating at high temperatures

5.1 Background and motivation

Long wavelength infrared photodetectors have long been investigated for environmental, industrial and military applications. Past efforts have been mainly devoted to several types of long wavelength infrared photodetectors, such as: quantum well infrared photodetectors (QWIPs) [31,32], quantum dot infrared photodetectors (QDIPs) [163,164], mercury cadmium telluride (MCT) [157,165] detectors, and III-V based T2SL [16,166,167] infrared photodetectors. These LWIR photodetectors have traditionally been limited largely to operation at low temperatures (typically 78-200 K) in order to reduce the noise and achieve high device performance. This requires cryogenic cooling which raises the cost and the size of the device package. MCT detectors can operate at room temperature [1,168], but the device performance is not optimal (*e.g.*, detectivity D^{*}~8 $\times 10^{7}$ Jones at 300 K at a cutoff wavelength near 8 µm) with a small product of resistance and device optical area (*e.g.*, ~0.0001 $\Omega\cdot\text{cm}^2$, two orders of magnitude lower than achieved by the cascade devices reported in this paper). In addition, MCT detectors must contend with undesirable issues, such as relatively small substrates of irregular size, and non-uniform epilayers. Nearly two decades ago, a p-i-n photodiode with a 2.5 µm-thick InAs/GaSb T2SL active region was reported to be capable of operation at room temperature with a cutoff wavelength of 8 µm and a peak detectivity of 1.2 $\times 10^{8}$ Jones [169], and uncooled T2SL photoconductors were also reported in the LWIR region with a responsivity of 2 mA/W [169,170]. However, little further work on LWIR SL detectors was done to improve their room temperature operation.

One of the major difficulties for room temperature operation of LWIR photodetectors is the reduced carrier diffusion length at this high temperature. The diffusion length for MWIR [89] and SWIR [171] T2SL detectors at 300 K were recently reported to be 0.4 and 0.45 μm, respectively. The diffusion length is expected to be even shorter for LWIR T2SL detectors at 300 K. With a discrete absorber architecture that circumvents this diffusion length limitation, interband cascade infrared photodetectors (ICIPs) [14,15,62,64,65,83] based on InAs/GaSb T2SL materials have great potential for high temperature operation. An ICIP consists of multiple series-connected cascade stages, where each stage is a T2SL absorber sandwiched by an electron barrier and a hole barrier, as shown in Fig. 2.5. The absorber is thinner than the diffusion length, so that photo-generated carriers can be efficiently collected without recombining during transport, while the incident light absorption is enhanced significantly by the multiple discrete absorbers. Thermal and shot noises are suppressed in ICIPs because the noise current squared is proportional to the absorber thickness and inversely proportional to the number of cascade stages, N_C [14,89]. Consequently, for the same level of current through the device, the shot noise in an ICIP is reduced approximately by $(1/N_C)^{1/2}$ compared to that in a single-stage detector. Generally, the maximum responsivity (and external quantum efficiency) that can be achieved in an ICIP is reduced by the thin individual absorbers and multi-stage architecture. This is compensated by the suppression of noise, resulting in an enhanced signal-to-noise ratio (*i.e.* detectivity) at high temperatures even with a short diffusion length and a small absorption coefficient in the LWIR region. Therefore, the device performance for ICIPs is better indicated by the detectivity rather than only by the responsivity or external quantum efficiency, in contrast to conventional detectors with a single absorber. This is appropriate when the readout circuit noise and system noise are lower than the device noise, which is true for LWIR detectors at high temperatures. Hence, ICIPs with a discrete absorber architecture should, in principle, perform better than conventional LWIR photodetectors at high temperatures. Furthermore, high-speed operation is feasible without compromising the device sensitivity, in contrast to the conventional single-absorber architecture [14,15,83]. In the MWIR region, operation of ICIPs has been demonstrated at temperatures up to 400 K [62]. Also, ICIPs were demonstrated at temperatures up to 340 K at a cutoff wavelength near 8 μm [65]. In the LWIR region, initial ICIPs, although far from optimized, were able to operate up to 220 K with reasonable performance [64]. These preliminary results suggested that further investigation may lead to improved device performance of LWIR ICIPs.

In this chapter, a comparison study is conducted to investigate the electrical and optical properties of four sets of device structures with a different number of cascade stages, absorber thickness, and the strength of electron barriers. An improved device performance of ICIPs is demonstrated where the D^* exceeds that of commercial uncooled and thermoelectrically cooled MCT detectors.

5.2 Device design and growth

Four sets of LWIR ICIP structures (11 in total) were designed, grown, and fabricated into devices for study. These ICIP structures were grown by molecular beam epitaxy (MBE) on nominally undoped *p*-type GaSb substrates with similar InAs/GaSb absorbers and cutoff wavelengths that were targeted for the LWIR region (8-12 μm) at room temperature. Similar to previous ICIPs [14,15], the electron and hole barriers are composed of digitally graded multiple GaSb/AlSb and InAs/AlSb quantum wells (QWs), respectively. The two illumination configurations for ICIP structures are shown in Fig. 2.6, where light is incident on the top surface [65]. In the regular (reg.) and reverse (rev.) illumination configurations, the electron barrier and hole barriers are closer to the top surface, respectively. Individual absorber thicknesses in the different stages are varied to achieve photocurrent matching between the cascade stages, as shown in Fig. 5.1. The T2SL period for the absorber and the unipolar barrier layer structures, in all of the wafers, are the same or similar, with some adjustments based on variations of the growth conditions and device characterization, as described below.

Set #1 consists of two wafers (S#1-8-reg. and S#1-8-rev.) with the same eight-stage ICIP structure, but opposite illumination configurations. This set was grown earlier (Oct. 2014) using an Intevac Gen II MBE chamber, with *p*-type doping of 2.5×10^{16} cm^{-3} in the absorber, and a total absorber thickness of 1391 nm. The other three sets were grown later (May-July 2016) using a Veeco GENxplor MBE chamber with the reverse illumination configuration and with *p*-type doping of 2.6×10^{16} cm^{-3} in the absorber. Set #2 includes two wafers, one is a single stage structure (S#2-1) and the other is a four-stage ICIP structure (S#2-4). The absorber thickness of S#2-1 is 1386 nm, equal to the total absorber thickness of S#2-4 and very close to the total absorber thickness of S#1-8-reg./rev. The period of the InAs/GaSb T2SL absorber was designed to be 61 and 60 Å with one InSb-like interface between the GaSb and InAs SL layers for wafers in set #1 and set #2, respectively. Their hole and electron barriers are approximately the same with seven InAs/Al(In)Sb QWs and three GaSb/AlSb QWs. Set #3 consists of four wafers, which are single stage (S#3-1), four-stage (S#3-4), six-stage (S#3-6), and eight-stage (S#3-8) ICIP structures with the same SL period (60 Å), and the same electron and hole barriers. However, the compositions of the SL period for the wafers in set #3 were slightly adjusted, with two InSb-like interfaces [70] inserted in the SL period. In Set #3, two wafers (S#3-6 and S#3-8) have the same total absorber thickness (2292 nm). Set #4 consists of three wafers, which are four-stage (S#4-4), six-stage (S#4-6) and eight-stage (S#4-8) ICIPs with the same T2SL absorber and hole barrier as S#3-6 and S#3-8. In set #4, the electron barrier was enhanced with an additional 73-Å-wide GaSb QW. A summary of designed structural parameters is provided in Table 5.1.

After MBE growth, the wafers were examined using high resolution x-ray diffraction and optical microscopy to evaluate their structural quality and defect density. Their structural qualities are comparable. Wafers in sets #1 and #2, with one InSb interface in the SL period, have tensile strains; while wafers in sets #3 and #4 with two InSb interfaces [70] in the SL period, have small compressive strains, as summarized in Table 5.1 and determined from the x-ray diffraction scans for wafers S#2-1 and S#3-6 in Fig. 5.2. However, the surface defect density was ~2×10^{5} cm^{-2} for most areas in wafer S#1-8-reg., which is significantly higher than the typical value of 1-2×10^{4} cm^{-2} observed for all other wafers. All of the wafers were processed into devices followed the process flow described in section 3.2.

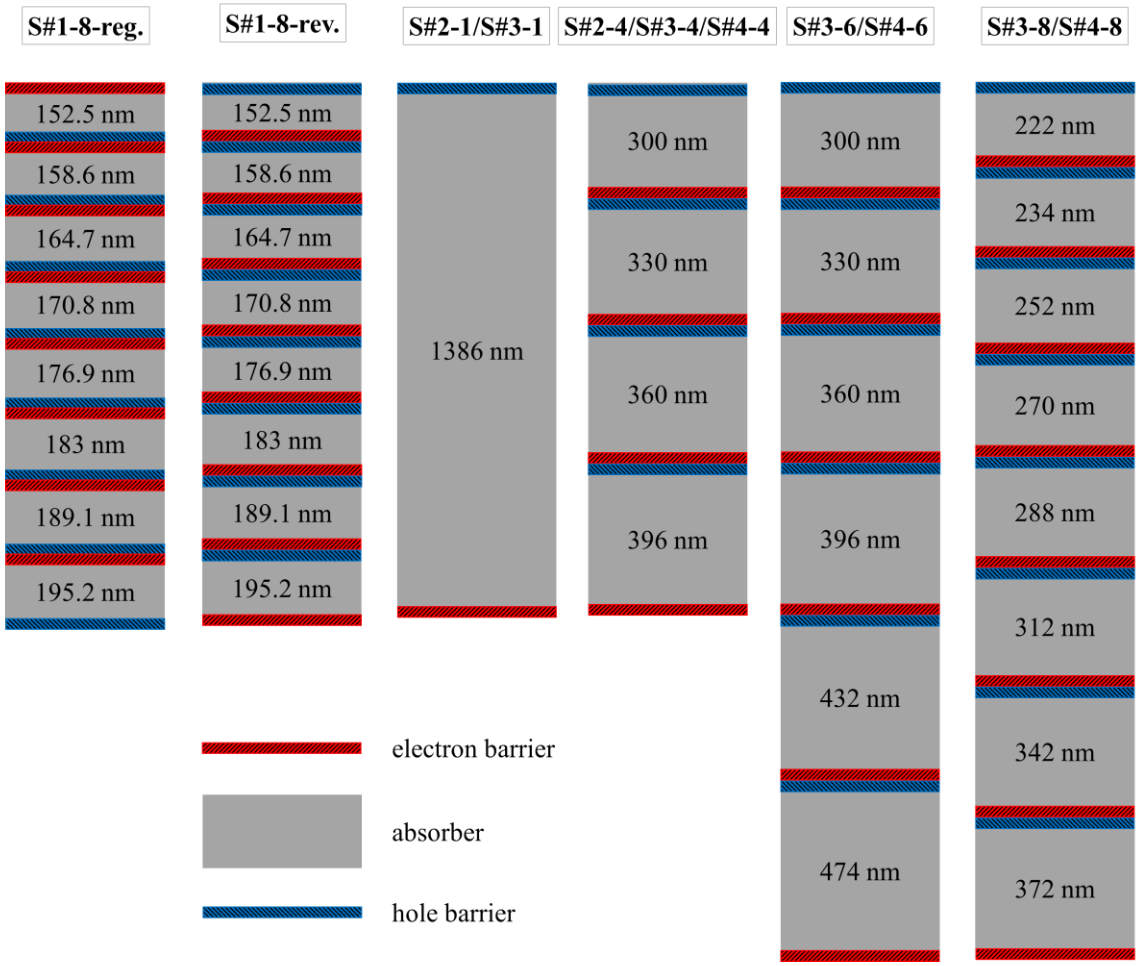

Figure 5.1: Schematic layer structures of the four sets of ICIP wafers (Total 11).

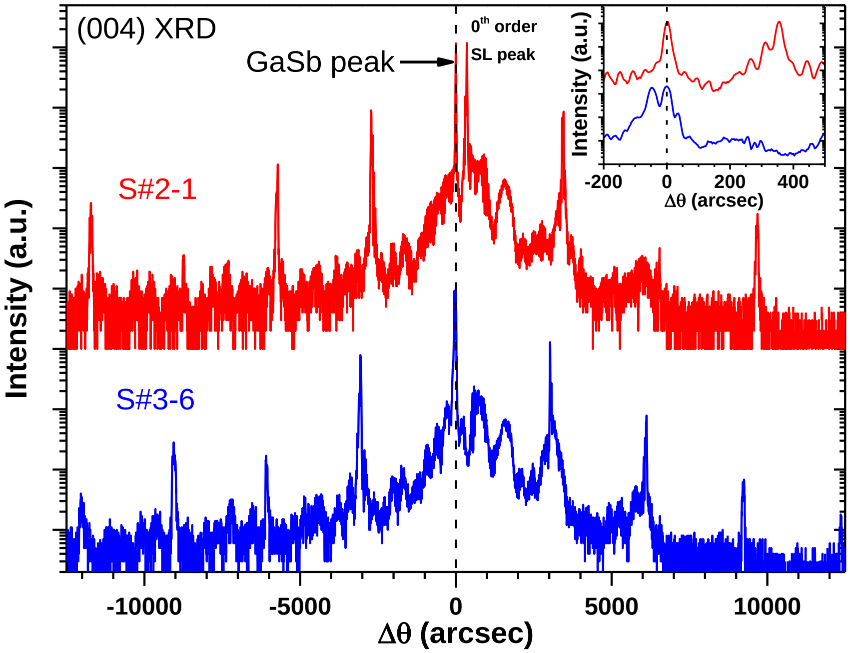

Figure 5.2: High resolution (004) x-ray diffraction scans for representative wafers S#2-1 and S#3-6.

Table 5.1: Summary of design and material parameters for each wafer.

Wafer	# of stages	GaSb/InAs in a period (Å)	InSb interfaces (Å)	# of QWs in electron barrier	Mismatch of SL in growth direction	90% λ_c (μm) at 200 K	E_g (meV) at 0 K	E_a (meV) 78-125 K	E_a (meV) 150-250 K	
								q=0	q=2	q=1
S#1-8-reg.	8	21.7/35	4.3	3	-0.100%	12.8	124	31	51	65
S#1-8-rev.	8	21.7/35	4.3	3	-0.390%	10.7	144	27	99	118
S#2-1	1	22.3/33.9	3.8	3	-0.205%	10.2	150	53	73	89
S#2-4	4	22.3/33.9	3.8	3	-0.290%	9.8	154	62	97	113
S#3-1	1	24.7/31	2.1+2.2	3	0.111%	9.1	164	45	132	148
S#3-4	4	24.7/31	2.1+2.2	3	0.128%	9.3	162	42	124	140
S#3-6	6	25.2/31	1.9+1.9	3	0.037%	9.0	167	39	139	156
S#3-8	8	25.2/31	1.9+1.9	3	0.043%	8.8	171	40	149	166
S#4-4	4	25.2/31	1.9+1.9	4	0.104%	8.8	170	41	154	170
S#4-6	6	25.2/31	1.9+1.9	4	0.086%	8.8	171	44	157	173
S#4-8	8	25.2/31	1.9+1.9	4	0.092%	8.7	174	45	157	173

5.3 Device characterization and analysis

Electrical and optical properties of devices from each wafer were obtained and analyzed through measurements of current density-voltage characteristics and photo-response spectra. Table 5.1 summarizes some of the material properties such as: cutoff wavelength λ_c, bandgap E_g, and activation energy E_a, extracted from the measurements. The cutoff wavelengths of devices from all wafers were in the LWIR region at high temperatures (T ≥200 K), with λ_c of 11-12 µm at 200 K for devices in set #1, about 10 µm at 200 K for devices in set #2, and near 9 µm at 200 K for devices in set #3 and #4. Their detailed properties are described and discussed below.

5.3.1 Electrical properties

The characteristics of dark current density (J_d) *vs.* bias voltage (V) from low to high temperatures (78-250 K) are shown in Fig. 5.3 for representative devices from all sets. For each set, the detectors with more stages had lower dark current densities, which is consistent with the theoretical projections for thin absorbers and multiple stages [83]. For example, taking the lowest among the devices with the same cascade stages, the dark current density at 78 K and reverse bias of 50 mV for the one-stage, four-, six- and eight-stage devices was 9.1×10^{-4}, 3.1×10^{-5}, 4.2×10^{-5} and 2.8×10^{-5} A/cm^2, respectively. Because the 90% cutoff wavelengths for these devices were 7.4-8.3 µm at 78 K, the corresponding dark current densities in MCT are 2.2×10^{-9}-5.0×10^{-8} A/cm^2, in accordance with “Rule 07” [172]. The much higher dark current density in ICIPs is attributed to the generation-recombination dominated mechanism in narrow bandgap T2SL materials at low temperatures [173]. For the two eight-stage devices in set #1, the device from S#1-8-rev. had a lower dark current density mainly due to the shorter cutoff wavelength (larger bandgap) than that from S#1-8-reg. For the devices with same cascade stages, although the cutoff wavelengths are longer for set #2 compared to set #3, the device from S#2-1 had a lower dark current density than the device from S#3-1, and the device from S#2-4 had the lowest dark current density among the three four-stage devices from different sets. This contradicts projections based on their bandgaps, and it may be related to only one InSb interface in T2SL period in set #2 instead of two interfaces in sets #3 and #4. Note that in set #2, the single InSb interface is thicker than the individual InSb interfaces that are included twice per period in sets #3 and #4 (this is similar to what was discussed in Ref [70]). Comparing devices with same cascade stages, the detectors in set #4 have lower dark current densities than those in set #3. This was attributed to the enhanced electron barrier in set #4, which further suppresses possible intraband tunneling between stages [15]. While it was sufficient to block the intraband tunneling for MWIR ICIPs [15,96] with three QWs in the electron barrier, this might not be enough QWs for LWIR ICIPs, where the minority carrier concentrations are much higher and the electron effective mass is smaller. Hence, the probability of substantial intraband tunneling through an electron barrier with three QWs could be increased for LWIR ICIPs and, consequently, an enhanced electron barrier is required to strengthen the suppression of intraband tunneling current. This is supported by the analysis of the negative conductance for these devices, which will be presented in Section 7.3.2.

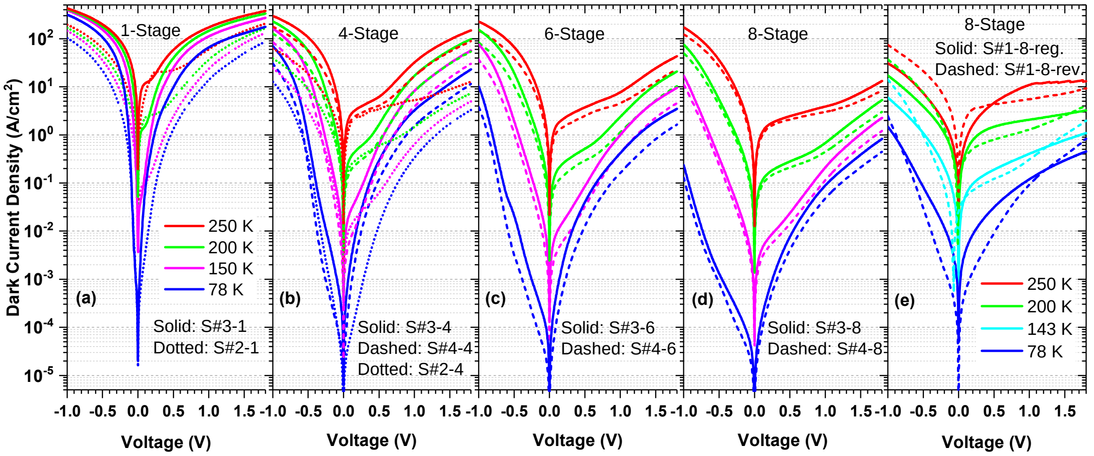

Figure 5.3: Dark current densities *vs*. bias voltage from 78 to 250 K for representative devices from all sets. In (a-d), dotted, solid and dashed lines represent devices from set #2, 3 and 4, respectively, while the devices from set #1 are shown in (e). Positive voltage denotes reverse bias (most devices had reverse configuration), while voltage polarity of S#1-8-reg. is reversed for a clear comparison.

From the measured J_d-V curves, the inverse product of zero-bias resistance and device area $(R_0A)^{-1}$ (*i.e.*, conductivity) for devices with different sizes was obtained. The size dependences of $(R_0A)^{-1}$ are plotted for these devices (at 200 K) as a function of the perimeter (P) to area (A) ratio in Fig. 5.4. As can be seen, the value of $(R_0A)^{-1}$ from all sets exhibited size dependence, indicating imperfect passivation on side walls of devices and/or possibly non-uniform distributions of defects for these wafers. Devices from wafer S#1-8-rev. exhibit a strong size dependence of $(R_0A)^{-1}$, which is correlated to the large bulk resistance associated with the eight discrete thinnest absorbers. The large bulk resistance requires good sidewall passivation, otherwise significant leakage currents can flow on the side walls. In contrast, although fabricated at the same time, because of the substantially higher defect density and the longer cutoff wavelength, the devices from S#1-8-reg. have a lower bulk resistance and $(R_0A)^{-1}$ has a relatively weak size dependence. As expected, $(R_0A)^{-1}$ for the one-stage devices was the highest among all detectors, and its size dependence was also significant. There are large variations for devices from S#2-1, suggesting structural non-uniformity. From Fig. 5.4(b), for multiple stage ICIPs, there is a reduction in $(R_0A)^{-1}$ with an increase in the number of the cascade stages for devices in sets #2, #3, and #4. For ICIPs in sets #3 and #4, the comparisons are more meaningful because of the nominally identical absorber structures with very similar cutoff wavelengths. In addition to a further reduction in $(R_0A)^{-1}$ with the enhanced electron barrier in set #4, the conductivity for these ICIPs showed relatively weak device-size dependence. This may be due to variations in passivation on uneven wet-etched side walls when wafers were fabricated into devices at different times. This weak dependence may also be associated with the enhanced electron barrier which can suppress the leakage current through surface states. This idea merits further investigation with additional structures. The passivation for etched surfaces of InAs/GaSb T2SL infrared detectors has been a long-standing issue [174]. This issue will be considerably alleviated by anisotropic dry-etching techniques that can produce smooth surfaces and will be available for future work.

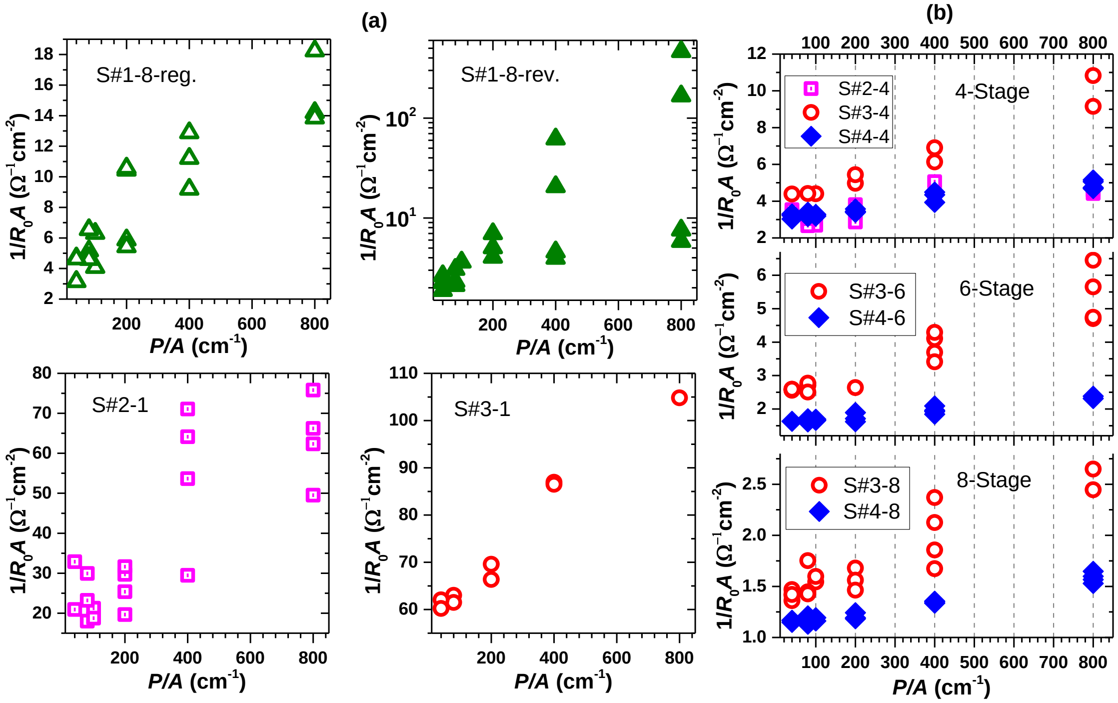

Figure 5.4: $(R_0A)^{-1}$ *vs.* P/A for (a) eight-stage devices in set #1 and one-stage devices in sets #2 and #3, (b) four-, six- and eight-stage devices in sets #2, #3 and #4 at 200 K.

To identify the dominant carrier transport mechanisms, R_0A was measured over a wide range of temperature (T) for representative devices and fit according to the modified Arrhenius Equation 1.13. From the Arrhenius plot, it is clear that there are separate low- and high-temperature regions with good linear fits. This means there are two separate activation energies, one for the low-T range of 78-125 K and the other for the high-T range of 150-250 K. The extracted values of E_a are shown in Table 5.1, where q=0 is used for the low-T range and q=1 and 2 are used for the high-T range.

As can be seen from Fig. 5.4, devices made from all wafers had surface leakage current to some degree. To evaluate the effect of the leakage current, for each wafer, the activation energy was extracted from many devices with different sizes. The variations from device to device were within 15-25% for the extracted E_a with q=2. For example, at temperatures above 150 K, the range of activation energies for devices from wafers S#3-1, 4 and 6 was 117-147 meV, and from wafer S#3-8 and wafers in set #4 was 127-159 meV. While the activation energies of smaller ($\leq 100\times100\ \mu m^2$) devices tended to be lower compared to those of larger ones, the E_a values were irregular for larger ($\geq 200\times200\ \mu m^2$) devices. As shown in Table 5.1, the activation energy for the representative device ($200\times200\ \mu m^2$ size) from each wafer was among the highest compared to other device sizes that should be less sensitive to surface leakage current.

At low temperatures, the activation energies of the devices from S#2-1 and S#2-4 were close to half of the zero-temperature bandgap, implying a generation-recombination (GR) limited transport through defect states (bulk defects and/or surface states). The activation energies of the devices from wafers in sets #1, #3 and #4 were far below their bandgaps, suggesting a transport mechanism similarly dominated by trap-assisted tunneling [175]. At high temperatures, devices from the wafers in sets #3 and #4 exhibited diffusion limited behavior with activation energies nearly equal to the zero-temperature bandgap, as shown in Fig. 5.5. For devices in sets #1 and #2 at high temperatures, the activation energies of S#1-8-reg. and S#2-1 were close to one-half of the bandgap, while it was between one-half and one bandgap for S#1-8-rev. and S#2-4. As can be seen from Table 5.1, wafers from sets #1 and #2 showed relatively large tensile strain while wafers from sets #3 and #4 had small compressive strain with two InSb interfaces included in the absorber SL period. These differences may be related to the more diffusion-limited transport observed at high temperatures for devices from wafers in sets #3 and #4.

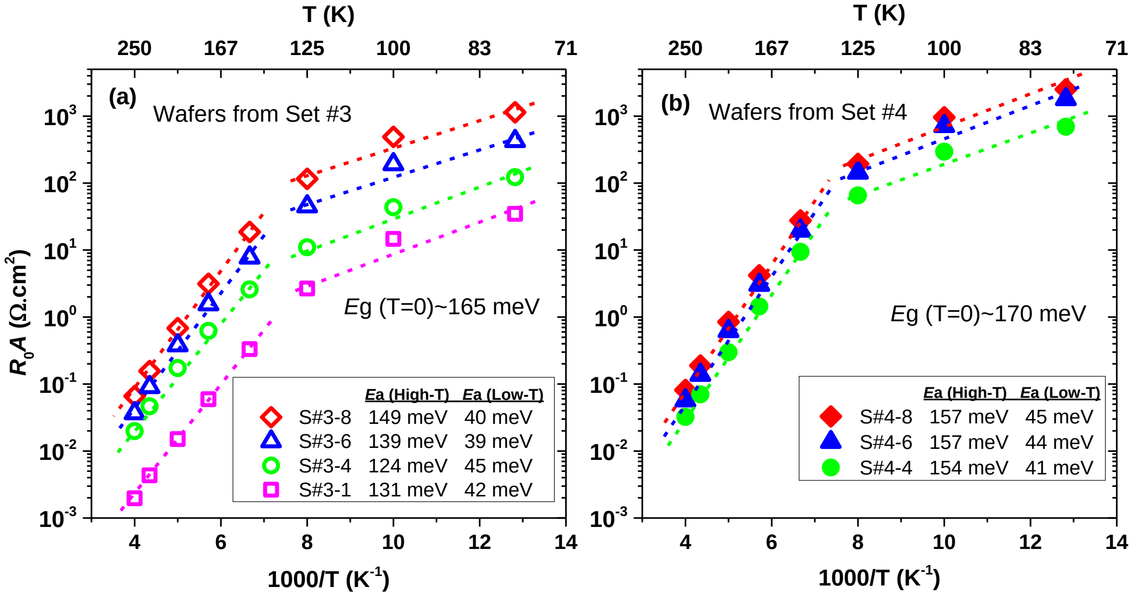

Figure 5.5: Arrhenius plot of R_0A for devices from wafers in (a) set #3 and (b) set #4.

5.3.2 Negative differential conductance

During measurements of the dark current characteristics of these devices, sawtooth features were observed in the reverse bias region of the J_d-V curve at high temperatures. By differentiating the J_d-V curve, negative differential conductance (NDC) peaks are clearly observed where the number of peaks equaled the number of stages of the ICIPs, as shown in Fig. 5.6, for devices with differing numbers of cascade stages from the four sets. The sawtooth features and NDCs were not observed at low temperatures but appeared only when the temperature was raised to a certain level, and intensified with a further increase in temperature. This is different from NDCs that were observed from early MWIR ICIPs only at low temperatures and under significantly higher reverse bias voltages [15]. This phenomenon is also different from NDC features observed in AlGaAs/Al$_x$Ga$_{1-x}$As SLs [176] and InAs/(GaIn)Sb T2SL diodes [177] associated with resonant tunneling of majority carriers in QWs and Wannier-Stark states in the depletion region of the T2SL diode. Again, for both SL samples, NDCs were reported only at low temperatures [96,173]. The distinct temperature dependence of NDCs and the correlation with the number of cascade stages observed in this study suggests that the intraband tunneling of minority carriers (*i.e.* electrons) through the electron barriers was mainly responsible for the observed phenomena. This is because the minority carrier concentration increased exponentially with temperature such that the intraband tunneling current through the electron barrier is significantly strengthened at high temperatures with reduced electron effective mass. For wafers in sets #1, #2 and #3, the electron barrier is composed of three digitally graded GaSb/AlSb QWs with well thicknesses of 33, 43, and 53 Ȧ, respectively. Under an appropriate reverse bias, the energy levels in the QWs of the electron barrier could be aligned and matched to the conduction miniband of the absorber in one stage, resulting in a resonant tunneling through these energy levels with a peak in dark current. Consequently, an NDC is generated when the bias is off the resonant condition. Hence, with N_C cascade stages, there could be N_C peaks in the dark current and corresponding NDCs. The magnitude of the resonant peak current and NDC would depend on the strength of the electron barrier. To further test this idea, ICIP structures in set #4 were designed and grown with an extra QW added in the electron barrier to reduce the intraband tunneling. As can be seen from Fig. 5.6, both dark current density and NDCs are substantially reduced for detectors in set #4 compared to that in set #3, which supports the consumption.

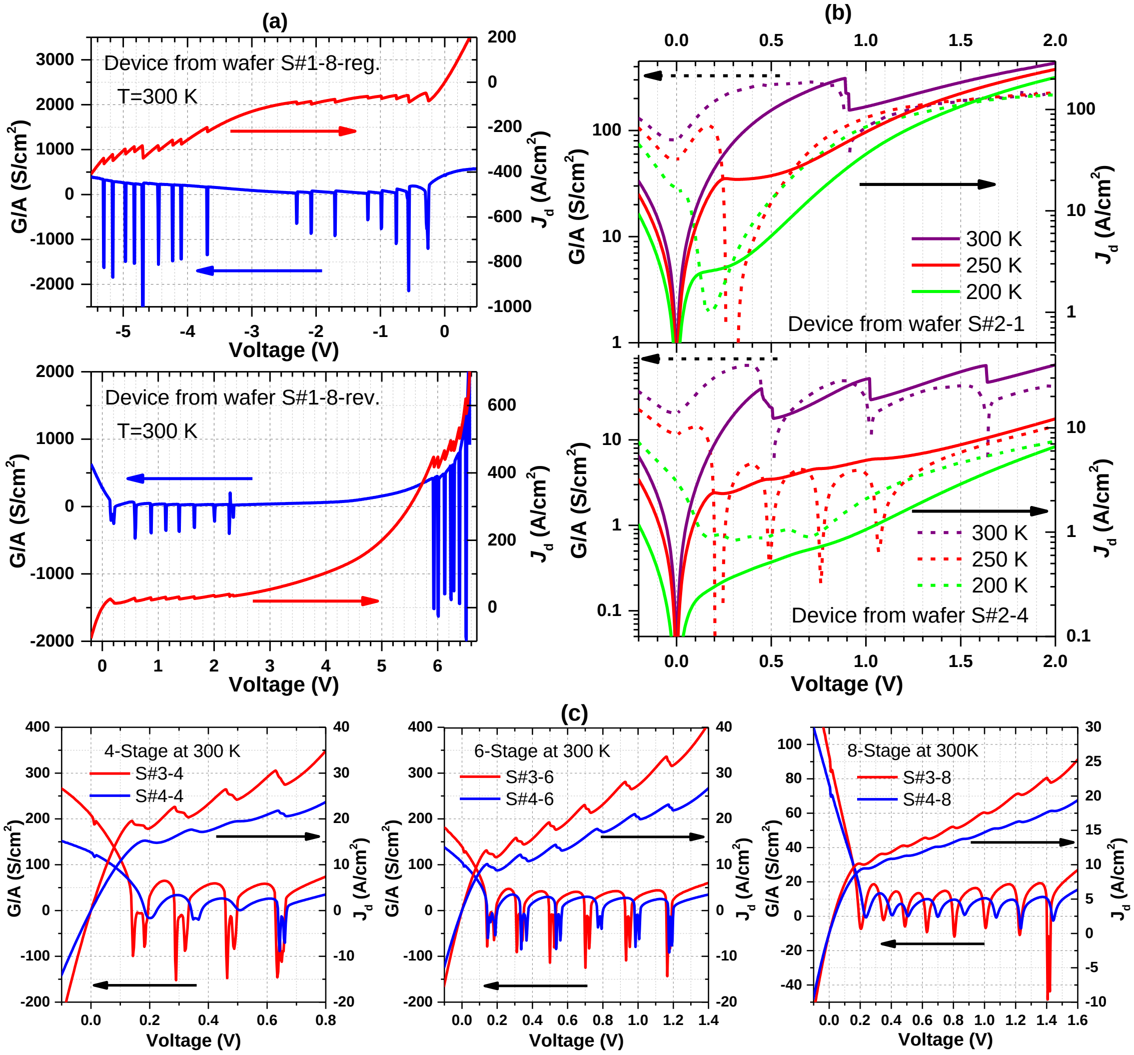

Figure 5.6: Differential conductance/area (*G/A*) and dark current density *vs.* voltage bias for devices in (a) set #1, (b) set #2 and (c) sets #3 and #4. In (b), the left vertical axis for *G/A* is a logarithmic scale that does not extend to negative values. The fourth dark current peak and the related NDC for the device from S#2-4 at 300 K appeared at a voltage beyond 2 V.

For the two eight-stage detectors in set #1, more dark current peaks with associated NDCs appeared with further increases in reverse bias voltage as shown in Fig. 5.6(a). Under large reverse bias voltages, the higher energy levels in the QWs of the electron barriers could be involved in resonant tunneling and the number of NDCs in the large reverse bias region did not always equal the number of cascade stages.

However, these NDCs associated with the higher energy levels were not found from devices in sets #2, #3 and #4 with large bias voltage (up to 5 V to avoid damage), which might be due to the larger bandgap in these sets compared to set #1.

For devices in sets #3 and #4, NDCs started to appear at 280 K. For devices in set #2, NDCs appeared from 200 K possibly due to the narrower bandgap in set #2 compared to sets #3 and #4. There may be other causes for the appearance of NDCs at this relatively low temperature in set #2. This shall be the subject of further research. Also, NDCs at 200 K appeared at a low reverse bias voltage and the required bias voltage for NDCs increased at higher temperatures as shown in Fig. 5.6(b). This was probably due to the increase of voltage drop percentage on the series resistance and the increase of tunneling current at high temperatures. It should be mentioned that the NDC was not observed in our MWIR ICIPs (with very similar electron barriers) in a wide range of temperature (up to 400 K). The absence of NDC in MWIR ICIPs is probably due to their lower minority carrier concentration and the larger band gap for the MWIR region.

5.3.3 Optical properties and device performance

The photo-response spectra of devices at various temperatures were measured using an FTIR spectrometer and calibrated with a blackbody source (aperture diameter of 1.52 cm) at 600 K with a 2π field of view (FOV). Figure 5.7 shows the cutoff wavelength and estimated bandgap as a function of temperature for a device from wafer S#4-4. The 90% cutoff wavelength was determined by the wavelength at which the responsivity fell to 10% of its maximum value. For this device, the 90% cutoff wavelength is 7.6 μm at 78 K, extending to 10.7 μm at 300 K. The bandgap narrowing of semiconductors with increasing temperature is related to the increased lattice constant (thermal expansion) and electron-lattice interaction that shifts the relative positions of the conduction and valence bands. The temperature-dependence of the bandgap is estimated using the Varshni formula [26] with Eq. 1.15. The fitting curve with Varshini parameters for the detector from wafer S#4-4 is shown in Fig. 5.7. Similarly, the zero-temperature bandgaps and cutoff wavelengths for devices from other wafers were obtained, representative values of which are given in Table 5.1. It can be seen that wafers in sets #3 and #4 had very similar zero-temperature bandgaps, while E_g (T=0) is smaller for wafers in sets #1 and #2.

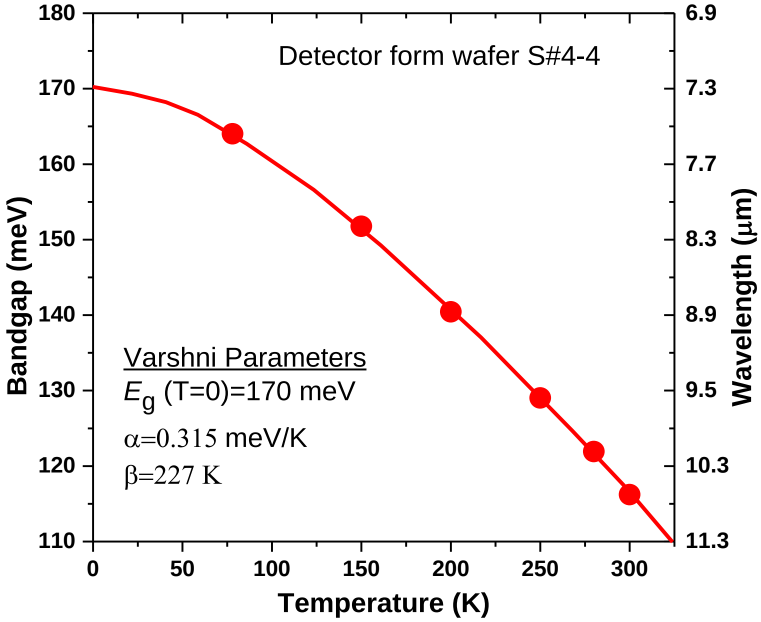

Figure 5.7: Temperature dependent cutoff wavelength and estimated bandgap for a device from wafer S#4-4. The fitting Varshni parameters for the device are shown.

Responsivity curves are shown in Fig. 5.8 for the detectors from S#1-8-reg. and S#1-8-rev. in set #1, with a 90% cutoff wavelength of 10.4 and 8.9 μm at 78 K, respectively. The responsivities at 78 K and 8 μm for devices from S#1-8-reg. and S#1-8-rev. were 0.075 and 0.114 A/W, respectively. The relatively low responsivities for the two eight-stage detectors were mainly due to the thin absorbers (153-195 nm, as shown in Fig. 5.1). Both detectors operated at temperatures up to 250 K, and their responsivities were insensitive to the bias voltage at low temperatures. However, the responsivity of the device from S#1-8-reg. depended substantially on bias voltage at temperatures above 125 K, while the responsivity of the device from S#1-8-rev. was bias independent up to 200 K. The difference is probably caused by variations of the material quality with a higher defect density and a longer cutoff wavelength in S#1-8-reg. On the other hand, the opposite illumination configurations for the two wafers in set #1 also contributes to the differences in performance. With the regular illumination configuration, the propagation of incident light is along the same direction as the transport of minority carriers and consequently most of the photo-generated electrons are relatively far from the collection point, resulting in an increased possibility of recombination for these electrons at elevated temperatures. Thus, a reverse bias may be required with the regular illumination configuration to facilitate the collection of photo-generated carriers at high temperatures with short carrier lifetimes at long wavelengths (especially when the material quality is not optimal). For the reverse illumination configuration, the propagation of incident light is in the opposite direction of the transport of minority carriers, making most of the photo-generated electrons close to the collection point, and resulting in more efficient collection of the photo-generated electrons without a bias voltage. Therefore, for detectors with *p*-type absorbers, the reverse illumination configuration is preferred.

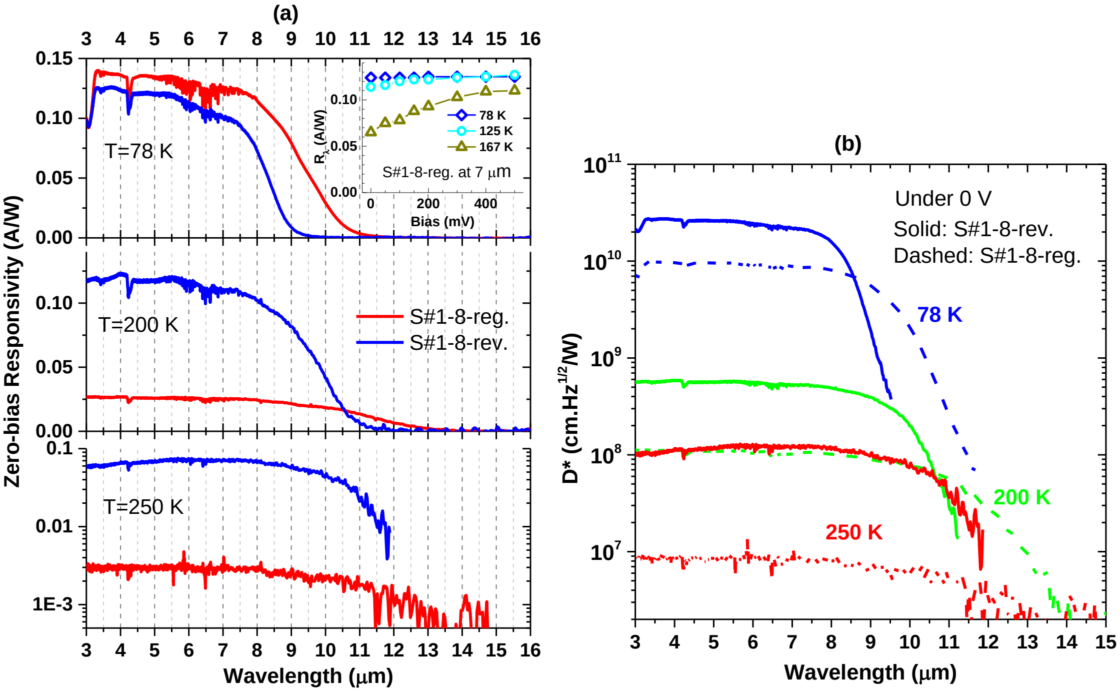

Figure 5.8: (a) Zero-bias responsivity and (b) *D** for the detectors from wafers S#1-8-reg. and S#1-8-rev. in set #1 under 25 °C background with a 2*π* FOV. The inset shows the bias dependence of responsivity for a detector from S#1-8-reg.

To evaluate the overall device performance, the normalized detectivity, D^*, is estimated according to Eq. 2.1. The Johnson-noise limited D^* is shown in Fig. 5.8(b) for devices (at zero-bias) from set #1. The D^* is significantly lower in the device from S#1-reg. than in the device from S#1-rev. For example, the D^* for a wavelength (λ) of 7 μm at 78 K was 8.7×10^9 and 2.2×10^{10} cm·Hz$^{1/2}$/W for the device from S#1-8-reg. and S#1-8-rev, respectively. The difference in D^* between these devices increased at high temperatures under zero-bias voltage, which was probably due to the bias-dependent responsivity in S#1-reg. at elevated temperatures. The D^* values for a wavelength of 8 μm at 200 K were 1.0×10^8 and 4.9×10^8 cm·Hz$^{1/2}$/W for devices from S#1-8-reg. and S#1-8-rev, respectively.

The responsivity of the detectors from S#2-1 and S#2-4 in set #2 is shown in Fig. 5.9, where the observed 90% cutoff wavelength varies from 8.3 μm at 78 K to 10.2 μm at 200 K. The responsivities at 78 K and 7 μm for devices from S#2-1 and S#2-4 were 0.89 and 0.22 A/W, respectively, which scales approximately with their individual absorber thicknesses, indicating efficient collection of photo-generated carriers at this low temperature. The detector from S#2-1 operated at temperatures up to 250 K, while that from wafer S#2-4 operated at up to 280 K. At low temperatures, their responsivities first increased slightly with reverse bias voltage and then dropped with further increase in the reverse bias voltage. Similar responsivity dependences on bias voltage were observed by other groups in T2SL and MCT photodetectors, for which trap-assisted tunneling is thought to be possibly responsible [60,157]. Nevertheless, at high temperatures (*e.g.*, 200 K and above), the responsivity decreased substantially at zero bias, especially in one-stage devices (S#2-1) with a thick absorber, possibly due to a reduction of the diffusion length at high temperatures. Also, the response spectrum of the one-stage device is noisy at 250 K compared to that of the four-stage device at the same temperature. The temperature dependence of zero-bias responsivity at 7 μm is shown in Fig. 5.10(a) for devices from wafer sets #2, #3, and #4, where the responsivity of the one-stage detectors was scaled down by a factor of 4 for better comparison (responsivity is proportional to the thickness of individual absorbers). As can be seen from Fig. 5.8(a) and Fig. 5.9(b), the zero-bias responsivity at 7 μm at low-*T* (*e.g.*, 78-125 K) is approximately proportional to the individual absorber thickness. Based on this, the extracted absorption coefficient ranged from 1000 to 1900 cm^{-1} depending on the cutoff wavelength for devices from all wafers. At 200 K, because of the narrowing of the bandgap with increasing temperature, the extracted absorption coefficient at 7 µm increased to 1800-2200 cm^{-1} based on the zero-bias responsivity or the maximum responsivity at a bias voltage (for devices in set #2 and the one-stage device in set #3). The extracted values for the absorption coefficient are in good agreement with early reported experimental measurements and theoretical calculations for T2SLs in the LWIR region [135,178], implying efficient collection of photo-generated carriers in all devices at 78 K, and even at high temperatures for the multi-stage ICIPs from sets #3 and #4, as will be discussed in more detail below.

Detectors from both wafers in set #2 had a D^* value larger than 10^{11} $\mathrm{cm\cdot Hz^{1/2}/W}$ at 78 K. For example, as shown in Fig. 5.10(b), the D^* was 1.0×10^{11} and 1.3×10^{11} $\mathrm{cm\cdot Hz^{1/2}/W}$ at 7 µm for devices from wafer S#2-1 and S#2-4, respectively. At 200 K, the D^* at 7 µm for the detector from wafer S#2-1 was 4.3×10^{8} $\mathrm{cm\cdot Hz^{1/2}/W}$ (1.2×10^{9} $\mathrm{cm\cdot Hz^{1/2}/W}$ under 150 mV), and was 9.0×10^{8} $\mathrm{cm\cdot Hz^{1/2}/W}$ (1.4×10^{9} $\mathrm{cm\cdot Hz^{1/2}/W}$ under 150 mV) for detectors from S#2-4. This demonstrates the advantages of multi-stage ICIPs over the conventional one-stage detector at both low and high temperatures, even with equal total absorber thickness. With more cascade stages to increase the optical absorption and further suppress the noise, more significant benefits are expected using ICIPs. Compared to PV MCT detectors from Vigo System [1,2] at 8 µm (D^* is 4-5$\times10^{8}$ $\mathrm{cm\cdot Hz^{1/2}/W}$ at 195 K), the D^* for the ICIPs in set #2 is larger (1.0×10^{9} $\mathrm{cm\cdot Hz^{1/2}/W}$ under a smaller bias). Table 5.2 shows D^* for ICIPs from the other wafers. At 200 K, there are some differences in D^* at 7 µm and 8 µm for detectors made from sets #3 and #4, as can be seen from Fig. 5.10(b) and Table 5.2. This is because at 200 K the cutoff wavelength was close to 8 µm for those devices.

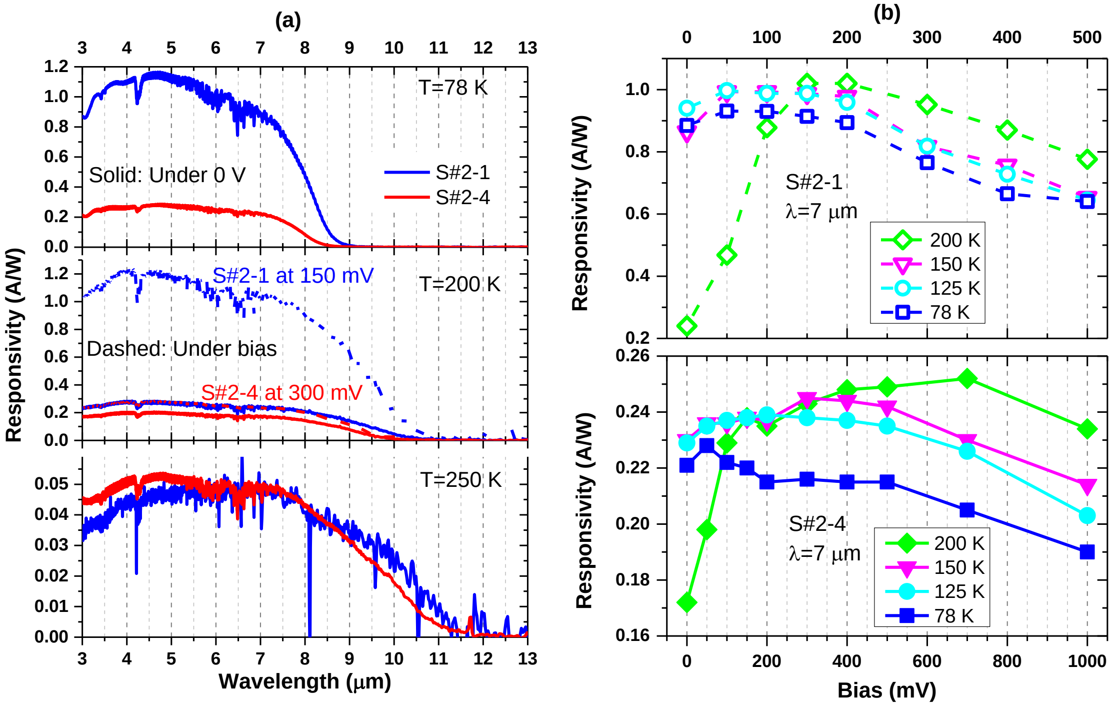

Figure 5.9: (a) Responsivity *vs.* wavelength at different temperatures and (b) Bias dependent responsivity for the detectors from S#2-1 and S#2-4 in set #2.

Table 5.2: Performance at a wavelength of 8 μm for ICIPs (background temperature=25 °C, FOV=2*π*) and MCT detectors at 200 and 300 K.

T	Detector	S#2-1	S#2-4	S#3-1	S#3-4	S#3-6	S#3-8	S#4-4	S#4-6	S#4-8	PV MCT
200 K	Zero-bias D^* (cm·Hz$^{1/2}$/W)	3.7×10^{8}	7.5×10^{8}	8.2×10^{8}	7.8×10^{8}	1.0×10^{9}	8.8×10^{8}	7.4×10^{8}	1.1×10^{9}	7.7×10^{8}	$\geq4.0\times10^{8}$
	R_λ (A/W)	0.21	0.14	0.70	0.19	0.17	0.11	0.14	0.14	0.09	≥1.5
	R_0A (Ω·cm^2)	0.035	0.304	0.015	0.176	0.383	0.687	0.304	0.628	0.846	≥0.0006
200 K	D^* under bias (cm·Hz$^{1/2}$/W)	1.0×10^{9} (150 mV)	1.1×10^{9} (150 mV)	1.0×10^{9} (50 mV)	8.7×10^{8} (100 mV)	1.1×10^{9} (100 mV)	1.0×10^{9} (150 mV)	8.8×10^{8} (100 mV)	1.3×10^{9} (100 mV)	8.6×10^{8} (150 mV)	\
	R_λ (A/W)	0.90	0.19	0.70	0.19	0.17	0.11	0.14	0.14	0.09	\
	R_DA (Ω·cm^2)	0.41	1.35	0.125	0.499	0.887	1.79	1.03	1.76	2.23	\
300 K	Zero-bias D^* (cm·Hz$^{1/2}$/W)	\	\	\	7.8×10^{7}	1.1×10^{8}	1.2×10^{8}	7.4×10^{7}	1.0×10^{8}	1.2×10^{8}	$\geq4.0\times10^{7}$
	R_λ (A/W)	\	\	\	0.20	0.21	0.17	0.13	0.17	0.15	≥0.3
	R_0A (Ω·cm^2)	\	\	\	0.0026	0.0048	0.0082	0.0051	0.0072	0.0105	≥0.0001

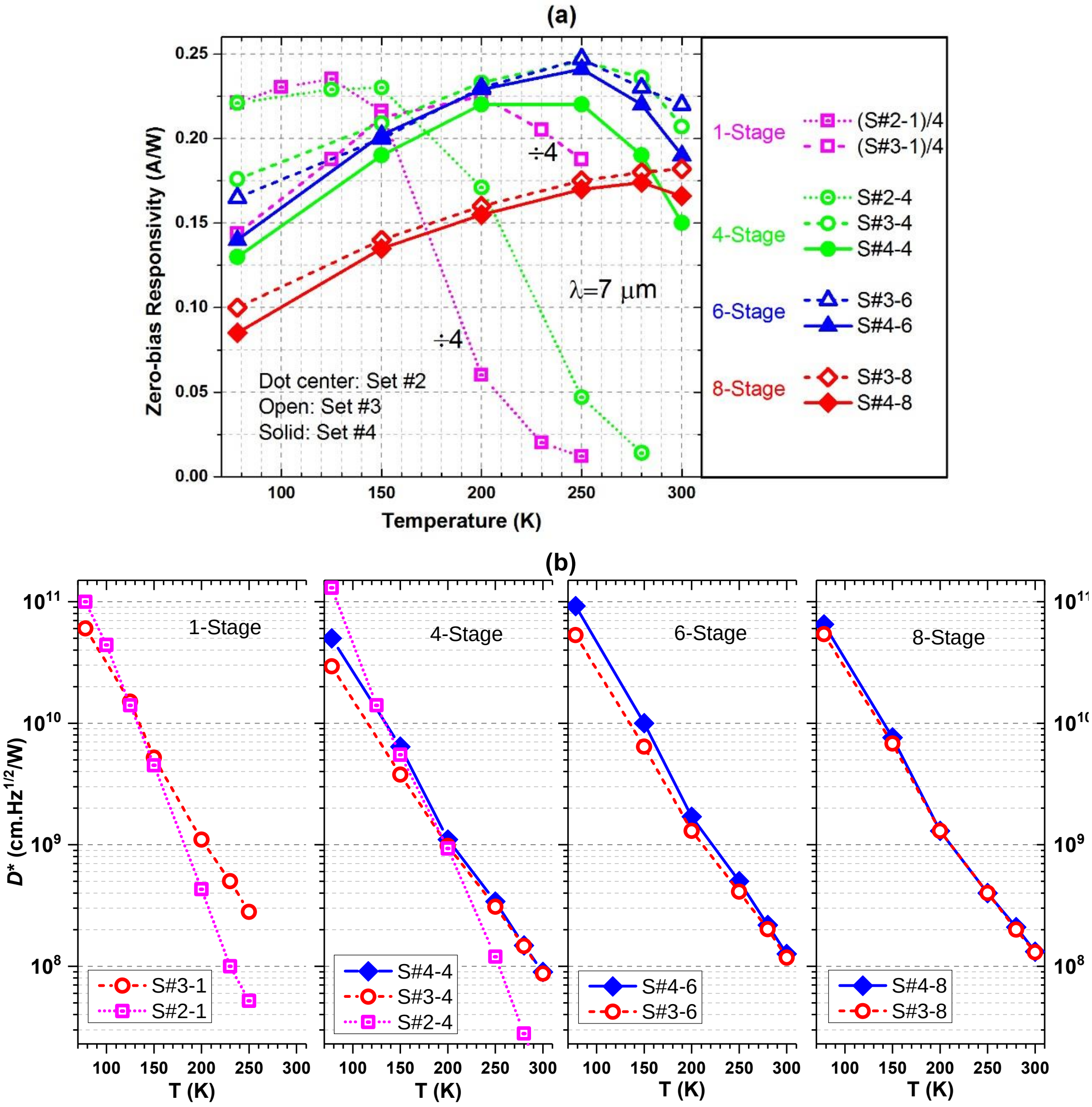

Figure 5.10: (a) Zero-bias responsivity and (b) zero-bias D^* at 7 µm *vs.* temperature for all the detectors from sets #2, #3 and #4, where the responsivity for the one-stage detectors was divided by a factor of 4 for better comparison.

The photo-response spectra for the detectors in sets #3 and #4 are shown in Fig. 5.12. The 90% cutoff wavelength at 78 K for the detectors in set #3 was about 7.4-7.9 µm, which is shorter than that (8.5 µm) in set #2. Room temperature operation was achieved for the multi-stage ICIPs in these two sets, with a 90% cutoff wavelength around 10.4-10.7 µm at 300 K. Responsivities for detectors from S#3-4 (S#4-4) and

S#3-6 (S#4-6) were nearly equal (e.g. 0.22-0.23 A/W at 200 K at 7 µm), indicating an effective implementation of photocurrent matching between different stages in these four- and six-stage detectors. Comparing the responsivities of devices with the same cascade stage number, the devices with the enhanced electron barrier from set #4 had only slightly lower responsivities (~7%) than the devices in set #3 at medium temperatures (150-250 K), while the dark current was reduced (~20%) more considerably, as shown in Fig. 5.3. Thus, the lower signal is compensated by the more significantly reduced noise, and the signal-to-noise ratio (D^*) is higher for devices with the enhanced electron barrier in set #4, as can be seen from Fig. 5.10. At 300 K, the D^* was higher than 1.0×10^8 cm·Hz$^{1/2}$/W at wavelengths near 7-8 µm, as shown in Figs. 5.10 and 5.13. From Table 5.2, D^* for both six- and eight-stage ICIPs from sets #3 and #4 exceeds the reported value for uncooled commercial MCT detectors [1,2].

Intense oscillations were observed in the response spectrum as illustrated in Fig. 5.11. They were caused by reflections in the Fabry-Perot cavity formed from the top surface to the interface between the substrate and the heat sink. This is verified by the small separation Δ (~5.8 cm^{-1}) of adjacent peaks from the oscillation pattern in the inset to Fig. 5.11. The cavity length L is estimated at about 230 µm based on the equation $\Delta=1/(2nL)$ with an average refractive index $n\approx3.7$, which is consistent to the thickness of a typically lapped substrate. The oscillations could be avoided or reduced by intentionally tilting the substrate at a small angle (~1-2°) during the lapping process [128]. Due to these internal reflections in such a cavity, gain in responsivity (or quantum efficiency) might be possible in these detectors [178]. Further investigations, such as transmission experiments, would be required to verify this possibility.

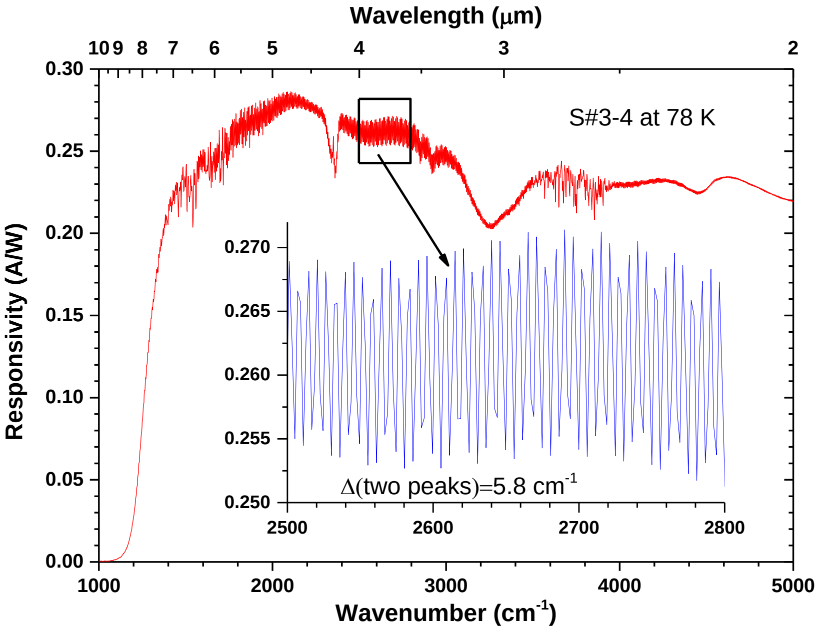

Figure 5.11: Responsivity *vs*. wavenumber at 78 K for a detector from S#1-4, where details of the oscillations due to the reflections in a Fabry-Perot cavity are shown in the inset.

As can be seen in Fig. 5.10(a), the zero-bias responsivity for the one-stage detector from S#3-1 increased with temperature up to 200 K, while the four- and six-stage ICIPs from S#3-4 and S#4-4 increased up to 250 K. These increases suggest the reduction of diffusion length with increasing temperature and clearly demonstrate the advantage of multiple-stage ICIPs over one-stage detectors for higher temperature operation. This advantage can also be seen from their response spectra at high temperatures. For example, the response spectrum of the one-stage device from S#3-1 was relatively noisy at 250 K, while the response spectra from multiple-stage ICIPs were still fairly clean. Additionally, as shown in insets to Fig. 5.12(a) for devices from S#3-1 and S#3-4, the conventional one-stage detector was more sensitive to bias voltage at high temperatures, while ICIPs were bias independent for the four- and six-stage devices up to 250 K. This indicates an effective collection of photo-generated carriers for ICIPs under zero-bias for a wide range of temperatures. In contrast, the one-stage detector with a thick absorber required a particular bias voltage to facilitate the collection of photo-generated carriers because the diffusion length was shorter than the absorber thickness. Furthermore, the responsivities of eight-stage detectors from S#3-8 and S#4-8 increased with temperature up to 280 K and again they are bias independent, which is related to the still shorter absorber thickness in each stage compared to that in four- and six-stage detectors. This is because eight-stage ICIPs with relatively short absorbers can afford more reduction of diffusion length with increased temperature. Because the total absorber thickness for the six- and eight-stage devices is equal, comparing their device performance is instructive. In terms of D^* at wavelengths near 7-8 µm (see Table 5.2 and Figs. 5.10(b) and 5.13), the six-stage device is slightly better at 200 K, while the eight-stage device is better at 300 K. This can also be seen from the response spectra, which are substantially less noisy for the eight-stage devices at 300 K, especially with the enhanced electron barrier. Considering that the total absorber thickness for the eight-stage device is less than 2.3 µm, there is still room to add more stages to further suppress noise so as to enhance high-T device performance. These results clearly demonstrate the benefits of using multiple-stage ICIPs for high temperature operation in the long wavelength infrared region.

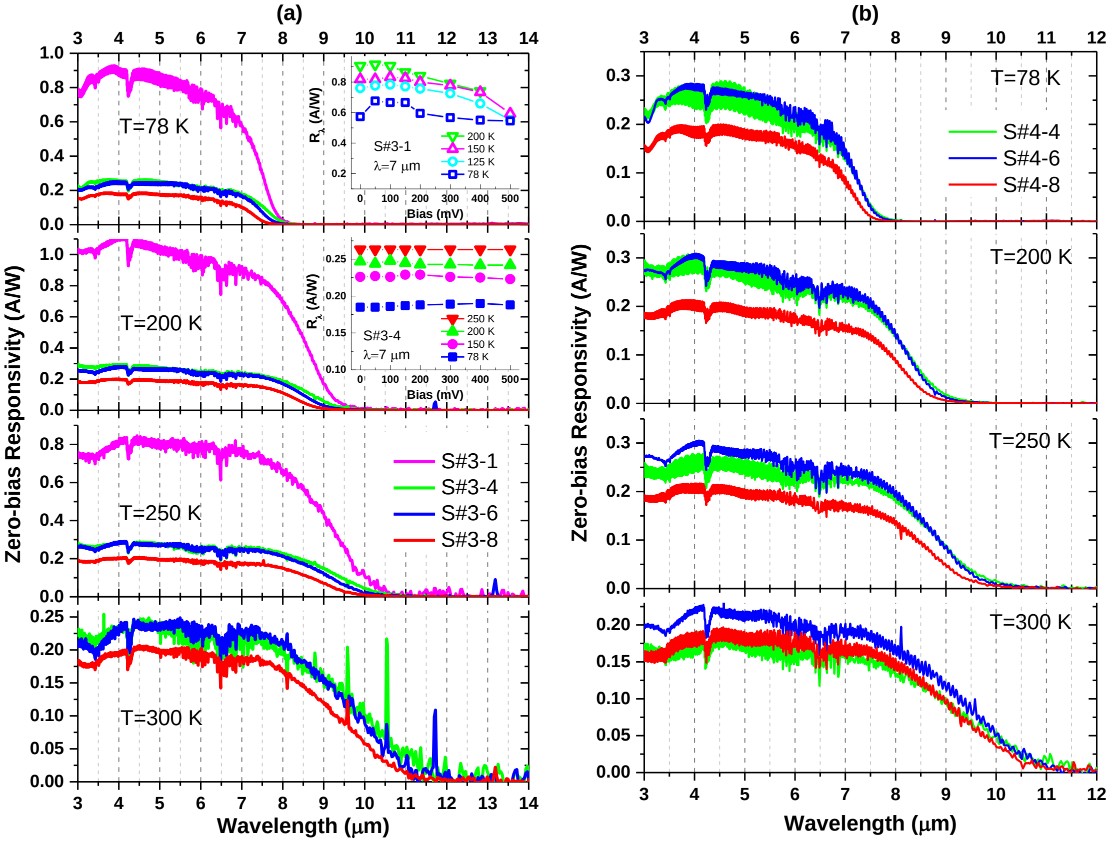

Figure 5.12: (a) Zero-bias responsivity for detectors from wafers S#3-1, S#3-4, S#3-6 and S#3-8 in set #3 and (b) detectors from wafers S#4-4, S#4-6 and S#4-8 in set #4. Insets: responsivity at 7 μm *vs*. bias voltage for detectors from wafers S#3-1 and S#3-4.

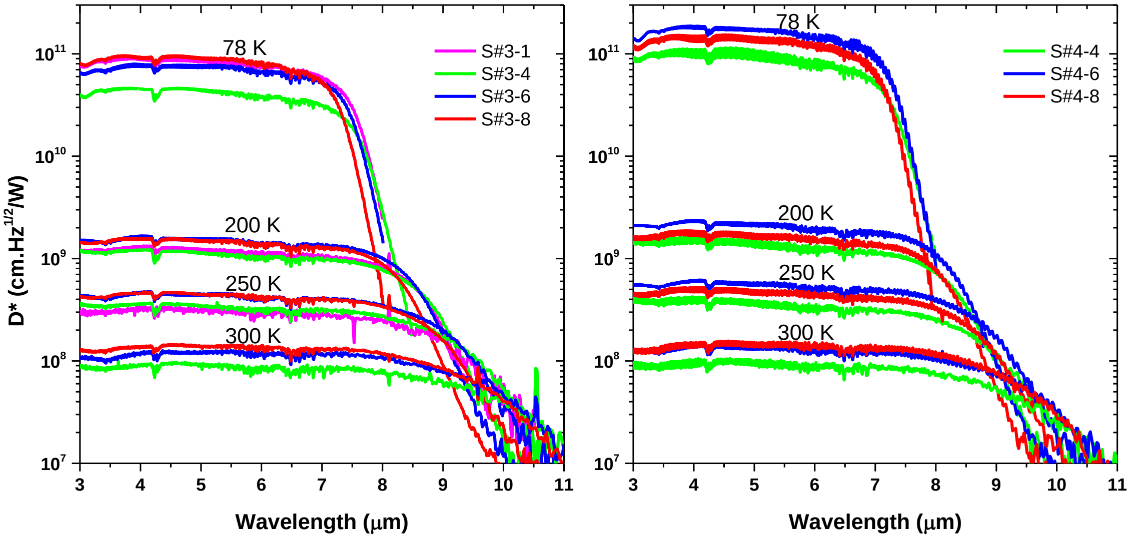

Figure 5.13: Zero-bias D^* *vs*. wavelength at different temperatures for the detectors from sets #3 and #4.

5.3.4 High temperature (>300 K) operation

While the one-stage detectors are incapable of operating at temperatures higher than 250 K, the four-stage ICIPs from sets #3 and #4 and the six-stage ICIPs from S#3-6 could operate up to 320 K, and the six-stage ICIPs from wafer S#4-6 and the eight-stage ICIPs from both sets #3 and #4 could operate up to 340 K. Their responsivities at these high temperatures are shown in Fig. 5.14. At high temperatures, because the device resistance is relatively low (*e.g.*, <30 Ω), the series resistance (5-7 Ω) from contact and external wire connections could have a significant influence on the accuracy of extracted intrinsic photocurrent. Hence, there may be some uncertainties in their responsivities at high temperatures. Nevertheless, the obtained relative photo-response spectra reflect how well these ICIPs can perform at temperatures above 300 K. Since Johnson noise is the dominant noise source at high temperature when detectors operate under zero-bias, it is critical to reduce this noise in order to achieve high temperature operation. As can be seen from Figs. 5.12 and 5.14, the photo-response spectra of ICIPs with eight stages were less noisy, especially with the enhanced electron barrier from set #4, compared to other devices with fewer cascade stages and without the enhanced electron barrier. Again this validates the importance of the multi-stage ICIP architecture for suppressing the noise at high temperatures.

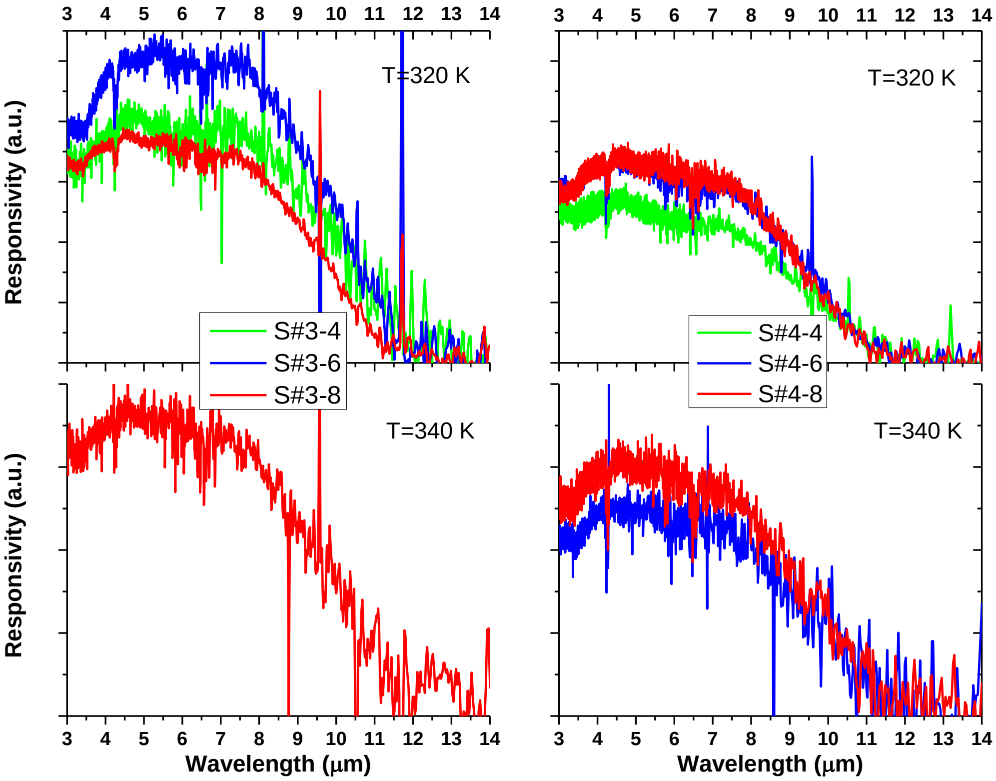

Figure 5.14: Zero-bias responsivity for detectors from sets #3 and #4 at 320 and 340 K.

5.4 Concluding remarks

LWIR ICIPs are demonstrated to be capable of operating at high temperatures up to 340 K. The advantages of the multi-stage ICIPs, with their discrete absorber architecture, have been clearly demonstrated over the conventional one-stage device by reduced dark current density (*i.e.*, the suppression of noise), higher detectivity (D^*) and higher operating temperature in the LWIR region. Although not yet optimized, the ICIPs could operate at 300 K with a D^* higher than 1.0×10^8 cm·Hz$^{1/2}$/W, which exceeds the reported value for commercial uncooled MCT detectors [1,2]. suggesting great potential for real applications such as laser spectroscopy and free-space communication in combination with room temperature long-wavelength quantum cascade (QC) lasers.

Additionally, negative differential conductances were observed in these detectors at high temperatures and identified as being related to intraband tunneling through the electron barrier. The observed features related to NDCs can be used as a characterization tool in the future to further improve understanding and device optimization of ICIPs. For example, the electron barrier will need to be enhanced further so that NDCs can be minimized or even eliminated for high temperature operation. Considering the complexity of ICIPs and the preliminary phase of their development, there are many parameters and options in the structure and material growth that need to be investigated and optimized, which will be challenging and time intensive. On the other hand, these parameters and options also provide remarkable room for significant improvements in device performance. Therefore, it is expected that the continuing development of ICIPs will lead to real products for many applications in addition to the generation of cutting-edge knowledge in quantum engineered semiconductor structures and devices. Considering the increased availability and popularity of room temperature QC lasers, the number of applications and the demand for uncooled long wavelength ICIPs should grow in the future.

Chapter 6 Non-current-matched long wavelength interband cascade infrared photodetectors

6.1 Background and motivation

ICIPs have been investigated by several groups for their advantages of high-operating-temperature (HOT) and high-speed operation with low dark current densities, especially for high HOT detectors in the LWIR region. As discussed in chapter 5, ICIPs had been demonstrated to be capable of operate above room temperature in LWIR band. Even showing a promising potential for high performance of the LWIR ICIPs (with $D^*\geq 1.0\times 10^8$ cm·Hz$^{1/2}$/W at 300K), there's still plenty of room of improvement before touching the limit.

In contrast to an IC laser where each injected electron generates multiple photons, the process is reversed in an ICIP. Each additional electron in the external circuit requires absorption of multiple photons for detector operation. In other words, the maximum responsivity (and external quantum efficiency, η_{max}) in an ICIP is reduced by the thin individual absorbers and multi-stage architecture. However, the suppression of noise compensates for the reduced responsivity. This has been discussed in previous theories from the perspective of shot noise gain [14] and at a fundamental level [83], as well as from equivalent circuit consideration of Johnson noise [99]. Hence, the signal to noise ratio (*i.e*. detectivity D^*) in ICIPs is not reduced, but instead proportional to the square root of the number of cascade stages (N_C) for a first-order approximation [14,99]; and thus enhanced compared to the conventional single-absorber detector [83]. Another aspect that should be made clear is that the *maximum* responsivity (and *maximum* external quantum efficiency η_{max}, equal to $1/N_C$) is not necessarily the actual responsivity (and η) of an ICIP. In this early phase of development, because the total absorber thickness is not long enough to absorb all the incident photons, an ICIP is usually designed and operated with a responsivity (and η) below the maximum value and its responsivity is determined by individual absorber thicknesses, instead of N_C. For current-matched ICIPs [83] where the number of photo-generated carriers is equal in every stage, ideally, the photo-current (and responsivity) is a constant that can be determined by the absorber thickness in the first stage, and is independent of N_C. For a thicker absorber, the responsivity is higher. For non-current-matched ICIPs with identical absorbers in every cascade stage, theoretically, the responsivity is not only determined by the absorber thickness in the first stage, but also by the travel distance of incident light, which is related to N_C because of light intensity attenuation during propagation. Consequently, one should expect that the responsivity in the non-current-matched ICIP with identical absorbers is reduced compared to that in the current-matched ICIP with a first absorber that is equal thickness. This has been partially shown in a non-current matched MWIR ICIP mentioned in chapter 3. However, only a single device is not as convincing apart from its material issue, so more experimental work is required to verify this.

Compared to conventional detector structures with a single absorber, ICIPs are more flexible, with multiple degrees of freedom for the optimization of device performance. However, this flexibility certainly adds more complexity and requires better understanding of many factors and their interplay in order to optimize device performance. For example, there are tradeoffs depending on whether photocurrent in

ICIPs is designed to be matched between stages. In the current-matched ICIPs [64,65,88-90], the absorbers in optically deeper stages are made thicker to achieve an equal photocurrent among all stages with maximized utilization of absorbed photons for optimal responsivity. This requires knowing material absorption coefficients with good accuracy, which may vary with temperature, and increases difficulties in implementation at different operating temperatures. By comparison, individual absorbers are designed to be identical with equal thickness in a non-current-matched ICIP [14,15,62,63,86,87]. They are simpler to implement, but have the possible drawback of a substantial reduction in responsivity due to light attenuation, especially with relatively thick absorbers [14,83].

Although current-matched and non-current-matched ICIPs have been explored independently, they have not been investigated together in the same framework until this work. To identify and understand their specific features and differences in device performance, a comparative study of the electrical and optical properties of a group of ICIPs with both absorber designs was presented. Electrical gains significantly exceeding unity were observed from non-current-matched ICIPs. This high gain was also observed in our MWIR ICIPs with non-current matching structure, as discussed in chapter 3. However, due to the material issues, the analysis based on that sample is not that solid. Therefore, in this chapter, several LWIR ICIPs were grown with both current-matched and non-current matched starches to carry on a compassion study to further investigate the ICIPs.

6.2 Device structure and growth

Two sets of ICIP structures were designed to target the LWIR region with a reverse illumination configuration [65,90]. The structures in each set have different numbers of stages and variations of individual absorber thicknesses, but have identical electron and hole barriers and the same InAs/GaSb SL absorber composition. There are two thin InSb interfaces [70,90]between the InAs and GaSb layers in each SL period (60 Å) in every absorber that is *p*-type doped at 2.6×10^{16} cm^{-3}. Set #1 consists of two current-matched ICIP structures in set #4, which areS#4-8 and S#4-12 with eight and twelve cascade stages, where S#4-8 had been discussed in chapter 5. S#4-12 is composed of 12 stages with absorber thicknesses of 180, 192, 210, 228, 246, 264, 282, 306, 336, 366, 396, and 432 nm, in order from the surface to the substrate (the direction of light illumination). Set #7(NM.) has five non-current-matched ICIP structures, S#7(NM.)-16, S#7(NM.)-20, S#7(NM.)-15, S#7(NM.)-23, and S#7(NM.)-28, with sixteen, twenty, fifteen, twenty-three and twenty-eight cascade stages, respectively. S#7(NM.)-16 has 16 discrete identical stages with each absorber thickness (222 nm) equal to that of the first absorber of S#4-8. S#7(NM.)-20, S#7(NM.)-15 and S#7(NM.)-23 has 20, 15, and 23 discrete identical stages with each absorber thickness (180 nm) equal to that of the first absorber of S#4-12. S#7(NM.)-28 has 28 discrete identical stages with each absorber thickness of 150 nm. More details about the structure parameters with device characteristics are provided in Table 6.1

The growth and device fabrication follow the same process as described in section 3.2. However, during the growth for the wafers S#7(NM.)-15, S#7(NM.)-23, and S#7(NM.)-28, the doping level (3×10^{18} cm^{-3}) of the InAs contact layer was relatively higher to the designed level (1×10^{18} cm^{-3}) for our typical ICIP structure. Besides, the 10-nm GaSb layer right above buffer layer was *p*-doped to 2.6×10^{16} cm^{-3}, which is undoped in the design. Additionally, the hole barrier was incorrectly doped as 6.6×10^{16} cm^{-3}, nearly three-fold of the designed value (2.3×10^{16} cm^{-3}). These errors may cause certain issues to the device performance as will be discussed below.

6.3 Device characterization and discussions

Electrical and optical properties of devices from these wafers were determined through measurements of dark current density-voltage (J_d-V) characteristics and photo-response spectra. Table 6.1 summarizes some key material properties including cutoff wavelength λ_c, bandgap E_g and activation energy E_a extracted from measurement, along with design parameters. At 300K, S#7(NM.)-20 has a shorter cutoff wavelength (9.5 µm) compared to the other wafers (10.6-11.1 µm)

Table 6.1: Summary of material and design parameters for the seven devices.

Device	First absorber thickness (nm)	# of stages	Total absorber thickness (µm)	100% λ_c (µm) at 300K	E_g (meV) at 0 K	E_a (meV) 78-125 K	E_a (meV) 150-250 K
S#4-8	222	8	2.29	11.0	175	45	155
S#4-12	180	12	3.44	11.0	174	45	155
S#7(NM.)-16	222	16	2.29	11.1	172	64	160
S#7(NM.)-20	180	20	3.60	9.5	188	43	160
S#7(NM.)-15	180	15	2.70	10.6	180	21	132
S#7(NM.)-23	180	23	4.14	10.6	180	23	132
S#7(NM.)-28	150	28	4.2	10.6	180	11	102

6.3.1 Electrical properties

From the measured J_d-V curves, the zero-bias resistance-area products (R_0A) were extracted as shown in Fig. 6.1 for the seven representative devices at a wide temperature (T) range, which allows us to determine the activation energies. As shown in Fig. 6.1 and Table 6.1, the carrier transport in these devices at low temperatures (<150 K) is dominated by the tunneling. While at high temperatures (>150 K), it is diffusion limited for S#4-8, S#4-12 S#7(NM.)-16, and S#7(NM.)-20 with activation energies nearly equal to their zero-temperature bandgaps. However, devices from the other three wafers S#7(NM.)-15, S#7(NM.)-23, and S#7(NM.)-28, both diffusion and generation-recombination processes are presented for carrier transport with activation energies between half and one bandgap. The relative low activation energies in these three wafers may be associated with the unperfect growth.

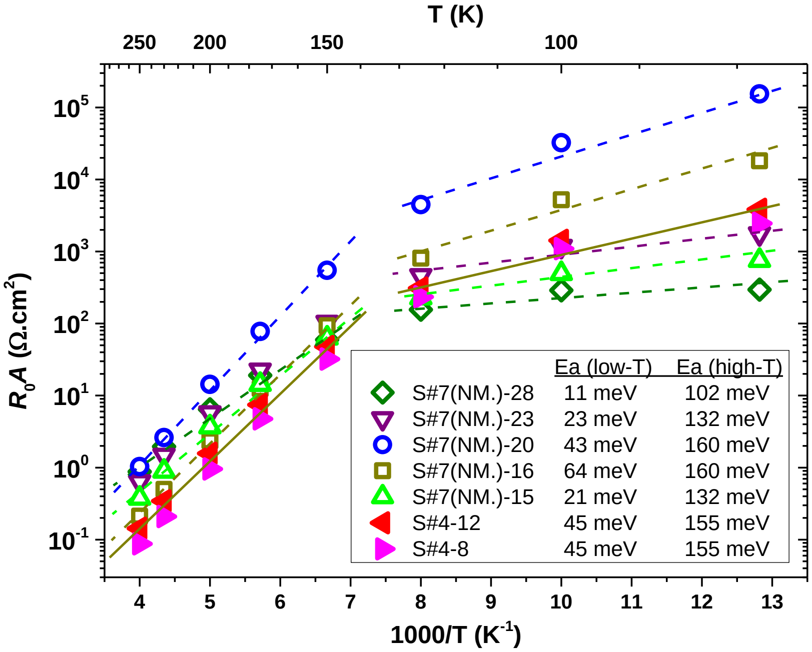

Figure 6.1: Extracted R_0A of the seven representative devices from each wafer at various temperatures.

6.3.2 Optical Characteristics

6.3.2.1 Responsivity

The optical response of the ICIPs was collected using an IR global source within an FTIR spectrometer and calibrated using a 600 K blackbody source (aperture diameter of 0.762 cm) with a 2π field of view (FOV). Because of efficient carrier transport in ICIPs with relatively thin individual absorbers, the photo-current is insensitive to bias voltage. Figure 6.2 shows the zero-bias responsivity (R_i) spectra of the seven representative devices at a temperature from 78 to 300 K. It is evident that current-matched ICIPs have higher responsivities than non-current-matched ICIPs at all temperatures. When comparing them with the same absorber thickness (180 or 222 nm) in the first stage, the responsivity of the non-current-matched ICIP was about 50-60% of that obtained from corresponding current-matched ICIPs. This is exemplified in Table 6.2, where the value of R_i was taken at 7 µm, except for S#7(NM.)-20 of which is taken at 5 µm because its cutoff wavelength is about 2 µm shorter than other three ICIPs. These data demonstrate the necessity of current-matching for optimal responsivity, and substantial attenuation of light intensity in the optically deeper stages related to individual absorber thicknesses. This can be further examined and illustrated by looking at the temperature dependence of responsivity, as shown in Fig. 6.3.

Table 6.2: Experimentally obtained ratio of responsivity for ICIPs at different temperatures.

T (K)	200	250	280	300	320
$\frac{R_i(S\#7(NM.)-16)}{R_i(S\#4-8)}$	0.63	0.61	0.62	0.59	0.57
$\frac{R_i(S\#7(NM.)-15)}{R_i(S\#4-12)}$	0.62	0.65	0.67	0.62	0.64
$\frac{R_i(S\#7(NM.)-23)}{R_i(S\#4-12)}$	0.47	0.50	0.52	0.51	0.51
$\frac{R_i(S\#7(NM.)-20)}{R_i(S\#4-12)}$	0.66	0.61	0.62	0.59	0.57

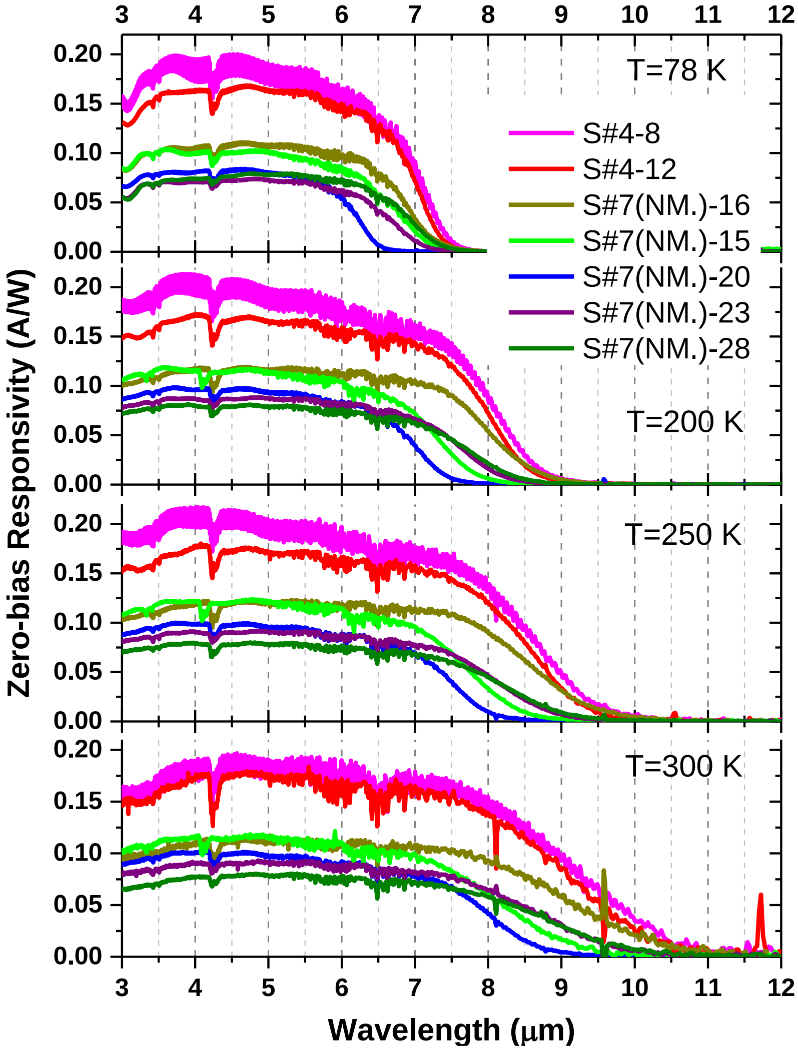

Figure 6.2: Zero-bias responsivity spectra for the four devices at different temperatures.

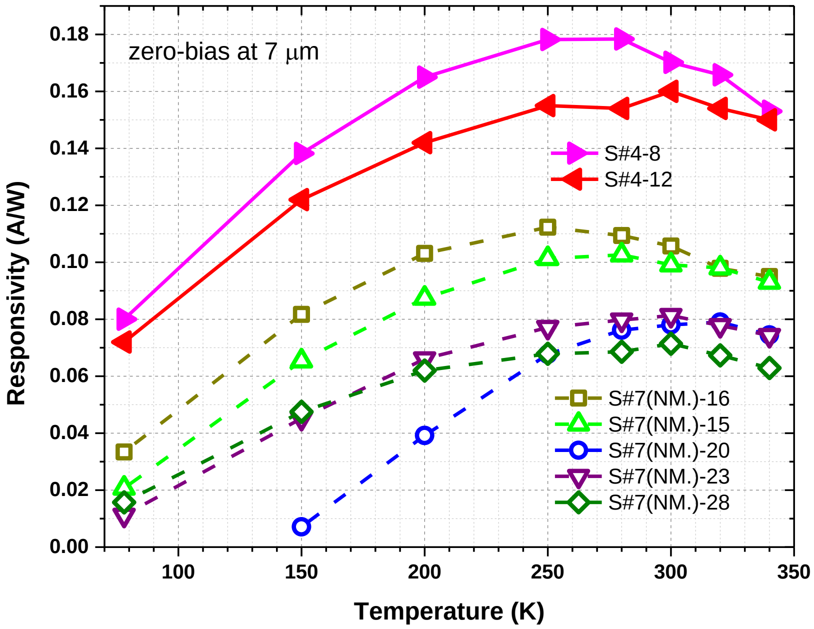

Figure 6.3: Temperature-dependent responsivity of the four devices at 7 μm.

As can be seen from Fig. 6.3, the responsivities of the seven devices exhibited similar trends with increasing temperature as they peaked at certain temperatures and then decreased. This was related to variations of diffusion length, absorption coefficient, and current-matching with temperature. As reported for ICIPs [94], the diffusion length (>500 nm at 300 K) is likely longer than or comparable to individual absorber thicknesses over the entire temperature range of interest, and consequently the collection of photo-generated carriers would not be affected much in these ICIPs at various temperatures. Hence, the temperature dependence of R_i was mainly caused by the increase of absorption coefficient due to bandgap narrowing with raising temperatures and the accompanying change in current-matching. In other words, R_i initially increased with enhanced absorption when the temperature was raised, and then decreased when the more considerable attenuation in the optically deeper stages (due to stronger absorption in optically shallower stages) began to affect the current-matching.

This is more significant for devices with relatively thick absorbers. For example, because the absorber in the first stage for S#4-8 and S#7(NM.)-16 is thicker (222 nm) than that (180 nm) for S#4-12, S#7(NM.)-15 and S#7(NM.)-23, their responsivities peaked at lower temperatures (250 K) compared to the peak locations (300, 280 and 300 K) for S#4-12, S#7(NM.)-15 and S#7(NM.)-23. Again, this demonstrates the existence of substantial light attenuation and the requirement of current-matching in achieving optimal responsivity. Since the cutoff wavelength of S#7(NM.)-20 approached 7 µm at low temperatures, which was substantially shorter than that for the other three wafers, the light absorption (and attenuation) was small at this wavelength. This produced the relatively fast increase of the corresponding R_i with temperature up to 280 K and the peak at 320 K (Fig. 6.3).

6.3.2.2 Electrical gain

To make a further quantitative assessment of current-matched and noncurrent-matched ICIPs, the absorption coefficients (α) for the SL absorbers at room temperature were obtained through the direct transmission measurement shown in Fig. 6.4. Based on the measured absorption coefficient, the estimated R_i is significantly smaller than the values in Fig. 6.2 for non-current-matched ICIPs, implying possible electrical gain (G) exceeding unity. For the current-matched and non-current-matched identical absorber ICIPs, the responsivities can be expressed similar to Eqs. 3.2 and 3.3 as:

$$R_i(\lambda)\frac{1.24}{\lambda} = (1-R)(1-e^{-\alpha d})G\,, \tag{6.1}$$

$$R_i(\lambda)\frac{1.24}{\lambda} = (1-R)e^{-(N_c-1)\alpha d}(1-e^{-\alpha d})G\,, \tag{6.2}$$

where *R* is the reflectance at the device's top surface taken to be 0.31 for an InAs cap layer, N_c is the number of cascade stages and *d* is the absorber thickness of the first stage. According to Eqs. 6.1 and 6.2, the electrical gain can be extracted from experimentally measured absorption coefficients and responsivities for all devices. Only the first stage was considered with Eq. 6.1 for the current matched ICIPs because of a designed equal photocurrent in every stage. All cascade stages were considered with Eq. 6.2 for ICIPs with identical absorbers because the photocurrent is the smallest in the last stage due to the largest attenuation of light intensity.

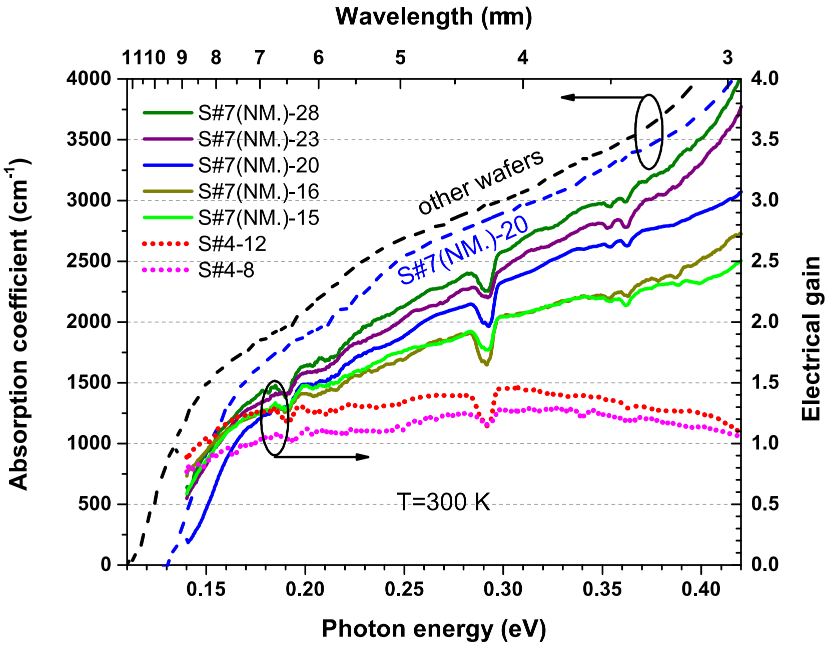

Figure 6.4: Absorption coefficient and electrical gain at room temperature. The dips near 4.2 µm in the gain curves were due to CO_2 absorption in the response spectra.

The estimated electrical gain at room temperature is plotted in Fig. 6.4 for the four devices. When the absorption coefficient is higher than a certain value (e.g. >1000 cm^{-1}), the electrical gain for the ICIPs exceeds the unity. With the further increase of absorption coefficient at the higher photon energies, *G* increases for identical absorber ICIPs, but remains nearly constant in the current-matched ICIPs. The enhanced absorption at a large photon energy significantly attenuates the light intensity in the last stage, which then requires a large electrical gain to maintain current continuity. At the first stage, the increase of electrical gain is not needed because the photocurrent is the highest among all the stages. To maintain the current continuity, the electrical gain is required to be higher in ICIPs with thinner absorbers to compensate for a shorter absorption length. This can be seen in Fig. 6.4, where G is higher in S#4-12 compared to S#4-8, while G is higher in S#7(NM.)-23 than S#7(NM.)-15 and S#7(NM.)-16 when the photon energy is higher than 0.2 eV. It should be noted that the value of G could vary significantly in different cascade stages with substantial light attenuation, as G increases with more number of cascade stages.

Gain exceeding unity was also observed in T2SL detectors (>5) [61] and in our previous MW ICIPs discussed in chapters 3 and 4 [92,95], although the mechanism is not fully understood. One mechanism for ICIPs, implied in Ref. [83], arises from the distribution of bias voltage or electrical potential across individual cascade stages during device operation. For a multi-stage ICIP under illumination at zero bias, the electrical potential across each individual stage will self-adjust to achieve equal current through each stage. If the number of photo-generated carriers is not equal in every stage, the electrical potential across each stage would also not be equal. The requirement of current continuity forces the stage with the largest amount of photo-generated carriers (typically the first stage in a non-current-matched ICIP with identical absorbers) to be slightly forward biased such that a forward injection current will partially offset the photocurrent. Hence, the responsivity in a non-current-matched ICIP is smaller than that in a current-matched ICIP, as observed in this work.

Consequently, other stages with smaller amounts of photo-generated carriers will necessarily be under reverse bias to make the total bias voltage across all stages zero. The reverse bias will add a thermal generation current in those stages along the same direction as the photocurrent, resulting in an effective increase of the photocurrent. When the thermal generation current is higher than or comparable to the photocurrent (which is possible at high temperatures), the stages under a reverse-bias voltage could have a significant electrical gain as observed in the non-current-matched ICIPs. Of course, this mechanism cannot explain the gain observed in one-stage devices [61,92,95] as presented in the chapters 3 and 4, where a photoconductive gain was postulated to be coexisted in these thin absorber ICIPs with a possible longer carrier lifetime than transit time. This may explain the slightly lager electrical gain than unity existed in the first stage of the current-matched ICIPs.

Due to light attenuation, the photocurrent generated in each cascade stage is different and the photo-generated current deceases with optically deeper stages. When the absorbers are thin enough to ensure a small αd, the deceasing of photo-generated current will follow a liner trend with the increasing order of stages. Therefore, in order to maintain current continuity, the output current will approach the value of the photo-generated current in the middle cascade stage among all the stages. According to a recent theory, the output current is the average of the photo-generated current from every stage. The electrical gain in each stage follows the same trend as the photo-generated current, the electrical gain in No. n stage with gain, G_n, can be described as:

$$R_i(\lambda)\frac{1.24}{\lambda}=(1-R)e^{-(n-1)\alpha d}(1-e^{-\alpha d})G_n, \tag{6.3}$$

When n=N_C/2, the electrical gain in the middle cascade stage can be estimated as shown in Fig. 6.5. The electrical gain in the middle cascade stage of the non-current matched ICIPs present very comparable values to that in the first stage of current-matched ICIPs, which dose support the assumption to some extent. Therefore, a maximum value of D^* can be achieved by varying the absorber thickness (d) and number of cascaded stages (N_C) based on the absorption coefficient (α) of interest:

$$D^*=\frac{R_i}{\sqrt{\frac{4k_BT}{R_0A}}}\propto I_{ph}\sqrt{R_0}\propto\int_0^{\lambda_c}e^{-\alpha(\lambda)(\frac{N_C}{2}-1)d}\left(1-e^{-\alpha(\lambda)d}\right)P_{inc}(\lambda)d\lambda\sqrt{\frac{N_C}{d}}, \tag{6.4}$$

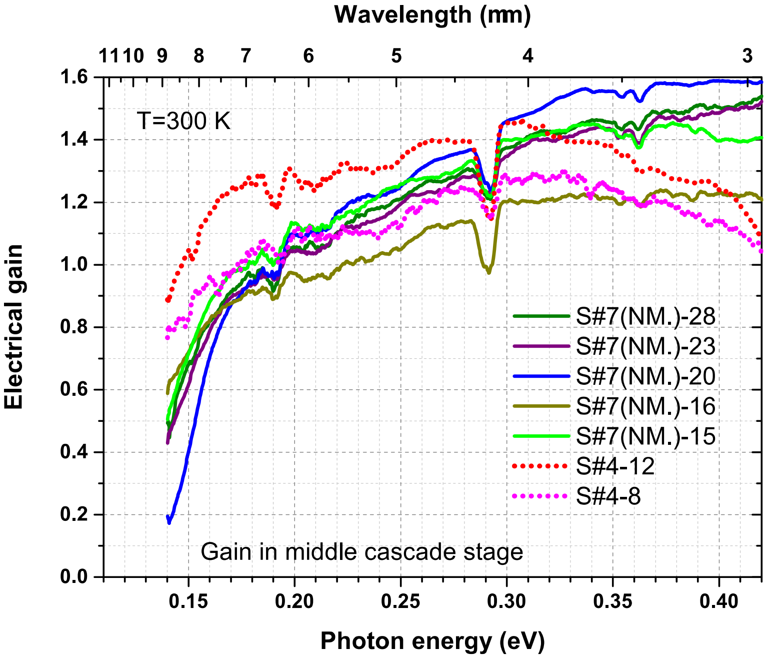

Figure 6.5: Electrical gain in the middle cascade stage of the non-currented ICIPs at room temperature. They exhibited comparable electrical gain to that in current matched ICIPs.

Overall, an electrical gain can be produced to partially offset the light attenuation in an optically deeper stage. As such, the responsivity in a non-current-matched ICIP would be appreciable although it is not maximal as in the current-matched ICIP. Considering the significantly higher R_0A (Fig. 6.1) and suppressed noise as shown in cleaner response spectra (Fig. 6.2), non-current-matched ICIPs with identical absorbers in every stage may achieve device performance comparable to current-matched ICIPs in terms of detectivity (D^*). Also, due to possible electrical gain, perfect current-matching is not necessary in ICIPs, which provides great flexibility in design and device implementation.

6.3.2.3 Detectivity

Based on the measured R_0A and responsivity, the estimated Johnson-noise limited detectivity under zero-bias for each device is shown in Fig. 6.6. The advantage offered by noncurrent-matched ICIPs with more-stages can be seen from the maximum value of D^* for S#7(NM.)-28, regardless of S#7(NM.)-20 with a shorter cutoff wavelength. For instance, at 250K, the Johnson-noise-limited D^* (λ=7 µm with a FOV of 2π) were 4.1×10^8, 5.1×10^8, 5.0×10^8, 4.5×10^8, 6.0×10^8, 5.3×10^8, and 8.2×10^8 cm·Hz$^{1/2}$/W for S#4-8, S#4-12, S#7(NM.)-15, S#7(NM.)-16, S#7(NM.)-20, S#7(NM.)-23 and S#7(NM.)-28, respectively. At higher temperatures, such as 300K, the corresponding Johnson-noise limited D^* became 1.4×10^8 (S#4-8), 1.8×10^8 (S#4-12), 1.6×10^8 (S#7(NM.)-15), 1.5×10^8 (S#7(NM.)-16), 2.4×10^8 (S#7(NM.)-20), 1.8×10^8 (S#7(NM.)-23), and 1.9×10^8 (S#7(NM.)-28) cm·Hz$^{1/2}$/W, which significantly exceeds the reported value (*e.g.* $\geq 4.0\times10^7$ Jones with a FOV between π/2 and 2π) for commercial uncooled MCT detectors [1,2]. The substantially higher D^* for S#7(NM.)-20 was due partially to the relatively short cutoff wavelength compared to the other ICIPs. Nevertheless, with a similar cutoff wavelength, D^* is slightly higher in the ICIP made from wafers S#7(NM.)-16 compared to S#4-8 with the same first absorber thickness, even though R_i is lower in S#7(NM.)-16. Hence, in terms of device detectivity, non-current-matched ICIPs with appropriate construction can have comparable or even better performance over current-matched ICIPs. In fact, the performance of non-current-matched ICIPs can be further improved. When the stages of an ICIP are made identical, there is a tradeoff between reduced signal and suppression of noise as the number of stages increases. Adding further stages to an identical-absorber ICIP can reduce the thermal noise, but also compromises the overall signal current, due to light attenuation in the optically deeper stages. Hence, an optimized number of cascade stages may exist for achieving a maximum value of D^* based on the absorption coefficient and absorber thickness [83].

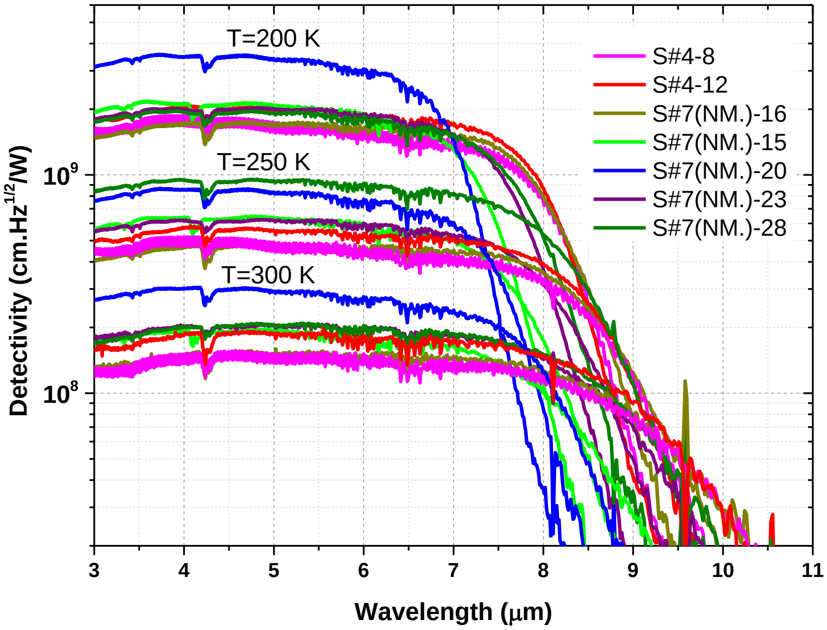

Figure 6.6: Johnson-noise limited D^* spectra of the seven devices at various temperatures.

6.4 Summary and concluding remarks

Through comparative investigation of two sets of LW ICIPs with both current-matched and non-current-matched configurations in the same framework, the necessity of current-matching is demonstrated to maximize utilization of absorbed photons for optimal responsivity and the correlation of reduced responsivity with light attenuation in the optically deeper stages for non-current-matched ICIPs. Electrical gain exceeding unity is observed, which is more significant in the last stage of non-current-matched ICIPs for reaching photocurrent continuity. The significant electrical gain enabled an appreciable responsivity in non-current-matched ICIPs, although still lower than in current-matched ICIPs. This, in combination with the large R_0A in non-current-matched ICIPs, resulted in Johnson-noise limited detectivities (>1.5×10^8 cm·Hz$^{1/2}$/W at 300 K) comparable to or even higher than in current-matched ICIPs. Further understanding of the electrical gain and optimization should lead to better structure design and higher device performance. Because of the ease of design and implementation, as well as improved coupling with an external circuit, non-current-matched ICIPs with identical absorber configuration are promising to meet many applications at room temperature in the LWIR spectrum.

Chapter 7 Resonant tunneling and multiple negative differential conductance in long wavelength interband cascade infrared photodetectors

7.1 Background and motivation

Negative differential conductance (NDC) has been extensively studied in double barrier QW heterostructures [179-183], superlattices [176,184], and quantum cascade lasers [185,186]. In these semiconductor quantum structures, NDC is attributed to the resonant tunneling of electrons through quantized energy levels in the conduction band that lead to a peak in the current-voltage curves. Additionally, NDC can be caused by resonant interband tunneling of carriers through quantized states in both the conduction and valence bands [187-192], resulting in high peak-current densities and large peak-to-valley current ratios. All of the above mentioned NDC features and the associated peaks in current share a common feature; they become weak (or even disappear) with increasing temperature. In contrast, the NDC features and their associated current peaks recently observed in LW ICIP structures [90] exhibit the opposite temperature dependence; they become more significant with increasing temperature. However, this temperature dependence of NDC features was not observed in our MW ICIPs. By examining current-voltage characteristics of LW ICIPs that have different electron barriers, as discussed in chapter 5, it is initially identified that intraband tunneling of minority electrons was responsible for NDC features in those LW ICIPs. Because of the totally different temperature dependence from most of the previous resonant tunneling structures, and the complexity and involvement of both conduction and valence bands in ICIP structures, further investigation was need to understand how other factors, such as doping concentration and the hole barrier, affect the current-voltage characteristics, as well as influence device performance.

This chapter presents a comprehensive description of how multiple peaks in current-voltage characteristics and their associated NDC features are formed in ICIPs, including a study of how structural parameters and doping concentration can affect these features and device performance.

7.2 Device design and growth

Five sets of ICIP structures (15 in total) were designed based on InAs/GaSb SL absorbers with room temperature cutoff wavelengths (λ_c) targeted in the LW region (8-12 µm). These ICIP structures were grown using a Veeco GENxplor molecular beam epitaxy chamber on nominally undoped *p*-type GaSb (001) substrates. As shown schematically in the simplified band diagram in Fig. 2.5, in each stage of an ICIP, the absorber (zone 1) is sandwiched by two wider band gap zones (2 and 3) that serve as a hole barrier (hB) and an electron barrier (eB), respectively. The eB and hB are composed of digitally graded multiple GaSb/AlSb and InAs/AlSb QWs, respectively. The period of the InAs/GaSb SL absorber was designed to be 60 Å with two InSb-like interfaces [70] between the InAs and GaSb layers. In a SL period, the InAs/GaSb layers are 31/24.7 Å for wafer S#3-4, and are 31/25.2 Å for all other wafers. The numbers of SL periods in individual absorbers for these ICIPs and other parameters are provided in Table 7.1. The eBs in set #3 have three QWs with GaSb well widths of 33/43/58 Å, while the eBs in sets #4, 5, 6 and 7 are enhanced with an additional 73-Å-wide QW. The hB is made of seven digitally graded InAs/AlSb QWs with InAs well thicknesses of 48/50/52/55/58/62/70 Å in sets #3, 4, 5 and 7, and of 48/50/53/57/62/69/78 Å in wafer S#6-8. The *p*-type doping concentration in the absorbers is 2.6×10^{16} cm^{-3} for the wafers in sets #3, 4, 6 and 7, and 5.3×10^{16} cm^{-3} for the wafers in set #5. The ICIPs in sets #3 through 6 were designed to be photocurrent matched with varied absorber thicknesses. The five ICIPs in set #7 were designed to have an equal absorber thickness in each stage, as discussed in chapter 6. Sets #3, 4 and 7 has been discussed in chapters 5 and 6, and are included here for comparison and completeness. Pieces from each wafer were processed into square mesa detectors with the method describe in section 3.2.

Table 7.1: Summary of ICIP design parameters and device characterization for each wafer.

Wafer	# of stages N_C	# of SL periods in each absorber listed by stage order …	Total absorber thickness (μm)	Doping in the absorber (cm^{-3})	# of QWs in electron barrier	100% λ_c (μm) at 300 K	D^* at 8 μm at 300 K (cm·Hz$^{1/2}$/W)
S#3-4	4	50/55/60/66	1.386	2.6×10^{16}	3	12.0	7.8×10^{7}
S#3-6	6	50/55/60/66/72/79	2.292	2.6×10^{16}	3	11.7	1.1×10^{8}
S#3-8	8	37/39/42/45/48/52/57/62	2.292	2.6×10^{16}	3	11.6	1.2×10^{8}
S#4-4	4	50/55/60/66	1.386	2.6×10^{16}	4	11.5	7.4×10^{7}
S#4-6	6	50/55/60/66/72/79	2.292	2.6×10^{16}	4	11.5	1.0×10^{8}
S#4-8	8	37/39/42/45/48/52/57/62	2.292	2.6×10^{16}	4	11.4	1.2×10^{8}
S#4-12	12	30/32/35/38/41/44/47/51/56/61/66/72	3.438	2.6×10^{16}	4	11.5	1.5×10^{8}
S#5-6	6	50/55/60/66/72/79	2.292	5.3×10^{16}	4	11.5	1.2×10^{8}
S#5-8	8	37/39/42/45/48/52/57/62	2.292	5.3×10^{16}	4	11.0	1.4×10^{8}
S#6-8	8	37/39/42/45/48/52/57/62	2.292	2.6×10^{16}	4	11.0	1.2×10^{8}
S#7-16	16	37×16	3.552	2.6×10^{16}	4	11.5	1.3×10^{8}
S#7-20	20	30×20	3.600	2.6×10^{16}	4	9.6	1.3×10^{8}
S#7-15	15	30×15	2.700	2.6×10^{16}	4	10.6	1.0×10^{8}
S#7-23	23	30×23	4.140	2.6×10^{16}	4	10.6	1.4×10^{8}
S#7-28	28	25×28	4.200	2.6×10^{16}	4	10.6	1.5×10^{8}

7.3 Device performance

All of the ICIPs were operated as detectors at 300 K and above. Table 7.1 provides their 100% cutoff wavelengths at 300 K, which were in the range of 9.6 to 12 µm and agreed well with their design values. Figure 7.1 showed their Johnson noise limited detectivities (D^*) for the detectors from sets # 3, 4, 5 and 6 at 300 K with the 100% cutoff wavelength was around 11.5 µm. The performance for the other detectors have been discussed in chapters 5 and 6. As can be seen from Table 7.1, the detectivities for these ICIPs at 8 µm exceeded 1.0×10^9 and 1.0×10^8 cm·Hz$^{1/2}$/W at 200 and 300 K, respectively.

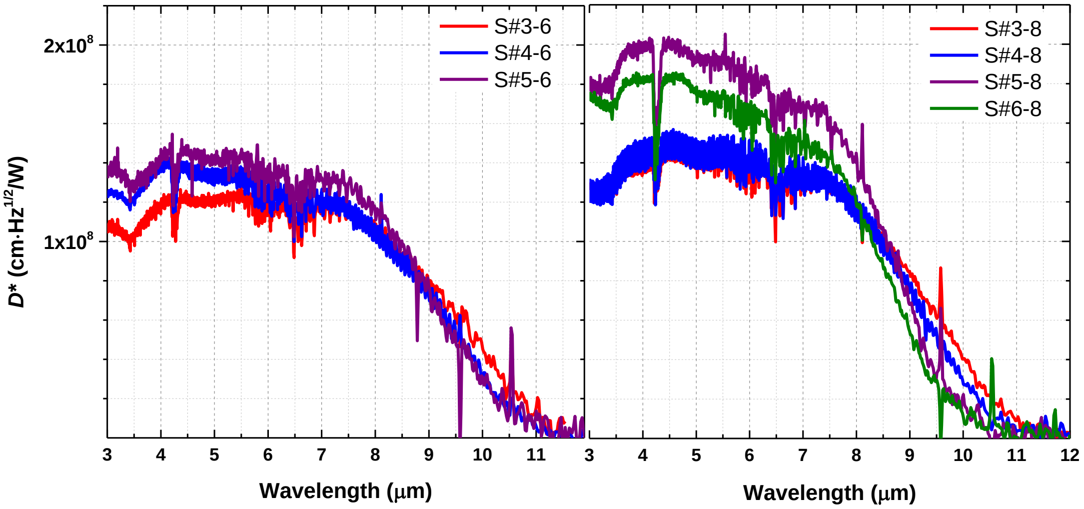

Figure 7.1: Johnson noise limited D^* for six- and eight-stage devices at 300 K.

7.4 Multiple negative differential conductance

The dark current density–voltage (J_d-V) characteristics and differential conductances (G) for devices from all the wafers are shown in Figs. 7.4 and 7.5 at temperatures at and above 280 K. In Fig. 7.4, multiple peaks can be seen in the J_d–V

curves obtained for all the devices under reverse bias voltage and each current peak corresponds to a NDC feature. The number of current peaks (or equivalently NDC features) observed are 4, 6, 8, 12, 15, 16, 20, 23 and 28, and the number observed always corresponds to the number of cascade stages (N_C) in that particular ICIP structure. As expected, the voltage required to observe the entire set of peaks is higher for an ICIP with a larger number of cascade stages. The peaks and NDC become more significant with the increase of temperature (see Fig. 7.5), which is distinctly different from what is observed from other semiconductor quantum structures [176,179-186,188-191]. This distinctive temperature dependence results from the fact that the dominant transport, where the absorbers are *p*-doped, is by minority carriers (electrons) and the electron concentration increases exponentially with raising the temperature. I will come back to this idea when I discuss how the doping concentration in the absorbers affects the current peaks/NDC features. Now, with the identification of the minority carrier transport as responsible for the observed feature, it is time to explain how the peaks/NDC features are produced in ICIPs.

With light illumination or under a reverse bias, the electrons shown in Fig. 7.2 will move from right to left. There are two transport paths for electrons to go through from the absorber in one stage to the next stage. The first is to undergo intraband relaxation in the hB (zone 2) and then interband tunneling to the valence band in the next cascade stage. The other path is to undergo intraband tunneling through the eB to the conduction band in the next cascade stage. The eB is composed of four (or three for set #1) QWs with different GaSb well widths, which increase sequentially from left to right so that the ground state energy decreases from left to right, as shown in Fig. 7.2(a).

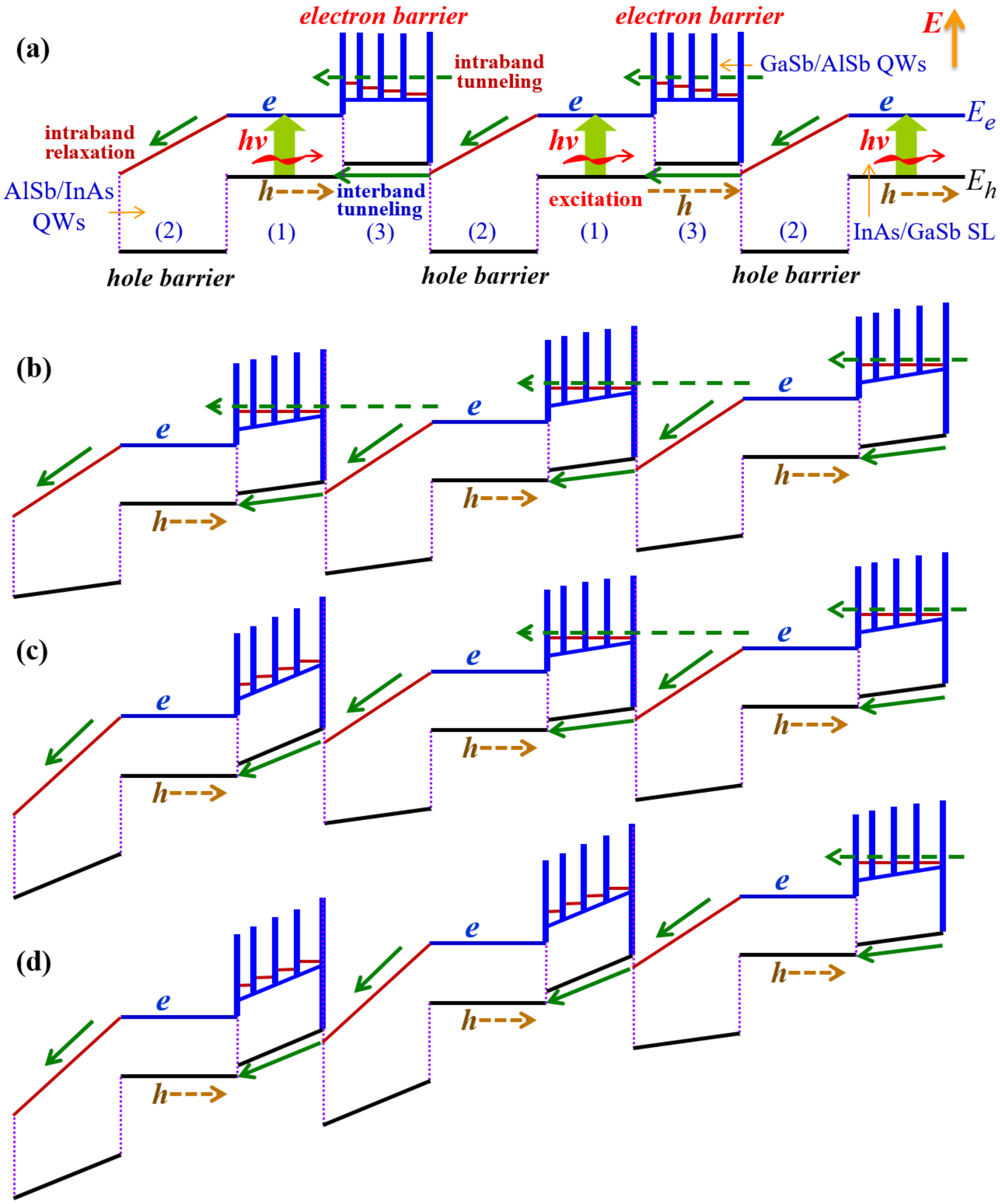

Figure 7.2: (a) Schematic energy band structure of a three-stage ICIP with a reverse illumination configuration under zero-bias. (b) Electrons in the conduction band of the absorbers resonantly tunnel through the eBs under a certain reverse bias. (c) Turn off of resonant tunneling across the eB in the first stage (closest to the anode) with increasing reverse bias, which gives rise to a NDC. (d) Turn off of resonant tunneling across the eB in the second stage with further increasing reverse bias, which produces a second NDC.

Because the ground states in the QWs of the eB are misaligned under zero-bias, the probability of intraband tunneling through the eB is very low and thus the carrier transport is dominated by intraband relaxation and interband tunneling (the first path). Under an appropriate reverse bias, the ground states in the QWs of the eBs become aligned, resulting in resonant intraband tunneling and a substantial increase of current, as shown in Fig. 7.2(b).

Because the charge accumulated in the QWs screens the applied electric field [176,181], a reverse bias makes the field higher near the anode end than the cathode end of the device. Thus, the resonant tunneling condition is initially broken in the eB closest to the anode (left end of Fig. 7.2(c)), resulting in the first NDC feature. When the reverse bias voltage is further increased, the turn-off of resonant tunneling is expanded to the next eB (see Fig. 7.2(d)), resulting in the second NDC feature. In general, with continued increase of the reverse bias voltage, the turn-off of resonant tunneling will sequentially step from the anode to the cathode end of the device. Consequently, the number of current peaks/NDC features should be exactly equal to the number of cascade stages, as confirmed in Figs. 7.4 and 7.5. In some cases, after the turn-off of resonant tunneling between the ground levels of QWs in all eBs, additional reverse bias voltage could align the ground level in the rightmost QW with the energy of excited states in the other QWs in an eB, resulting in another series of NDC features as observed in devices from set #1 discussed in chapter 5.

The appearance of current peaks and NDC features in these ICIPs is similar to that in series-connected multiple double barrier (DB) structures [181,182]. However, the temperature dependences are different due to the different carrier types involved.

Majority carriers are dominant in the transport in previous quantum structures [176,179-186], while minority carriers are dominant in ICIPs. Another difference is that in contrast to symmetric DB structures, the eB in ICIPs is asymmetric to bias polarities. Therefore, the energy levels for the ground state in each QW of the eB will not be aligned under forward bias and thus resonant tunneling was observed in these ICIPs only under a reverse bias. This is also different from the recently reported DB Ga(In)Sb/AlAsSb QW resonant tunneling structures [193], where electrons are majority carriers. It should be mentioned that NDC features are not observed in our MW ICIPs at high temperatures (up to 400 K). The absence of NDC features in MW ICIPs is probably due to their lower minority carrier concentrations and the wider bandgaps required for the MWIR region. On the other hand, in MW ICIPs, under significantly larger reverse-bias voltage at low temperatures, multiple current peaks/NDC features are observed where, again, their number equals the number of cascade stages, N_C [15]. These features are probably caused by the same mechanism discussed here.

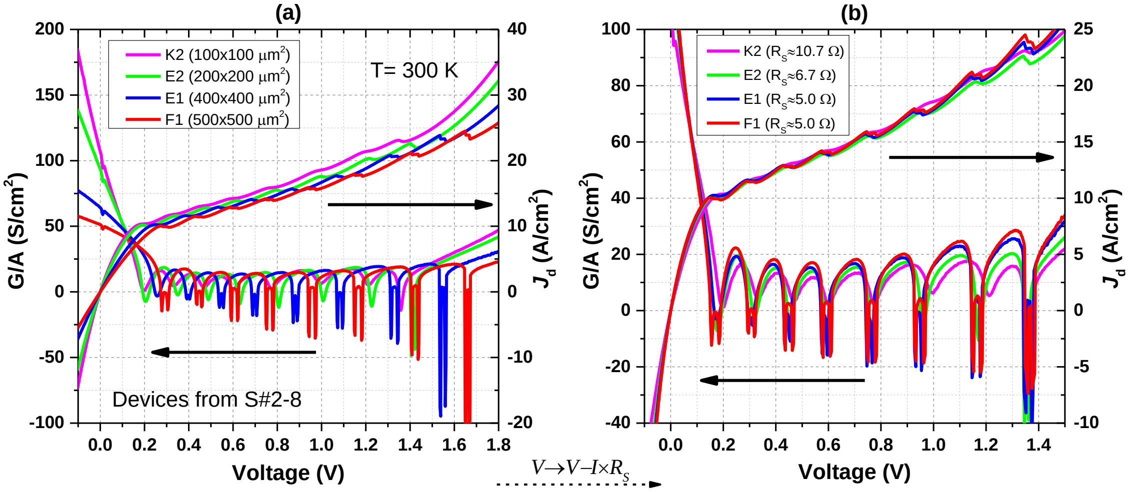

Figure 7.3: *G/A* and *J*d *vs. V* of devices with different sizes prepared from wafer S#2-8 at 300 K (a) without and (b) with the correction due to the circuit series resistance.

The observed locations and separation of NDC features depend on the device size. This is because the device resistances at high temperatures are relatively small (*e.g.* <50 Ω) so that the circuit series resistance, R_S = 5-11 Ω, could have a substantial voltage drop especially on the larger size devices, in which the device resistance is smaller while the current is higher compared to smaller devices. This is consistent with the increased separation between adjacent NDC features observed when the device size became larger as shown in Fig. 7.3(a). In principle, the positions of these NDC features should be located at the same voltages for different size devices if the circuit series resistance effect is negligible. To examine this, the dark current density and conductance (G/A) are plotted with respect to the voltage drop on the device (*i.e*. substituting the voltage V with $V\text{-}I\times R_S$) for different sizes as shown in Fig. 7.3(b). Indeed, the positions of NDC features observed from these devices are essentially the same for different sizes, suggesting that multiple NDC features are inherent properties of these ICIP structures.

7.4.1 ICIPs with 3- and 4-QWs in the electron barrier

In order to further understand and substantiate this resonant-tunneling mechanism, ICIPs with different eBs, *p*-doping concentrations in the absorbers, and hBs were investigated (see Table 7.1). Compared to the ICIPs in set #3, the ICIPs in set #4 had an extra QW in the eBs to reduce the intraband tunneling of electrons. As can be seen in Fig. 7.4(a-c), both dark current densities and NDCs are substantially reduced for ICIPs in set #4 compared to those in set #3. Comparing the devices with the same cascade stage number between sets #3 and 4, the dark current in the devices with the enhanced eB in set #4 was reduced considerably (by ~20%, as shown in Fig. 7.4(a-c)), indicating effective suppression of the intraband tunneling current by the enhanced eB. This also verifies that the observed current peaks/NDC features in ICIPs originate from resonant intraband tunneling through eBs.

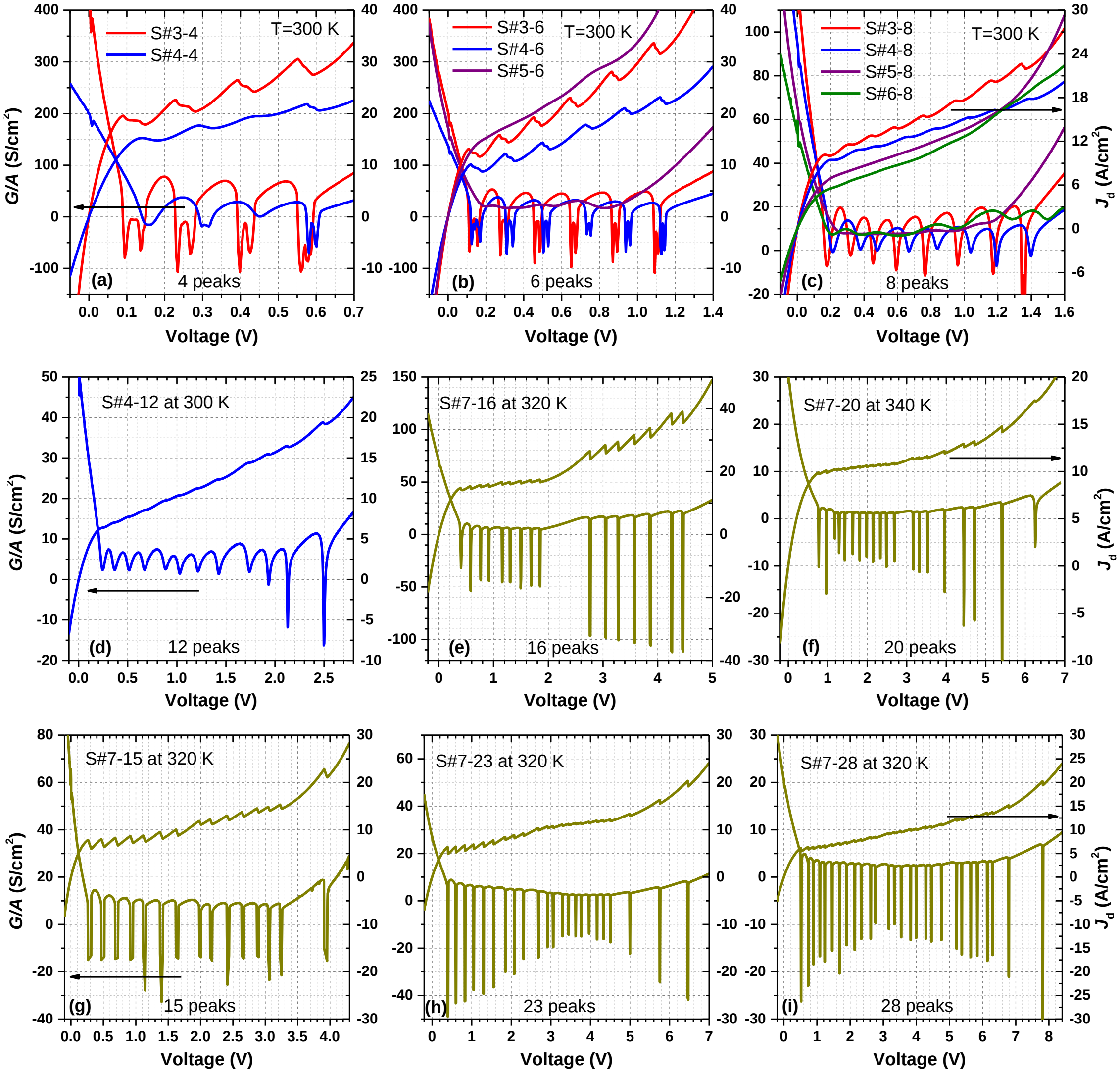

Figure 7.4: Differential conductance/area (*G*/*A*) and dark current density *vs.* voltage bias for the ICIPs from different set. (a) 3 QWs vs. 4 QWs in an eB, (b) comparison with changes in eB and doping, (c) comparison with changes in eB, doping and hB.

7.4.2 ICIPs with higher doping in absorbers

As the tunneling current is approximately proportional to the electron concentration, the peaks/NDC features in ICIPs should also be related to the *p*-type doping concentration in the absorbers. With all other parameters kept the same as in set #4, the absorbers in the ICIPs of set #5 are *p*-type doped at a concentration that is about two times higher than that in set #4, resulting in a lowered minority carrier density. This should lead to a reduced intraband tunneling current and less significant NDC features. Indeed, comparing the devices with the same N_C (6 and 8) between set #4 and set #5, the NDC features are much smaller from the devices in set #5 and could only be clearly identified at higher temperatures, such as 340 K (see Fig. 7.5). Also, as shown in Fig. 7.4(c), the dark current density is lower in the eight-stage device from S#3-8, resulting in a higher detectivity D^* (the responsivity is similar), as shown in Fig. 7.1 and Table 7.1. The six-stage device from S#5-6 had a higher J_d (Fig. 7.4(b)) due to some leakage current associated with higher defect densities observed in wafer S#5-6 compared to wafer S#4-6. This is not related to intraband tunneling as evidenced by its nearly flat differential conductance in the NDC feature region of S#4-6 at 300 K (Fig. 7.4(b)).

7.4.3 ICIP with modified hole barrier

As pointed out above, there are two transport paths for electrons travelling through the electron barriers (see Fig. 7.2). How easily electrons move along one path will affect the fraction of electrons going along the other path, and this will affect the current peaks/NDC features in ICIPs. The relaxation region (hB) in wafer S#6-8 is wider, with the electron state at a lower energy compared to the hB in the other wafers. Consequently, the interband tunneling window (at the interface between the hB and eB) is widened. As such, more electrons from the absorber will go along the first transport path through the hB and interband tunneling, and fewer electrons will go through via intraband tunneling through the eB. As shown in Fig. 7.4(c) at 300 K, the ICIP from S#6-8 exhibited a reduced dark current density, with much smaller NDC features compared to the device from wafer S#4-8. Note, S#4-8 differs from S#6-8 only in the hBs, and the NDC features in S#6-8 did not appear until higher temperatures (320 and 340 K), as shown in Fig. 7.5(d).

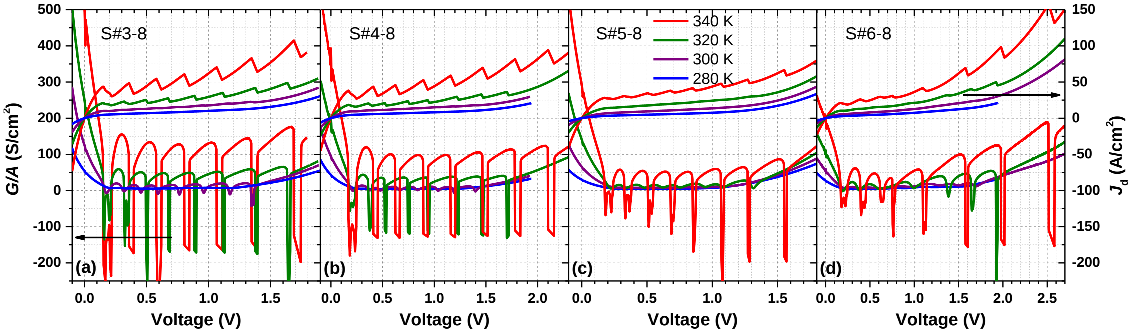

Figure 7.5: Differential conductance/area (*G/A*) and dark current density *vs.* voltage bias for the eight-stage devices at 280 to 340 K.

7.4.4 ICIPs with identical thin absorbers

Finally, ICIPs with relatively thin absorbers and with more cascade stages were studied, from wafers in set #7 and S#4-12. With thin absorbers, the number of available electrons per stage is effectively reduced and thus the dark current density is reduced compared to S#4-8 (see Fig. 7.4(d-i)). Consequently, NDC features were not clearly observed until a large bias voltage was applied (for devices from S#4-12) or a higher temperature was reached (for devices from set #7). For the five ICIPs from set #7 with identical thin absorbers, the number of NDC features show excellent agreement with the number of cascade stages of 15, 16, 20, 23, and 28, respectively. As shown in Fig 7.4(e-i), NDC features can be observed at 320 K and above for these devices. However, the appearance of NDC features at a higher temperature (340 K) for S#7-20 is due to its relative wider bandgap compared to the other ones, hence lower carrier concentration. Therefore, a higher temperature is required for S#7-20 to reach a certain level of carrier concentration to realize resonant tunneling.

7.5 Summary and concluding remarks

These ICIPs with more cascade stages showed somewhat higher Johnson-noise-limited detectivities, as indicated in Table 7.1. Overall, these ICIPs operated at zero-bias and their D^* did not vary much among the structures (see Table 7.1) because the resonant tunneling occurred at a reverse bias. Nevertheless, the Johnson-noise-limited detectivities for these ICIPs at 300 K at 8 µm exceeded 1.0×10^8 cm·Hz$^{1/2}$/W, which is more than a factor of two higher than the corresponding values for photovoltaic HgCdTe detectors with similar cutoff wavelengths [1,2]. Additionally, in order to effectively couple to an external circuit, it is beneficial for ICIPs to have a significantly large resistance with a much reduced dark current density, especially at high temperatures. Hence, it is important to minimize the dark current density with optimized structures.

In summary, multiple NDC features are observed in LW ICIPs. These NDC features are shown to be related to intraband tunneling of minority carriers through the electron barriers, leading to the sequential turn-off of resonant tunneling in the eBs. By varying the detailed structure and the carrier concentrations in the absorber, The details of these phenomena have been substantiated. Furthermore, the NDC features in the ICIPs can be used as a characterization tool that will improve the understanding of ICIPs and related interband cascade devices, leading to advancements in device performance.

Chapter 8 Conclusion and future work

8.1 Dissertation summary

This dissertation mainly focused on interband cascade infrared photodetectors which originated from interband cascade lasers. Along with interband cascade infrared thermophotovoltaics they make up the interband cascade structure family, which is unique for its multi-stage architecture. In these devices, the carrier transport is rectified with two unipolar barriers (injectors), namely the electron barrier (hole injector) and hole barrier (electron injector). The series connection between cascade stages is realized by employing the type-II broken-gap alignment between InAs and GaSb layers, rather than Esaki tunnel junctions. These interband cascade devices with a multiple stage structure fundamentally have a superior performance over conventional single stage devices.

Since most of the IR detectors are typically operated at low temperatures, and the device performance of $Hg_{1-x}Cd_xTe$ detectors are not optimal at high temperatures, it is important to develop an uncooled IR detector with high device performance. The aim of this dissertation was to investigate the theoretically projected enhancements of multi-stage ICIPs over the conventional single stage IR detectors in terms of higher detectivities, higher operating temperature (HOT) in both MWIR and LWIR ranges, and to show the potential of ICIPs for high speed application.

In this dissertation, after a brief overview of IR radiation and the corresponding applications. A survey of different infrared detector technologies was presented in chapter 1. The operating principles of the interband cascade devices were introduced in chapter 2. Detailed discussion was focused on the theory of ICIPs to qualitatively imply their advantages, and a comparison between a single absorber detector and the multi-stage ICIP showed the fundamental advantages of ICIPs. The following chapters are dedicated to the design, characterization and analysis of ICIPs in the MWIR and LWIR bands.

In chapter 3, a set of MW ICIPs based on an InAs/GaSb T2SL was investigated with both regular and reverse illumination configurations. The 100% cutoff wavelength was 4.3 µm at 300 K. Four one-stage detectors with different absorber thicknesses and substrates were included for comparison to the multiple-stage ICIPs with different absorber thicknesses, numbers of stages, and illumination configurations, as well as variations in substrate and buffer layer doping concentration. The multi-stage ICIPs were capable of operating at high temperatures at zero-bias with Johnson-noise limited detectivities over 1.0×10^9 cm·Hz$^{1/2}$/W at 300 K, and the D^* values were enhanced by a factor of two under certain reverse bias conditions. However, their performance was limited by undesired substrate effects and should be enhanced with better materials quality. The ICIPs exhibited superior carrier transport over the conventional one-stage detectors, particularly at higher temperatures with a reduced diffusion length. ICIPs with thin discrete absorbers showed a monotonically increasing zero-bias responsivity with increasing temperature up to 300 K, while the responsivity of the one-stage devices began to drop at 200 or 250 K. Based on the temperature dependence and the bias sensitivity of their responsivities with various absorber thicknesses, the diffusion length is estimated to be between 0.6 to 1.0 µm for T2SL materials at high temperatures (>250 K). By comparing responsivities between current matched ICIPs with various absorber thicknesses and noncurrent-matched ICIPs with equal absorbers, it was shown that the current-matching between cascade stages is important and necessary to achieve the maximum responsivity. In addition, electrical gain exceeding unity was demonstrated in these detectors in the reverse illumination configuration. This is the first time that electrical gain was observed in the ICIPs with T2SL absorbers. Based on these MWIR ICIPs, high-frequency operation with a 3-dB bandwidth of 1.3 GHz was demonstrated at room temperature.

In chapter 4, bulk GaInAsSb alloy was first time employed as the absorbers of an ICIP. A three-stage ICIP and a conventional one-stage device were investigated, both detectors were demonstrated at operating temperatures up to 340 K with a cutoff wavelength around 4.5 μm at 300 K. The observed absorption coefficients (e.g. ~5000 cm^{-1} at 3.3 μm) were significantly higher than the typical value (2000-3000 cm^{-1}) in T2SLs. The Johnson-noise limited detectivity of both detectors reached 10^9 $cm \cdot Hz^{1/2}/W$ at 300 K, which is comparable to the T2SL photodetectors with similar cutoff wavelengths as mentioned in chapter 4. In addition, these GaInAsSb detectors exhibited a much higher responsivity due to a larger absorption coefficient, indicating an enhanced output signal compared to the T2SL detectors. This suggested a possible improved frequency response in the ICIPs with GaInAsSb absorbers that are feasible for high speed application. Overall, the successful implantation with quaternary GaInAsSb alloy validated the advantages of ICIPs for high device performance and high operating temperature, not only remained in T2SL, but also with bulk materials. Moreover, it also implied the other degree of flexibility of ICIPs by utilizing of others available alternative materials as the absorbers for meeting specific applications.

In chapter 5, four sets of LW ICIPs were systematically investigated with a 90% cutoff wavelength between 7.5 μm and 11.5 μm from 78 to 340 K. It is the first time ICIPs are demonstrated to be operated at high temperatures up to 340 K in the LWIR region, proving the benefit of LW ICIPs for high temperature operation according to the theoretical projections. Although not yet optimized, the ICIPs achieved high performance with D^* higher than 1.0×10^9 and 1.0×10^8 $\mathrm{cm{\cdot}Hz^{1/2}/W}$ at 200 and 300 K, respectively. These are among the best results demonstrated for uncooled photovoltaic detectors in the LWIR region. To the best of my knowledge, ICIP is the only HOT photodetector with high device performance that can beat the top $Hg_{1-x}Cd_xTe$ detector in the LWIR band, suggesting a great potential for real applications such as laser spectroscopy and free-space communication in combination with room temperature long-wavelength quantum cascade lasers. Nevertheless, better device performance is expected by further optimizing these ICIPs.

The appearance of multiple negative differential conductance (NDC) features was identified as related to intraband tunneling through the electron barrier, with further investigations described in chapter 7.

In chapter 6, a comparison study was discussed between two sets of LW ICIPs with current matched and non-current matched architectures. These ICIPs have a comparable performance ($D^*>1.0\times10^8$ $\mathrm{cm{\cdot}Hz^{1/2}/W}$ at 300 K) with a similar cutoff wavelength around 11 μm at 300 K to the ICIPs discussed in chapter 5. The necessity of current-matching to maximize photon absorption for optimal responsivity was, again, illustrated. The lower responsivity in the non-current matched ICIPs was attributed to light attenuation in the optically deeper stages, but was enhanced by the significant higher electrical gain, such that the device performance was comparable or even slightly higher than for current matched ICIPs. Therefore, the benefits of non-current matched ICIPs are implied in terms of easier structure design and device implementation.

The presence of high electrical gain in the ICIPs was postulated to be related to two mechanisms, one is the photoconductive gain due to a shorter transit time than carrier lifetime, the one is current compensation of the dark current required to maintain current continuity. Further theoretical and experimental studies are needed to fully understand the electrical gain.

In chapter 7, to fully understand the underlying physics behind the multiple NDC features observed in LW ICIPs as partially mentioned in chapter 6, a systematic research was performed with five sets of LW ICIPs by varying the detailed structure and the carrier concentrations in the absorber. The multiple NDC features were explained to be related to the sequential turn-off of intraband tunneling of minority carriers through the electron barriers. As such, the NDC features in the ICIPs can be used as a characterization tool that will improve the understanding of ICIPs and related interband cascade devices, leading to advancements in device performance.

Overall, this dissertation demonstrated the high temperature operation of ICIPs with high device performance in both MWIR and LWIR band. High frequency operation with a 3-dB bandwidth of 1.3 GHz has been established based on the MW ICIPs. Above room temperature operation of LW ICIPs has been achieved for the first time with a cutoff wavelength around 11 µm at 300 K. Up to now, this is the only uncooled LWIR photodetector exhibits a higher device performance than the commercial photovoltaic $Hg_{1-x}Cd_xTe$ detectors. The improved understanding of the electrical gain with further optimization will lead to enhanced performance of future ICIP devices.

8.2 Suggested future work

Although ICLs have been developed for more than two decades, ICIPs are still in their preliminary phase with plenty of room for improvement. Below, several suggestions are provided for future research.

As discussed in this dissertation, electrical gain is observed in most of our ICIPs, thus the analysis of carrier transport based on the temperature dependence of zero-bias responsivities cannot fully explain the processes. Therefore, absorption coefficients at low temperatures are necessary to understand the carrier transport with changing temperature, as well as to extract the electrical gain at each temperature. In order to further understand the dynamics, measurements of carrier lifetime and diffusion length at a wide temperature range are rather important for device design and analysis.

Since the determination of the detectivity of our ICIPs only considered the Johnson noise and shot noise extracted from the device current, the value may be overestimated if the other noise sources are not negligible. Hence, it is vital to directly measure the other noise mechanisms in the devices, in order to better evaluate the actual device performances.

High frequency operation of uncooled ICIPs has been demonstrated with a 3-dB bandwidth of 1.3 GHz [91]. However, this is far below the optimum value and is limited by the device packaging. With improvements in the device packaging, a better frequency response is expected. Meanwhile, a systematic study of the frequency response of ICIPs can be carried out by varying the structural parameters, such as absorber thickness, number of stages, identical absorbers and illumination configurations. Analogous studies of IC LEDs would also be beneficial.

Detectors based on T2SLs are limited by low absorption coefficients and relatively high defect densities, while absorbers based on bulk materials could compensate for these issues. Photodetectors based on InAsSb have shown high performance [54,55,194,195] in the MWIR and LWIR bands. Since ICIPs based on a quaternary GaInAsSb alloy as the absorber material have been established, as discussed in chapter 3, InAsSb alloys may be another promising alternative for the absorbers in ICIPs. The defects in InAs/GaSb T2SLs have been attributed to the Ga atoms [196]. Therefore, several groups have employed Ga-free InAsSb/InAs T2SLs in their detectors [197] and obtained improved minority carrier lifetimes [198,199] and high device performance [166,200] in the LWIR region.

ICTPVs based on T2SLs with the same bandgap for each absorber have demonstrated advantages over one-stage TPV devices. Meanwhile, as discussed above, ICTPVs can also make use of the advantages of bulk materials as the absorber to enhance absorption and increase the short-circuit current, or employ InAsSb/InAs T2SLs as the absorbers to reduce dark current and enhance the open-circuit voltage. Additionally, considering that heat sources are typically broadband, ICTPVs can take advantages from multi-junction solar cells by varying the bandgaps of the absorbers in different cascade stages to enhance the absorption of incident photons and hence increase the conversion efficiency.

References

[1] P. Martyniuk and A. Rogalski, “HOT infrared photodetectors,” Opto-Electronics Review **21,** 239 (2013).

[2] Vigo System S.A. catalogue. https://www.vigo.com.pl/products/infrared-detectors.

[3] C. H. Grein, P. M. Young, and H. Ehrenreich, “Minority carrier lifetimes in ideal InGaSb/InAs superlattices,” Applied Physics Letters **61,** 2905 (1992).

[4] C. H. Grein, H. Cruz, M. E. Flatté, and H. Ehrenreich, “Theoretical performance of very long wavelength InAs/$In_xGa_{1-x}Sb$ superlattice based infrared detectors,” Applied Physics Letters **65,** 2530 (1994).

[5] C. H. Grein, P. M. Young, M. E. Flatté, and H. Ehrenreich, “Long wavelength InAs/InGaSb infrared detectors: Optimization of carrier lifetimes,” Journal of Applied Physics **78,** 7143 (1995).

[6] D. L. Smith and C. Mailhiot, “Proposal for strained type II superlattice infrared detectors,” Journal of Applied Physics **62,** 2545 (1987).

[7] E. R. Youngdale, J. R. Meyer, C. A. Hoffman, F. J. Bartoli, C. H. Grein, P. M. Young, H. Ehrenreich, R. H. Miles, and D. H. Chow, “Auger lifetime enhancement in InAs–$Ga_{1-x}In_xSb$ superlattices,” Applied Physics Letters **64,** 3160 (1994).

[8] H. Mohseni, V. I. Litvinov, and M. Razeghi, “Interface-induced suppression of the Auger recombination in type-II InAs/GaSb superlattices,” Physical Review B **58,** 15378 (1998).

[9] S. Maimon and G. W. Wicks, “nBn detector, an infrared detector with reduced dark current and higher operating temperature,” Applied Physics Letters **89,** 151109 (2006).

[10] D. Z. Y. Ting, A. Soibel, L. Höglund, J. Nguyen, C. J. Hill, A. Khoshakhlagh, and S. D. Gunapala, Chapter 1 "Type-II Superlattice Infrared Detectors" in *Semiconductors and Semimetals*; *Vol. 84,* edited by D. R. R. Sarath D. Gunapala and J. Chennupati (Elsevier, 2011).

[11] J. R. Pedrazzani, S. Maimon, and G. W. Wicks, “Use of nBn structures to suppress surface leakage currents in unpassivated InAs infrared photodetectors,” Electronics Letters **44,** 1487 (2008).

[12] G. R. Savich, J. R. Pedrazzani, S. Maimon, and G. W. Wicks, “Suppression of surface leakage currents using molecular beam epitaxy-grown unipolar barriers,” Journal of Vacuum Science & Technology B: Microelectronics and Nanometer Structures **28,** C3H18 (2010).

[13] G. R. Savich, J. R. Pedrazzani, S. Maimon, and G. W. Wicks, “Use of epitaxial unipolar barriers to block surface leakage currents in photodetectors,” Physica Status Solidi (C) **7,** 2540 (2010).

[14] R. Q. Yang, Z. Tian, Z. Cai, J. F. Klem, M. B. Johnson, and H. C. Liu, “Interband-cascade infrared photodetectors with superlattice absorbers,” Journal of Applied Physics **107,** 054514 (2010).

[15] Z. Tian, R. T. Hinkey, R. Q. Yang, D. Lubyshev, Y. Qiu, J. M. Fastenau, W. K. Liu, and M. B. Johnson, “Interband cascade infrared photodetectors with enhanced electron barriers and p-type superlattice absorbers,” Journal of Applied Physics **111,** 024510 (2012).

[16] D. Z.-Y. Ting, C. J. Hill, A. Soibel, S. A. Keo, J. M. Mumolo, J. Nguyen, and S. D. Gunapala, “A high-performance long wavelength superlattice complementary barrier infrared detector,” Applied Physics Letters **95,** 023508 (2009).

[17] N. K. Dhar, R. Dat, and A. K. Sood, Chapter 7 "Advances in Infrared Detector Array Technology" in *Optoelectronics - Advanced Materials and Devices*, edited by S. L. Pyshkin and J. M. Ballato (InTech, Rijeka, 2013).

[18] J. S. Li, W. Chen, and H. Fischer, “Quantum Cascade Laser Spectrometry Techniques: A New Trend in Atmospheric Chemistry,” Applied Spectroscopy Reviews **48,** 523 (2013).

[19] A. Rogalski, P. Martyniuk, and M. Kopytko, “Challenges of small-pixel infrared detectors: a review,” Reports on Progress in Physics **79,** 046501 (2016).

[20] A. Konczakowska and B. M. Wilamowski, “Noise in semiconductor devices,” Industrial Electronics Handbook **1** (2011).

[21] A. Rose, *Concepts in photoconductivity and allied problems* (Interscience publishers, 1963).

[22] C.-T. Sah, R. N. Noyce, and W. Shockley, “Carrier generation and recombination in pn junctions and pn junction characteristics,” Proceedings of the IRE **45,** 1228 (1957).

[23] M. B. Reine, A. K. Sood, and T. J. Tredwell, Chapter 6 "Photovoltaic Infrared Detectors" in *Semiconductors and Semimetals*; *Vol. 18*, edited by R. K. Willardson and C. B. Albert (Elsevier, 1981).

[24] V. Gopal, S. K. Singh, and R. M. Mehra, “Analysis of dark current contributions in mercury cadmium telluride junction diodes,” Infrared Physics & Technology **43,** 317 (2002).

[25] H. K. Chung, M. A. Rosenberg, and P. H. Zimmermann, “Origin of 1/f noise observed in $Hg_{0.7}Cd_{0.3}Te$ variable area photodiode arrays,” Journal of Vacuum Science & Technology A: Vacuum, Surfaces, and Films **3,** 189 (1985).

[26] Y. P. Varshni, “Temperature dependence of the energy gap in semiconductors,” Physica **34,** 149 (1967).

[27] A. Rogalski, “History of infrared detectors,” Opto-Electronics Review **20,** 279 (2012).

[28] M. M. Rao, *Optical communication* (Universities press, 2001).

[29] B. F. Levine, K. K. Choi, C. G. Bethea, J. Walker, and R. J. Malik, “New 10 μm infrared detector using intersubband absorption in resonant tunneling GaAlAs superlattices,” Applied Physics Letters **50,** 1092 (1987).

[30] H. Schneider, “Optimized performance of quantum well intersubband infrared detectors: Photovoltaic versus photoconductive operation,” Journal of Applied Physics **74,** 4789 (1993).

[31] H. Schneider and H. C. Liu, *Quantum well infrared photodetectors* (Springer, Berlin, 2007).

[32] V. Guériaux, N. B. de l’Isle, A. Berurier, O. Huet, A. Manissadjian, H. Facoetti, X. Marcadet, M. Carras, V. Trinité, and A. Nedelcu, “Quantum well infrared photodetectors: present and future,” Optical Engineering **50,** 061013 (2011).

[33] E. Costard, J. P. Truffer, O. Huet, L. Dua, A. Nedelcu, J. Robo, X. Marcadet, N. B. de l'Isle, and P. Bois, "QWIP from 4 μm up to 18 μm," *Remote Sensing,* 636117 (2006).

[34] K. Brunner, U. Bockelmann, G. Abstreiter, M. Walther, G. Böhm, G. Tränkle, and G. Weimann, “Photoluminescence from a single GaAs/AlGaAs quantum dot,” Physical Review Letters **69,** 3216 (1992).

[35] D. Bimberg, N. Kirstaedter, N. Ledentsov, Z. I. Alferov, P. Kop'Ev, and V. Ustinov, “InGaAs-GaAs quantum-dot lasers,” IEEE Journal of selected topics in quantum electronics **3,** 196 (1997).

[36] J. Phillips, K. Kamath, and P. Bhattacharya, “Far-infrared photoconductivity in self-organized InAs quantum dots,” Applied Physics Letters **72,** 2020 (1998).

[37] J. C. Campbell and A. Madhukar, “Quantum-dot infrared photodetectors,” Proceedings of the IEEE **95,** 1815 (2007).

[38] P. Martyniuk and A. Rogalski, “Quantum-dot infrared photodetectors: Status and outlook,” Progress in Quantum Electronics **32,** 89 (2008).

[39] X. Lu, J. Vaillancourt, and G. Gu, “A plasmonic perfect absorber enhanced longwave infrared quantum dot infrared photodetector with high quantum efficiency,” Journal of Physics D: Applied Physics **50,** 135101 (2017).

[40] H. C. Liu, M. Gao, J. McCaffrey, Z. R. Wasilewski, and S. Fafard, “Quantum dot infrared photodetectors,” Applied Physics Letters **78,** 79 (2001).

[41] J. Phillips, “Evaluation of the fundamental properties of quantum dot infrared detectors,” Journal of Applied Physics **91,** 4590 (2002).

[42] H. Schneider, K. Kheng, M. Ramsteiner, J. D. Ralston, F. Fuchs, and P. Koidl, “Transport asymmetry and photovoltaic response in (AlGa)As/AlAs/GaAs/(AlGa)As single-barrier quantum-well infrared detectors,” Applied Physics Letters **60,** 1471 (1992).

[43] D. Hofstetter, M. Beck, and J. Faist, “Quantum-cascade-laser structures as photodetectors,” Applied Physics Letters **81,** 2683 (2002).

[44] F. R. Giorgetta, E. Baumann, D. Hofstetter, C. Manz, Q. Yang, K. Köhler, and M. Graf, “InGaAs⁄AlAsSb quantum cascade detectors operating in the near infrared,” Applied Physics Letters **91,** 111115 (2007).

[45] M. Graf, G. Scalari, D. Hofstetter, J. Faist, H. Beere, E. Linfield, D. Ritchie, and G. Davies, “Terahertz range quantum well infrared photodetector,” Applied Physics Letters **84,** 475 (2004).

[46] P. Reininger, B. Schwarz, H. Detz, D. MacFarland, T. Zederbauer, A. M. Andrews, W. Schrenk, O. Baumgartner, H. Kosina, and G. Strasser, “Diagonal-transition quantum cascade detector,” Applied Physics Letters **105,** 091108 (2014).

[47] D. Hofstetter, M. Graf, T. Aellen, J. Faist, L. Hvozdara, and S. Blaser, “23 GHz operation of a room temperature photovoltaic quantum cascade detector at 5.35 μm,” Applied Physics Letters **89,** 061119 (2006).

[48] A. Vardi, S. Sakr, J. Mangeney, P. K. Kandaswamy, E. Monroy, M. Tchernycheva, S. E. Schacham, F. H. Julien, and G. Bahir, “Femto-second electron transit time characterization in GaN/AlGaN quantum cascade detector at 1.5 micron,” Applied Physics Letters **99,** 202111 (2011).

[49] S. Sakr, P. Crozat, D. Gacemi, Y. Kotsar, A. Pesach, P. Quach, N. Isac, M. Tchernycheva, L. Vivien, G. Bahir, E. Monroy, and F. H. Julien, “GaN/AlGaN waveguide quantum cascade photodetectors at $\lambda \approx 1.55$ μm with enhanced responsivity and ~40 GHz frequency bandwidth,” Applied Physics Letters **102,** 011135 (2013).

[50] F. R. Giorgetta, E. Baumann, M. Graf, Q. Yang, C. Manz, K. Kohler, H. E. Beere, D. A. Ritchie, E. Linfield, A. G. Davies, Y. Fedoryshyn, H. Jackel, M.

Fischer, J. Faist, and D. Hofstetter, "Quantum Cascade Detectors," IEEE Journal of Quantum Electronics **45,** 1039 (2009).

[51] G. R. Savich, J. R. Pedrazzani, D. E. Sidor, S. Maimon, and G. W. Wicks, "Dark current filtering in unipolar barrier infrared detectors," Applied Physics Letters **99,** 121112 (2011).

[52] G. R. Savich, J. R. Pedrazzani, D. E. Sidor, and G. W. Wicks, "Benefits and limitations of unipolar barriers in infrared photodetectors," Infrared Physics & Technology **59,** 152 (2013).

[53] P. Klipstein, "XBn'barrier photodetectors for high sensitivity and high operating temperature infrared sensors," *Proc. SPIE,* **6940**, 69402U (2008).

[54] P. Klipstein, O. Klin, S. Grossman, N. Snapi, I. Lukomsky, D. Aronov, M. Yassen, A. Glozman, T. Fishman, and E. Berkowicz, "XBn barrier photodetectors based on InAsSb with high operating temperatures," Optical Engineering **50,** 061002 (2011).

[55] A. Soibel, C. J. Hill, S. A. Keo, L. Hoglund, R. Rosenberg, R. Kowalczyk, A. Khoshakhlagh, A. Fisher, D. Z.-Y. Ting, and S. D. Gunapala, "Room temperature performance of mid-wavelength infrared InAsSb nBn detectors," Applied Physics Letters **105,** 023512 (2014).

[56] A. M. Itsuno, J. D. Phillips, and S. Velicu, "Design and Modeling of HgCdTe nBn Detectors," Journal of Electronic Materials **40,** 1624 (2011).

[57] A. M. Itsuno, J. D. Phillips, and S. Velicu, "Mid-wave infrared HgCdTe nBn photodetector," Applied Physics Letters **100,** 161102 (2012).

[58] M. Kopytko, A. Kębłowski, W. Gawron, P. Madejczyk, A. Kowalewski, and K. Jóźwikowski, "High-operating temperature MWIR nBn HgCdTe detector grown by MOCVD," Opto-Electronics Review **21,** 402 (2013).

[59] J. L. Johnson, L. A. Samoska, A. C. Gossard, J. L. Merz, M. D. Jack, G. R. Chapman, B. A. Baumgratz, K. Kosai, and S. M. Johnson, "Electrical and optical properties of infrared photodiodes using the InAs/$Ga_{1-x}In_xSb$ superlattice in heterojunctions with GaSb," Journal of Applied Physics **80,** 1116 (1996).

[60] J. E. A. DeCuir, G. P. Meissner, P. S. Wijewarnasuriya, N. Gautam, S. Krishna, N. K. Dhar, R. E. Welser, and A. K. Sood, "Long-wave type-II superlattice detectors with unipolar electron and hole barriers," Optical Engineering **51,** 124001 (2012).

[61] A. Soibel, D. Z. Y. Ting, C. J. Hill, M. Lee, J. Nguyen, S. A. Keo, J. M. Mumolo, and S. D. Gunapala, "Gain and noise of high-performance long wavelength superlattice infrared detectors," Applied Physics Letters **96,** 111102 (2010).

[62] N. Gautam, S. Myers, A. V. Barve, B. Klein, E. P. Smith, D. R. Rhiger, L. R. Dawson, and S. Krishna, "High operating temperature interband cascade midwave infrared detector based on type-II InAs/GaSb strained layer superlattice," Applied Physics Letters **101,** 021106 (2012).

[63] Z.-B. Tian, S. E. Godoy, H. S. Kim, T. Schuler-Sandy, J. A. Montoya, and S. Krishna, "High operating temperature interband cascade focal plane arrays," Applied Physics Letters **105,** 051109 (2014).

[64] H. Lotfi, L. Li, H. Ye, R. T. Hinkey, L. Lei, R. Q. Yang, J. C. Keay, T. D. Mishima, M. B. Santos, and M. B. Johnson, "Interband cascade infrared photodetectors with long and very-long cutoff wavelengths," Infrared Physics & Technology **70,** 162 (2015).

[65] H. Lotfi, L. Lei, L. Li, R. Q. Yang, J. C. Keay, M. B. Johnson, Y. Qiu, D. Lubyshev, J. M. Fastenau, and A. W. K. Liu, "High-temperature operation of interband cascade infrared photodetectors with cutoff wavelengths near 8 μm," Optical Engineering **54,** 063103 (2015).

[66] L. Li, H. Ye, Y. Jiang, R. Q. Yang, J. C. Keay, T. D. Mishima, M. B. Santos, and M. B. Johnson, "MBE-grown long-wavelength interband cascade lasers on InAs substrates," Journal of Crystal Growth **425,** 369 (2015).

[67] W. W. Bewley, C. L. Canedy, C. S. Kim, C. D. Merritt, M. V. Warren, I. Vurgaftman, J. R. Meyer, and M. Kim, "Room-temperature mid-infrared interband cascade vertical-cavity surface-emitting lasers," Applied Physics Letters **109,** 151108 (2016).

[68] 楊瑞青, 李路, and 江宇超, "带间级联激光器: 从原始概念到实际器件," 物理学进展 **34,** 169 (2014).

[69] G. A. Sai-Halasz, R. Tsu, and L. Esaki, "A new semiconductor superlattice," Applied Physics Letters **30,** 651 (1977).

[70] H. Ye, L. Li, H. Lotfi, L. Lei, R. Q. Yang, J. C. Keay, T. D. Mishima, M. B. Santos, and M. B. Johnson, "Molecular beam epitaxy of interband cascade structures with InAs/GaSb superlattice absorbers for long-wavelength infrared detection," Semiconductor Science and Technology **30,** 105029 (2015).

[71] R. Kazarinov, "Possibility of amplification of electromagnetic waves in a semiconductor with superlattice," Sov. Phys.-Semicond. **5,** 707 (1971).

[72] J. Faist, F. Capasso, D. L. Sivco, C. Sirtori, A. L. Hutchinson, and A. Y. Cho, "Quantum cascade laser," Science **264,** 553 (1994).

[73] R. Q. Yang, "Infrared laser based on intersubband transitions in quantum wells," Superlattices and Microstructures **17,** 77 (1995).

[74] R. Q. Yang, B. H. Yang, D. Zhang, C.-H. Lin, S. J. Murry, H. Wu, and S. S. Pei, "High power mid-infrared interband cascade lasers based on type-II quantum wells," Applied Physics Letters **71,** 2409 (1997).

[75] R. Q. Yang, L. Li, L. Zhao, Y. Jiang, Z. Tian, H. Ye, R. Hinkey, C. Niu, T. D. Mishima, and M. B. Santos, "Recent progress in development of InAs-based interband cascade lasers,*" Proc. SPIE,* **8640**, 86400Q (2013).

[76] I. Vurgaftman, J. R. Meyer, and L. R. Ram-Mohan, "Mid-IR vertical-cavity surface-emitting lasers," IEEE Journal of Quantum Electronics **34,** 147 (1998).

[77] R. Q. Yang, "InAs-based quantum cascade lasers with enhanced confinement," Semiconductor Science and Technology **30,** 105023 (2015).

[78] L. Li, Y. Jiang, H. Ye, R. Q. Yang, T. D. Mishima, M. B. Santos, and M. B. Johnson, "Low-threshold InAs-based interband cascade lasers operating at high temperatures," Applied Physics Letters **106,** 251102 (2015).

[79] J. Scheuermann, R. Weih, M. v. Edlinger, L. Nähle, M. Fischer, J. Koeth, M. Kamp, and S. Höfling, "Single-mode interband cascade lasers emitting below 2.8 μm," Applied Physics Letters **106,** 161103 (2015).

[80] W. W. Bewley, C. L. Canedy, C. S. Kim, M. Kim, C. D. Merritt, J. Abell, I. Vurgaftman, and J. R. Meyer, "Continuous-wave interband cascade lasers operating above room temperature at λ = 4.7-5.6 μm," Optics Express **20,** 3235 (2012).

[81] Y. Jiang, L. Li, R. Q. Yang, J. A. Gupta, G. C. Aers, E. Dupont, J.-M. Baribeau, X. Wu, and M. B. Johnson, "Type-I interband cascade lasers near 3.2 μm," Applied Physics Letters **106,** 041117 (2015).

[82] J. V. Li, R. Q. Yang, C. J. Hill, and S. L. Chuang, "Interband cascade detectors with room temperature photovoltaic operation," Applied Physics Letters **86,** 101102 (2005).

[83] R. T. Hinkey and R. Q. Yang, "Theory of multiple-stage interband photovoltaic devices and ultimate performance limit comparison of multiple-stage and single-stage interband infrared detectors," Journal of Applied Physics **114,** 104506 (2013).

[84] A. Baranov and E. Tournie, *Semiconductor lasers: Fundamentals and applications* (Elsevier, 2013).

[85] R. T. Hinkey and R. Q. Yang, "Comparison of ultimate limits of interband cascade infrared photodetectors and single-absorber detectors,*" Proc. SPIE,* **8868**, 886804 (2013).

[86] W. Pusz, A. Kowalewski, P. Martyniuk, W. Gawron, E. Plis, S. Krishna, and A. Rogalski, “Mid-wavelength infrared type-II InAs/GaSb superlattice interband cascade photodetectors,” Optical Engineering **53,** 043107 (2014).

[87] Z. B. Tian and S. Krishna, “Mid-Infrared Interband Cascade Photodetectors With Different Absorber Designs,” IEEE Journal of Quantum Electronics **51,** 1 (2015).

[88] H. Lotfi, L. Li, L. Lei, Y. Jiang, R. Q. Yang, J. F. Klem, and M. B. Johnson, “Short-wavelength interband cascade infrared photodetectors operating above room temperature,” Journal of Applied Physics **119,** 023105 (2016).

[89] Y. Zhou, J. Chen, Z. Xu, and L. He, “High quantum efficiency mid-wavelength interband cascade infrared photodetectors with one and two stages,” Semiconductor Science and Technology **31,** 085005 (2016).

[90] L. Lei, L. Li, H. Ye, H. Lotfi, R. Q. Yang, M. B. Johnson, J. A. Massengale, T. D. Mishima, and M. B. Santos, “Long wavelength interband cascade infrared photodetectors operating at high temperatures,” Journal of Applied Physics **120,** 193102 (2016).

[91] H. Lotfi, L. Li, L. Lei, H. Ye, S. M. Shazzad Rassel, Y. Jiang, R. Q. Yang, T. D. Mishima, M. B. Santos, J. A. Gupta, and M. B. Johnson, “High-frequency operation of a mid-infrared interband cascade system at room temperature,” Applied Physics Letters **108,** 201101 (2016).

[92] L. Lei, L. Li, H. Lotfi, H. Ye, R. Q. Yang, T. D. Mishima, M. B. Santos, and M. B. Johnson, “Midwavelength interband cascade infrared photodetectors with superlattice absorbers and gain,” Optical Engineering **57,** 011006 (2017).

[93] H. Lotfi, L. Lei, L. Li, R. Q. Yang, J. C. Keay, M. B. Johnson, Y. Qiu, D. Lubyshev, J. M. Fastenau, and A. W. K. Liu, "Long-wavelength interband cascade infrared photodetectors operating above room temperature," *Proc. SPIE,* **9370**, 937032 (2015).

[94] W. Huang, L. Lei, L. Li, J. A. Massengale, R. Q. Yang, T. D. Mishima, and M. B. Santos, “Current-matching versus non-current-matching in long wavelength interband cascade infrared photodetectors,” Journal of Applied Physics **122,** 083102 (2017).

[95] L. Lei, L. Li, H. Lotfi, Y. Jiang, R. Q. Yang, M. B. Johnson, D. Lubyshev, Y. Qiu, J. M. Fastenau, and A. W. Liu, “Mid-wave interband cascade infrared photodetectors based on GaInAsSb absorbers,” Semiconductor Science and Technology **31,** 105014 (2016).

[96] R. T. Hinkey, H. Lotfi, L. Li, H. Ye, L. Lei, R. Q. Yang, J. C. Keay, T. D. Mishima, M. B. Santos, and M. B. Johnson, "Interband cascade infrared

photodetectors with InAs/GaSb superlattice absorbers,*" Proc. SPIE,* **8868**, 886805 (2013).

[97] W. A. Beck, “Photoconductive gain and generation-recombination noise in multiple-quantum-well infrared detectors,” Applied Physics Letters **63,** 3589 (1993).

[98] C. Schönbein, H. Schneider, R. Rehm, and M. Walther, “Noise gain and detectivity of n-type GaAs/AlAs/AlGaAs quantum well infrared photodetectors,” Applied Physics Letters **73,** 1251 (1998).

[99] L. Lei, L. Li, H. Ye, H. Lotfi, R. Q. Yang, M. B. Johnson, J. A. Massengale, T. D. Mishima, and M. B. Santos, "Long wavelength interband cascade infrared photodetectors towards high temperature operation,*" Proc. SPIE*, **10111**, 1011113 (2017).

[100] M. G. Mauk, "Survey of Thermophotovoltaic (TPV) Devices" in *Mid-infrared Semiconductor Optoelectronics*, edited by A. Krier (Springer London, London, 2006).

[101] T. Bauer, *Thermophotovoltaics: basic principles and critical aspects of system design* (Springer Science & Business Media, 2011).

[102] B. Bitnar, W. Durisch, J. C. Mayor, H. Sigg, and H. R. Tschudi, “Characterisation of rare earth selective emitters for thermophotovoltaic applications,” Solar Energy Materials and Solar Cells **73,** 221 (2002).

[103] E. S. Sakr, Z. Zhou, and P. Bermel, “High efficiency rare-earth emitter for thermophotovoltaic applications,” Applied Physics Letters **105,** 111107 (2014).

[104] S. Molesky, C. J. Dewalt, and Z. Jacob, “High temperature epsilon-near-zero and epsilon-near-pole metamaterial emitters for thermophotovoltaics,” Optics Express **21,** A96 (2013).

[105] C. Argyropoulos, K. Q. Le, N. Mattiucci, G. D’Aguanno, and A. Alù, “Broadband absorbers and selective emitters based on plasmonic Brewster metasurfaces,” Physical Review B **87,** 205112 (2013).

[106] I. Johnson, W. T. Choate, and A. Davidson, “Waste Heat Recovery. Technology and Opportunities in U.S. Industry,” BCS. Inc., Laurel, MD, USA (2008).

[107] T. J. Coutts and J. S. Ward, “Thermophotovoltaic and photovoltaic conversion at high-flux densities,” IEEE Transactions on Electron Devices **46,** 2145 (1999).

[108] G. D. Cody, “Theoretical maximum efficiencies for thermophotovoltaic devices,” AIP Conference Proceedings **460,** 58 (1999).

[109] W. Shockley and H. J. Queisser, "Detailed Balance Limit of Efficiency of p-n Junction Solar Cells," Journal of Applied Physics **32,** 510 (1961).

[110] C. A. Wang, H. K. Choi, S. L. Ransom, G. W. Charache, L. R. Danielson, and D. M. DePoy, "High-quantum-efficiency 0.5 eV GaInAsSb/GaSb thermophotovoltaic devices," Applied Physics Letters **75,** 1305 (1999).

[111] M. W. Dashiell, J. F. Beausang, H. Ehsani, G. J. Nichols, D. M. Depoy, L. R. Danielson, P. Talamo, K. D. Rahner, E. J. Brown, S. R. Burger, P. M. Fourspring, W. F. TopperJr, P. F. Baldasaro, C. A. Wang, R. K. Huang, M. K. Connors, G. W. Turner, Z. A. Shellenbarger, G. Taylor, J. Li, R. Martinelli, D. Donetski, S. Anikeev, G. L. Belenky, and S. Luryi, "Quaternary InGaAsSb Thermophotovoltaic Diodes," IEEE Transactions on Electron Devices **53,** 2879 (2006).

[112] Y. Wang and Y.-y. Lou, "Radiant thermal conversion in 0.53 eV GaInAsSb thermophotovoltaic diode," Renewable Energy **75,** 8 (2015).

[113] R. Tuley, J. Orr, R. Nicholas, D. Rogers, P. Cannard, and S. Dosanjh, "Lattice-matched InGaAs on InP thermophovoltaic cells," Semiconductor Science and Technology **28,** 015013 (2012).

[114] A. Datas and C. Algora, "Global optimization of solar thermophotovoltaic systems," Progress in Photovoltaics: Research and Applications **21,** 1040 (2013).

[115] K. J. Cheetham, P. J. Carrington, N. B. Cook, and A. Krier, "Low bandgap GaInAsSbP pentanary thermophotovoltaic diodes," Solar Energy Materials and Solar Cells **95,** 534 (2011).

[116] R. Q. Yang, Z. Tian, J. F. Klem, T. D. Mishima, M. B. Santos, and M. B. Johnson, "Interband cascade photovoltaic devices," Applied Physics Letters **96,** 063504 (2010).

[117] H. Lotfi, R. T. Hinkey, L. Li, R. Q. Yang, J. F. Klem, and M. B. Johnson, "Narrow-bandgap photovoltaic devices operating at room temperature and above with high open-circuit voltage," Applied Physics Letters **102,** 211103 (2013).

[118] R. T. Hinkey, Z. B. Tian, S. M. S. S. Rassel, R. Q. Yang, J. F. Klem, and M. B. Johnson, "Interband Cascade Photovoltaic Devices for Conversion of Mid-IR Radiation," IEEE Journal of Photovoltaics **3,** 745 (2013).

[119] R. Q. Yang, H. Lotfi, L. Li, R. T. Hinkey, H. Ye, J. F. Klem, L. Lei, T. Mishima, J. Keay, and M. Santos, "Quantum-engineered interband cascade photovoltaic devices," *Proc. SPIE*, **8993**, 899310 (2014).

[120] H. Ye, H. Lotfi, L. Li, R. T. Hinkey, R. Q. Yang, L. Lei, J. C. Keay, M. B. Johnson, T. D. Mıshıma, and M. B. Santos, "Multistage interband cascade photovoltaic devices with a bandgap of 0.23 eV operating above room temperature," Chinese Science Bulletin **59,** 950 (2014).

[121] R. T. Hinkey and R. Q. Yang, "Theoretical comparison of performance limits of single-and multiple-stage photovoltaic devices," Semiconductor Science and Technology **30,** 015013 (2014).

[122] H. Lotfi, L. Li, L. Lei, R. Q. Yang, J. F. Klem, and M. B. Johnson, "Narrow-Bandgap Interband Cascade Thermophotovoltaic Cells," IEEE Journal of Photovoltaics (2017).

[123] M. Razeghi, A. Haddadi, A. M. Hoang, E. K. Huang, G. Chen, S. Bogdanov, S. R. Darvish, F. Callewaert, and R. McClintock, "Advances in antimonide-based Type-II superlattices for infrared detection and imaging at center for quantum devices," Infrared Physics & Technology **59,** 41 (2013).

[124] M. Hobbs, F. Bastiman, C. Tan, J. David, S. Krishna, and E. Plis, "Uncooled MWIR InAs/GaSb type-II superlattice grown on a GaAs substrate,*" Proc. SPIE,* **8899**, 889906 (2013).

[125] B.-M. Nguyen, D. Hoffman, P.-Y. Delaunay, and M. Razeghi, "Dark current suppression in type II InAs⁄GaSb superlattice long wavelength infrared photodiodes with M-structure barrier," Applied Physics Letters **91,** 163511 (2007).

[126] B. Aslan and R. Turan, "On the internal photoemission spectrum of PtSi/p-Si infrared detectors," Infrared Physics & Technology **43,** 85 (2002).

[127] H. C. Liu, M. Buchanan, and Z. R. Wasilewski, "Short wavelength (1–4 μm) infrared detectors using intersubband transitions in GaAs-based quantum wells," Journal of Applied Physics **83,** 6178 (1998).

[128] Z. B. Tian, E. A. Plis, R. T. Hinkey, and S. Krishna, "Influence of composition in InAs/GaSb type-II superlattices on their optical properties," Electronics Letters **50,** 1733 (2014).

[129] T. Schuler-Sandy, S. Myers, B. Klein, N. Gautam, P. Ahirwar, Z. B. Tian, T. Rotter, G. Balakrishnan, E. Plis, and S. Krishna, "Gallium free type II InAs/$InAs_xSb_{1-x}$ superlattice photodetectors," Applied Physics Letters **101,** 071111 (2012).

[130] N. Gautam, S. Myers, A. V. Barve, B. Klein, E. P. Smith, D. Rhiger, E. Plis, M. N. Kutty, N. Henry, T. Schuler-Sandy, and S. Krishna, "Band engineered HOT midwave infrared detectors based on type-II InAs/GaSb strained layer superlattices," Infrared Physics & Technology **59,** 72 (2013).

[131] W. Guo-Wei, X. Ying-Qiang, G. Jie, T. Bao, R. Zheng-Wei, H. Zhen-Hong, and N. Zhi-Chuan, “Growth and characterization of GaSb-based type-II InAs/GaSb superlattice photodiodes for mid-infrared detection,” Chinese Physics Letters **27,** 077305 (2010).

[132] J. Piotrowski and W. Gawron, “Ultimate performance of infrared photodetectors and figure of merit of detector material,” Infrared Physics & Technology **38,** 63 (1997).

[133] Rui Q. Yang, Hossein Lotfi, Lu Li, Lin Lei, Hao Ye, SM Shazzad Rassel, Yuchao Jiang, Tetsuya D. Mishima, Michael B. Santos, and M. B. Johnson, "Recent progress in interband cascade IR photodetectors," in talk 9755-36 at *Quantum Sensing and Nanophotonic Devices XIII at Photonics West*, San Francisco, California, Feb. 13-18 (2016).

[134] B. Satpati, J. B. Rodriguez, A. Trampert, E. Tournié, A. Joullié, and P. Christol, “Interface analysis of InAs/GaSb superlattice grown by MBE,” Journal of Crystal Growth **301-302,** 889 (2007).

[135] Y. Livneh, P. Klipstein, O. Klin, N. Snapi, S. Grossman, A. Glozman, and E. Weiss, “k· p model for the energy dispersions and absorption spectra of InAs/GaSb type-II superlattices,” Physical Review B **86,** 235311 (2012).

[136] R. Rehm, M. Walther, J. Schmitz, F. Rutz, J. Fleißner, R. Scheibner, and J. Ziegler, “InAs/GaSb superlattices for advanced infrared focal plane arrays,” Infrared Physics & Technology **52,** 344 (2009).

[137] M. Beck, D. Hofstetter, T. Aellen, J. Faist, U. Oesterle, M. Ilegems, E. Gini, and H. Melchior, “Continuous Wave Operation of a Mid-Infrared Semiconductor Laser at Room Temperature,” Science **295,** 301 (2002).

[138] M. Razeghi, N. Bandyopadhyay, Y. Bai, Q. Lu, and S. Slivken, “Recent advances in mid infrared (3-5µm) Quantum Cascade Lasers,” Optical Materials Express **3,** 1872 (2013).

[139] I. Vurgaftman, R. Weih, M. Kamp, J. R. Meyer, C. L. Canedy, C. S. Kim, M. Kim, W. W. Bewley, C. D. Merritt, J. Abell, and S. Höfling, “Interband cascade lasers,” Journal of Physics D: Applied Physics **48,** 123001 (2015).

[140] L. Shterengas, R. Liang, G. Kipshidze, T. Hosoda, G. Belenky, S. S. Bowman, and R. L. Tober, “Cascade type-I quantum well diode lasers emitting 960 mW near 3 µm,” Applied Physics Letters **105,** 161112 (2014).

[141] I. Vurgaftman, J. R. Meyer, and L. R. Ram-Mohan, “Band parameters for III–V compound semiconductors and their alloys,” Journal of Applied Physics **89,** 5815 (2001).

[142] M. J. Cherng, H. R. Jen, C. A. Larsen, G. B. Strigfellow, H. Lundt, and P. C. Taylor, "MOVPE growth of GaInAsSb," Journal of Crystal Growth **77,** 408 (1986).

[143] O. Kentaro, "Unstable Regions in III–V Quaternary Solid Solutions Composition Plane Calculated with Strictly Regular Solution Approximation," Japanese Journal of Applied Physics **21,** L323 (1982).

[144] H. K. Choi, S. J. Eglash, and G. W. Turner, "Double-heterostructure diode lasers emitting at 3 μm with a metastable GaInAsSb active layer and AlGaAsSb cladding layers," Applied Physics Letters **64,** 2474 (1994).

[145] C. Lin, M. Grau, O. Dier, and M.-C. Amann, "Low threshold room-temperature continuous-wave operation of 2.24–3.04 μm GaInAsSb/AlGaAsSb quantum-well lasers," Applied Physics Letters **84,** 5088 (2004).

[146] M. H. M. Reddy, J. T. Olesberg, C. Cao, and J. P. Prineas, "MBE-grown high-efficiency GaInAsSb mid-infrared detectors operating under back illumination," Semiconductor Science and Technology **21,** 267 (2006).

[147] H. Shao, A. Torfi, W. Li, D. Moscicka, and W. I. Wang, "High detectivity AlGaAsSb/InGaAsSb photodetectors grown by molecular beam epitaxy with cutoff wavelength up to 2.6μm," Journal of Crystal Growth **311,** 1893 (2009).

[148] B. Zhang, T. Zhou, H. Jiang, Y. Ning, and Y. Jin, "GaInAsSb/GaSb infrared photodetectors prepared by MOCVD," Electronics Letters **31,** 830 (1995).

[149] A. Yildirim and J. P. Prineas, "Strain- and kinetically induced suppression of phase separation in MBE-grown metastable and unstable GaInAsSb quaternary alloys for mid-infrared optoelectronics," Journal of Vacuum Science & Technology B: Microelectronics and Nanometer Structures **31,** 03C125 (2013).

[150] C. Lin and A. Z. Li, "The effect of strain on the miscibility gap in Ga–In–Sb ternary alloy," Journal of Crystal Growth **203,** 511 (1999).

[151] D. Lubyshev, Y. Qiu, J. M. Fastenau, A. W. K. Liu, E. J. Koerperick, J. T. Olesberg, and J. D. Norton, "Manufacturable MBE growth process for Sb-based photodetector materials on large diameter substrates," *Proc. SPIE*, **8268**, 82681A (2012).

[152] J. M. Fastenau, D. Lubyshev, Y. Qiu, A. W. K. Liu, E. J. Koerperick, J. T. Olesberg, and D. Norton Jr, "Sb-based IR photodetector epiwafers on 100 mm GaSb substrates manufactured by MBE," Infrared Physics & Technology **59,** 158 (2013).

[153] A. Rogalski, "HgCdTe infrared detector material: history, status and outlook," Reports on Progress in Physics **68,** 2267 (2005).

[154] S. Banerjee and W. A. Anderson, “Temperature dependence of shunt resistance in photovoltaic devices,” Applied Physics Letters **49,** 38 (1986).

[155] E. H. Aifer, S. I. Maximenko, M. K. Yakes, C. Yi, C. L. Canedy, I. Vurgaftman, E. M. Jackson, J. A. Nolde, C. A. Affouda, M. Gonzalez, J. R. Meyer, K. P. Clark, and P. R. Pinsukanjana, "Recent developments in type-II superlattice-based infrared detectors,*" Proc. SPIE,* **7660**, 76601Q (2010).

[156] B. Monemar and B. E. Sernelius, “Defect related issues in the “current roll-off” in InGaN based light emitting diodes,” Applied Physics Letters **91,** 181103 (2007).

[157] M. Kopytko and A. Rogalski, “HgCdTe barrier infrared detectors,” Progress in Quantum Electronics **47,** 1 (2016).

[158] S. L. Chuang, *Physics of Photonic Devices* (Wiley Publishing, 2009).

[159] Y. B. Li, R. A. Stradling, T. Knight, J. R. Birch, R. H. Thomas, C. C. Phillips, and I. T. Ferguson, “Infrared reflection and transmission of undoped and Si-doped InAs grown on GaAs by molecular beam epitaxy,” Semiconductor Science and Technology **8,** 101 (1993).

[160] E. O. Kane, “Band structure of indium antimonide,” Journal of Physics and Chemistry of Solids **1,** 249 (1957).

[161] C. J. Hill, A. Soibel, D. Z. Y. Ting, S. A. Keo, J. M. Mumolo, J. Nguyen, M. Lee, and S. D. Gunapala, “High temperature operation of long-wavelength infrared superlattice detector with supressed dark current,” Electronics Letters **45,** 1089 (2009).

[162] A. Soibel, D. Z.-Y. Ting, C. J. Hill, M. Lee, J. Nguyen, S. A. Keo, J. M. Mumolo, and S. D. Gunapala, “Gain and noise of high-performance long wavelength superlattice infrared detectors,” Applied Physics Letters **96,** 111102 (2010).

[163] A. V. Barve, S. J. Lee, S. K. Noh, and S. Krishna, “Review of current progress in quantum dot infrared photodetectors,” Laser & Photonics Reviews **4,** 738 (2010).

[164] S. Chakrabarti, S. Adhikary, N. Halder, Y. Aytac, and A. G. U. Perera, “High-performance, long-wave (~10.2 μm) InGaAs/GaAs quantum dot infrared photodetector with quaternary In0.21Al0.21Ga0.58As capping,” Applied Physics Letters **99,** 181102 (2011).

[165] M. Kopytko, A. Kębłowski, W. Gawron, and W. Pusz, “LWIR HgCdTe barrier photodiode with Auger-suppression,” Semiconductor Science and Technology **31,** 035025 (2016).

[166] A. Haddadi, G. Chen, R. Chevallier, A. M. Hoang, and M. Razeghi, "InAs/InAs$_{1-x}$Sb$_x$ type-II superlattices for high performance long wavelength infrared detection," Applied Physics Letters **105,** 121104 (2014).

[167] J. Bajaj, G. Sullivan, D. Lee, E. Aifer, and M. Razeghi, "Comparison of type-II superlattice and HgCdTe infrared detector technologies,*" Proc. SPIE*, **6542**, 65420B (2007).

[168] J. Piotrowski and A. Rogalski, "Uncooled long wavelength infrared photon detectors," Infrared Physics & Technology **46,** 115 (2004).

[169] H. Mohseni, J. Wojkowski, M. Razeghi, G. Brown, and W. Mitchel, "Uncooled InAs-GaSb type-II infrared detectors grown on GaAs substrates for the 8-12-μm atmospheric window," IEEE Journal of Quantum Electronics **35,** 1041 (1999).

[170] H. Mohseni and M. Razeghi, "Long-wavelength type-II photodiodes operating at room temperature," IEEE Photonics Technology Letters **13,** 517 (2001).

[171] H. Lotfi, L. Li, L. Lei, H. Ye, S. M. S. Rassel, Y. Jiang, R. Q. Yang, J. F. Klem, T. D. Mishima, M. B. Santos, M. B. Johnson, and J. A. Gupta, "Recent developments in interband cascade infrared photodetectors,*" Proc. SPIE*, **9819**, 98190Q (2016).

[172] W. E. Tennant, ""Rule 07" Revisited: Still a Good Heuristic Predictor of p/n HgCdTe Photodiode Performance?," Journal of Electronic Materials **39,** 1030 (2010).

[173] D. R. Rhiger, "Performance Comparison of Long-Wavelength Infrared Type II Superlattice Devices with HgCdTe," Journal of Electronic Materials **40,** 1815 (2011).

[174] M. A. Kinch, *State-of-the-art infrared detector technology* (Bellingham, Washington : SPIE Press, 2014).

[175] Q. K. Yang, F. Fuchs, J. Schmitz, and W. Pletschen, "Investigation of trap-assisted tunneling current in InAs/(GaIn)Sb superlattice long-wavelength photodiodes," Applied Physics Letters **81,** 4757 (2002).

[176] K. K. Choi, B. F. Levine, R. J. Malik, J. Walker, and C. G. Bethea, "Periodic negative conductance by sequential resonant tunneling through an expanding high-field superlattice domain," Physical Review B **35,** 4172 (1987).

[177] L. Bürkle, F. Fuchs, E. Ahlswede, W. Pletschen, and J. Schmitz, "Wannier-Stark localization in InAs/(GaIn)Sb superlattice diodes," Physical Review B **64,** 045315 (2001).

[178] E. H. Aifer, J. G. Tischler, J. H. Warner, I. Vurgaftman, W. W. Bewley, J. R. Meyer, J. C. Kim, L. J. Whitman, C. L. Canedy, and E. M. Jackson, "W-structured type-II superlattice long-wave infrared photodiodes with high quantum efficiency," Applied Physics Letters **89,** 053519 (2006).

[179] L. L. Chang, L. Esaki, and R. Tsu, "Resonant tunneling in semiconductor double barriers," Applied Physics Letters **24,** 593 (1974).

[180] J. Soderstrom and T. G. Andersson, "A multiple-state memory cell based on the resonant tunneling diode," IEEE electron device letters **9,** 200 (1988).

[181] S. Sen, F. Capasso, D. Sivco, and A. Y. Cho, "New resonant-tunneling devices with multiple negative resistance regions and high room-temperature peak-to-valley ratio," IEEE electron device letters **9,** 402 (1988).

[182] F. Capasso, S. Sen, A. Y. Cho, and D. L. Sivco, "Multiple negative transconductance and differential conductance in a bipolar transistor by sequential quenching of resonant tunneling," Applied Physics Letters **53,** 1056 (1988).

[183] H. C. Liu and T. C. L. G. Sollner, Chapter 6 "High-frequency resonant-tunneling devices," in *High-Speed Heterostructure Devices*, Semiconductor and Semimetals, **41** (1994).

[184] L. Esaki and L. L. Chang, "New Transport Phenomenon in a Semiconductor "Superlattice"," Physical Review Letters **33,** 495 (1974).

[185] C. Sirtori, F. Capasso, J. Faist, A. L. Hutchinson, D. L. Sivco, and A. Y. Cho, "Resonant tunneling in quantum cascade lasers," IEEE Journal of Quantum Electronics **34,** 1722 (1998).

[186] S. Kumar and Q. Hu, "Coherence of resonant-tunneling transport in terahertz quantum-cascade lasers," Physical Review B **80,** 245316 (2009).

[187] M. Sweeny and J. Xu, "Resonant interband tunnel diodes," Applied Physics Letters **54,** 546 (1989).

[188] J. R. Söderström, D. H. Chow, and T. C. McGill, "New negative differential resistance device based on resonant interband tunneling," Applied Physics Letters **55,** 1094 (1989).

[189] L. F. Luo, R. Beresford, and W. I. Wang, "Interband tunneling in polytype GaSb/AlSb/InAs heterostructures," Applied Physics Letters **55,** 2023 (1989).

[190] L. Yang, J. Chen, and A. Cho, "New GaSb/AlSb/GaSb/AiSb/InAs/AiSb/InAs triple-barrier interband tunnelling diode," Electronics Letters **26,** 1277 (1990).

[191] M. P. Houng, Y. H. Wang, C. L. Shen, J. F. Chen, and A. Y. Cho, "Improvement of peak-to-valley ratio by the incorporation of the InAs layer into the GaSb/AlSb/GaSb/AlSb/InAs double barrier resonant interband tunneling structure," Applied Physics Letters **60,** 713 (1992).

[192] R. Q. Yang and J. M. Xu, "Analysis of transmission in polytype interband tunneling heterostructures," Journal of Applied Physics **72,** 4714 (1992).

[193] A. Pfenning, G. Knebl, F. Hartmann, R. Weih, A. Bader, M. Emmerling, M. Kamp, S. Höfling, and L. Worschech, "Room temperature operation of GaSb-based resonant tunneling diodes by prewell injection," Applied Physics Letters **110,** 033507 (2017).

[194] E. Plis, S. Myers, M. N. Kutty, J. Mailfert, E. P. Smith, S. Johnson, and S. Krishna, "Lateral diffusion of minority carriers in InAsSb-based nBn detectors," Applied Physics Letters **97,** 123503 (2010).

[195] Y. Lin, D. Donetsky, D. Wang, D. Westerfeld, G. Kipshidze, L. Shterengas, W. L. Sarney, S. P. Svensson, and G. Belenky, "Development of Bulk InAsSb Alloys and Barrier Heterostructures for Long-Wave Infrared Detectors," Journal of Electronic Materials **44,** 3360 (2015).

[196] S. P. Svensson, D. Donetsky, D. Wang, H. Hier, F. J. Crowne, and G. Belenky, "Growth of type II strained layer superlattice, bulk InAs and GaSb materials for minority lifetime characterization," Journal of Crystal Growth **334,** 103 (2011).

[197] P. C. Klipstein, Y. Livneh, A. Glozman, S. Grossman, O. Klin, N. Snapi, and E. Weiss, "Modeling InAs/GaSb and InAs/InAsSb Superlattice Infrared Detectors," Journal of Electronic Materials **43,** 2984 (2014).

[198] E. H. Steenbergen, B. C. Connelly, G. D. Metcalfe, H. Shen, M. Wraback, D. Lubyshev, Y. Qiu, J. M. Fastenau, A. W. K. Liu, S. Elhamri, O. O. Cellek, and Y.-H. Zhang, "Significantly improved minority carrier lifetime observed in a long-wavelength infrared III-V type-II superlattice comprised of InAs/InAsSb," Applied Physics Letters **99,** 251110 (2011).

[199] L. Höglund, D. Z. Ting, A. Khoshakhlagh, A. Soibel, C. J. Hill, A. Fisher, S. Keo, and S. D. Gunapala, "Influence of radiative and non-radiative recombination on the minority carrier lifetime in midwave infrared InAs/InAsSb superlattices," Applied Physics Letters **103,** 221908 (2013).

[200] H. S. Kim, O. O. Cellek, Z.-Y. Lin, Z.-Y. He, X.-H. Zhao, S. Liu, H. Li, and Y.-H. Zhang, "Long-wave infrared nBn photodetectors based on InAs/InAsSb type-II superlattices," Applied Physics Letters **101,** 161114 (2012).

Appendix A: List of publications

Refereed journal articles

1. **L. Lei**, L. Li, W. Huang, J. A. Massengale, H. Ye, H. Lotfi, R. Q. Yang, T. D. Mishima, M. B. Santos and M. B. Johnson, "Resonant tunneling and multiple negative differential conductance features in long wavelength interband cascade infrared photodetectors," Appl. Phys. Lett., 111, 113504 (2017).

2. W. Huang, **L. Lei**, L. Li, J. A. Massengale, R. Q. Yang, T. D. Mishima, and M. B. Santos, "Current-matching versus non-current-matching in long wavelength interband cascade infrared photodetectors," J. Appl. Phys., 122, 083102 (2017).

3. **L. Lei**, L. Li, H. Lotfi, H. Ye, R. Q. Yang, T. D. Mishima, M. B. Santos and M. B. Johnson, "Mid-wavelength interband cascade infrared photodetectors with superlattice absorber and gain," Opt. Eng., 57(1), 011006 (2017).

4. H. Lotfi, L. Li, **L. Lei**, R. Q. Yang, J. F. Klem, and M. B. Johnson, "Narrow-Bandgap Interband Cascade Thermophotovoltaic Cells," IEEE J. Photovolt. (2017).

5. **L. Lei**, L. Li, H. Ye, H. Lotfi, R. Q. Yang, M. B. Johnson, J. A. Massengale, T. D. Mishima, and M. B. Santos, "Long wavelength interband cascade infrared photodetectors operating at high temperatures," J. Appl. Phys., 120, 193102 (2016).

6. **L. Lei**, L. Li, H. Lotfi, Y. Jiang, R. Q. Yang, M. B. Johnson, D. Lubyshev, Y. Qiu, J. M. Fastenau, and A. W. Liu, "Mid-wave interband cascade infrared photodetectors based on GaInAsSb absorbers," Semicond. Sci. Technol., 31, 105014 (2016).

7. H. Lotfi, L. Li, **L. Lei**, H. Ye, S. M. S. Rassel, Y. Jiang, R. Q. Yang, T. D. Mishima, M. B. Santos, J. A. Gupta, and M. B. Johnson, "High frequency operation of a midinfrared interband cascade system at room temperature," Appl. Phys. Lett., 108, 201101 (2016).

8. H. Lotfi, L. Li, **L. Lei**, R. Q. Yang, J. F. Klem, M. B. Johnson, "Short wavelength interband cascade infrared photodetectors operating above room temperature," J. Appl. Phys., 119, 023105 (2016).

9. H. Lotfi, **L. Lei**, L. Li, R. Q. Yang, J. C. Keay, M. B. Johnson, Y. Qiu, D. Lubyshev, J. M. Fastenau, A. W. K. Liu, "High temperature operation of interband cascade infrared photodetectors with cutoff wavelengths near 8 μm," Opt. Eng., 54(6), 063103 (2015).

10. H. Ye, L. Li, H. Lotfi, **L. Lei**, R. Q. Yang, J. C. Keay, T. D. Mishima, M. B. Santos, M. B. Johnson, "Molecular beam epitaxy of interband cascade structures with InAs/GaSb superlattice absorbers for long wavelength infrared detection," Semicond. Sci. Technol., 30, 105029 (2015).

11. H. Lotfi, L. Li, H. Ye, R. T. Hinkey, **L. Lei**, R. Q. Yang, J. C. Keay, T. D. Mishima, M. B. Santos, and M. B. Johnson, "Interband cascade infrared photodetectors with long and very long cutoff wavelengths", Infrared Phys. Technol., 70, 162167 (2015).

12. H. Ye, H. Lotfi, L. Li, R. T. Hinkey, R. Q. Yang, **L. Lei**, J. C. Keay, M. B. Johnson, T. D. Mishima, and M. B. Santos, "Multistage interband cascade photovoltaic devices with a bandgap of 0.23 eV operating above room temperature", Chin. Sci. Bull., 59, 950955 (2014).

13. C. K. Gaspe, S. Cairns, **L. Lei**, K. S. Wickramasinghe, T. D. Mishima, J. C. Keay, S. Q. Murphy, and M. B. Santos, “Epitaxial growth of elemental Sb quantum wells,” J. Vac. Sci. Technol. B 31, 03C129 (2013).

Conference proceedings

1. **L. Lei**, L. Li, H. Ye, H. Lotfi, R. Q. Yang, M. B. Johnson, J. A. Massengale, T. D. Mishima, and M. B. Santos, “Long-wavelength interband cascade infrared photodetectors towards high temperature operation,” *Proc. SPIE* 10111, 1011113-1 (2017)

2. H. Lotfi, L. Li, **L. Lei**, H. Ye, S. M. S. Rassel, Y. Jiang, R. Q. Yang, J. F. Klem, T. D. Mishima, M. B. Santos, M. B. Johnson, and J. A. Gupta, “Recent developments in interband cascade infrared photodetectors,” *Proc. SPIE* 9819, 98190Q-1 (2016)

3. H. Lotfi, **L. Lei**, L. Li, R. Q. Yang, J. C. Keay, M. B. Johnson, Y. Qiu, D. Lubyshev, J. M. Fastenau, and A. W. K. Liu, “Long-wavelength interband cascade infrared photodetectors operating above room temperature,” *Proc. SPIE* 9370, 937032-1 (2015)

4. R. Q. Yang, H. Lotfi, L. Li, R. T. Hinkey, H. Ye, J. F. Klem, **L. Lei**, T. D. Mishima, J. C. Keay, M. B. Santos, and M. B. Johnson, “Quantum-engineered interband cascade photovoltaic devices,” *Proc. SPIE* 8893, 889310-1 (2014)

5. R. T. Hinkey, H. Lotfi, L. Li, H. Ye, **L. Lei**, R. Q. Yang, J. C. Keay, T. D. Mishima, M. B. Santos, and M. B. Johnson, “Interband cascade infrared photodetectors with InAs/GaSb superlattice absorbers,” *Proc. SPIE* 8868, 886805-1 (2013)